MReadings: Ultra High Field MRI

Contributions from our MAGNETOM users

Not for distribution in the US.

SIEMENS

Towards Clinical 7T MRI

Graham C. Wiggins, D Phil; Daniel K. Sodickson, MD, PhD

Center for Biomedical Imaging, Department of Radiology, New York University Langone Medical Center, New York, NY, USA

Introduction

Many researchers in the field of ultra-high-field magnetic resonance have become accustomed to bracing themselves for an oft-repeated question. This question may arise during lulls in conversation with clinical colleagues, or during interviews with interested visitors from the press or the lay public, or, more delicate still, during reviews of our applications for research funding. The question is brief, and to the point: *'When will 7 Tesla scanners be ready for clinical use?'* Each of us has his or her own variant on a standard answer to this question, citing particular populations or disease processes in which we have obtained extraordinarily promising images, and outlining the technical hurdles which are gradually falling behind us as research advances. This twofold answer actually encapsulates two distinct strains of 7T research, each of which has an important part to play in defining the eventual clinical role of 7T MR. The first involves identification of unique information available only at ultra-high field strength, enabled for example by extremely high spatial and spectral resolution or by contrast mechanisms which are enhanced as field strength increases. The potential to access this unique information helped to motivate the original development of commercial 7T scanners, and fueled a great sense of enthusiasm as the first whole-body 7T systems arrived on the scene and the first jaw-dropping images began to emerge from those systems. This initial period of exuberant discovery was followed by an equally fascinating but also laborious period of extended basic development, during which 7T research teams began to grapple with the fact that not only the potential information content but also the routine operations of 7T scanners differed from what we had come to expect with lower-field scanners. Coils and pulse sequences required careful redesign and optimization, artifacts only hinted at in low-field settings became critical determinants of image quality at 7T, and new constraints on sequence types and parameters changed both the workflow and the content of day-to-day imaging protocols. In the past several years, a growing cadre of high-field researchers has risen to these challenges, seeking to identify the novel RF structures, calibration procedures, and spin manipulations that can eke the best performance out of 7T scanners. The goal of this second strain of research, occurring in parallel with the first, is to replicate some of the breadth and routine image quality of low-field scans, overcoming any and all practical obstacles along the way. Such nominally replicative research has actually spurred a remarkable range of technological and methodological innovation: witness the rise of parallel transmission techniques, reported in previous editions of this magazine, which have become a common component in many 7T research programs but which have already begun to have an impact on lower field strengths. Perhaps of equal importance, however, is the fact that research aimed at achieving high image quality across multiple examination types and body regions addresses an important requirement for what might be considered an ideal clinical 7T imaging platform: the ability to provide unique clinically-relevant information for a variety of disease processes without sacrificing traditional clinical image content in routine examinations. A 7T scanner with this ability need not be relegated to research tool or niche diagnostic device, but can take its place as a valuable component of the day-to-day clinical arsenal. This article reports on recent developments in the twofold pursuit of unique information content and routine usability at 7T, drawing examples from imaging experience at our institution. The clinical transformation of 7T scanning is by no means complete, but the picture that has begun to emerge is striking.

Unique clinical potential: A gallery of pathology-targeted 7T images from toe to head

The principal advantages of ultra-high field strength for MR imaging are
a) increased signal-to-noise-ratio (SNR), which can be used to increase spatial resolution, to shorten scan time, and/or to enable imaging of low-sensitivity nuclei other than hydrogen; and
b) enhanced contrast mechanisms such as those based on susceptibility-related effects. The corresponding challenges associated with 7T MRI include increased inhomogeneity of the RF transmit and the B_0 fields (which result in increased artifacts in various classes of pulse sequence) and increased RF energy deposition into tissue, as quantified by specific absorption rate (SAR), which can limit the range of sequence parameters which may safely be employed. 7T MRI of the brain has now become fairly routine, with the availability of reliable high-performance head coils, and high quality images in a variety of contrasts can be obtained. We will demonstrate later how a standard 3T clinical neuro imaging protocol can be translated to 7T, illustrating both advantages and challenges of ultra-high-field imaging, and presenting the opportunity to obtain familiar image contrasts while also exploring higher resolution and new contrast mechanisms in a single 7T scan session. The musculoskeletal system has become another highly fruitful area of 7T application, and we begin our catalogue of images there, proceeding from foot to head. Body imaging at 7T (e.g. targeting the heart, abdomen, or pelvis) continues to present unique challenges at 7T. However, 7T body imaging has been the subject of intensive recent attention, with striking examples provided and creative approaches undertaken by various ultra-high-field research groups. As mentioned earlier, parallel transmission and other related methods are currently under investigation to mitigate the particularly substantial B_1 inhomogeneities observed over large fields-of-view in the torso, and also to control SAR. Meanwhile robust imaging of selected body areas such as the breast may already be obtained at 7T with conventional single channel excitation.

1 The NYU 7 Tesla scanner.

2 Sagittal image of the ankle of a healthy adult subject. Note high-resolution depiction of cartilage and trabecular bone. (Fat-suppressed 3D FLASH, 0.23 x 0.23 x 1 mm³, TR/TE 26/5.1 ms, 60 partitions, acquisition time 6:58 min, custom-designed transmit-receive extremity coil array with 8 receive elements.)

At our institution, the past year or two has seen a surge of clinical interest in our 7T scanner, as clinical colleagues in our Department of Radiology and elsewhere have partnered with our basic researchers to probe anatomical details and pathologic processes for which key information has proven to be elusive at lower field strength. The backlog and hours of use of our 7T system have both increased markedly, and it has become an increasingly commonplace occurrence to find a radiologist at the console. The images that follow, all obtained on the Siemens MAGNETOM whole-body 7T scanner at the Center for Biomedical Imaging at NYU School of Medicine (Fig. 1), illustrate some of the multifaceted clinical promise of 7T MRI. These images, which we have sorted by body region and, when appropriate, disease process, are intended to indicate the image quality which may now be achieved at 7T with modern RF coil arrays and pulse sequences. The examples shown here represent only a subset of *in vivo* 7T scans at our center, and an even smaller subset of the work being done at a growing number of Siemens 7T sites around the world.

Ankle

Figure 2 shows a sagittal image of the ankle obtained at 0.23 x 0.23 mm^2 in-plane resolution in a healthy adult subject using a custom-designed transmit-receive extremity coil array [1]. Note the high-resolution depiction both of cartilage and of trabecular bone in this image. Although no particular pathology is evident in this example, the ability to resolve cartilage and bone structure at this level becomes a powerful asset for the detection and characterization of disease processes like those in the examples to follow.

Knee

Osteoarthritis

Figures 3 and 4 compare 7T scans of healthy adult subjects with corresponding scans of patients with radiographically documented osteoarthritis. Each of these images was obtained using a 28-element 7T knee coil array developed by Quality Electrodynamics (QED), LLC [2] and expected to be available com-

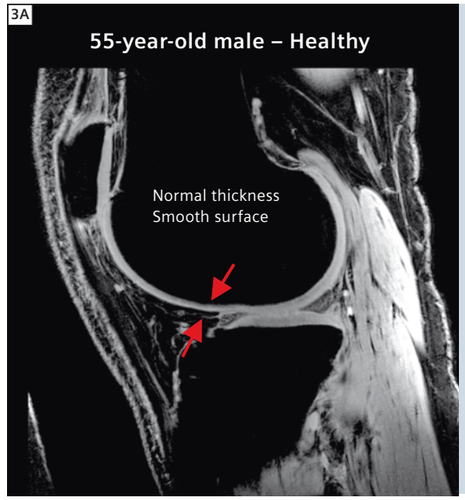

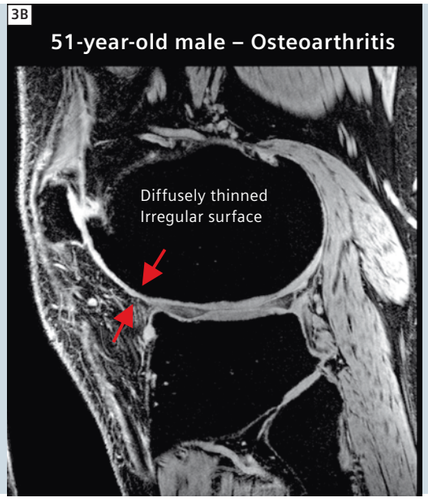

3 The high spatial resolution available at 7T enables visualization of the diffusely thinned irregular cartilage surface in a patient with osteoarthritis (right), as compared with an age-matched healthy subject (left). (Fat-suppressed 3D FLASH, TR/TE 26/5.1 ms, 0.23 x 0.23 x 1 mm³, 60 partitions, acquisition time 6:58 min, transmit-receive 7T knee coil array with 28 receive elements from QED. *Images courtesy of Gregory Chang, M.D., Department of Radiology, NYULMC, USA).*

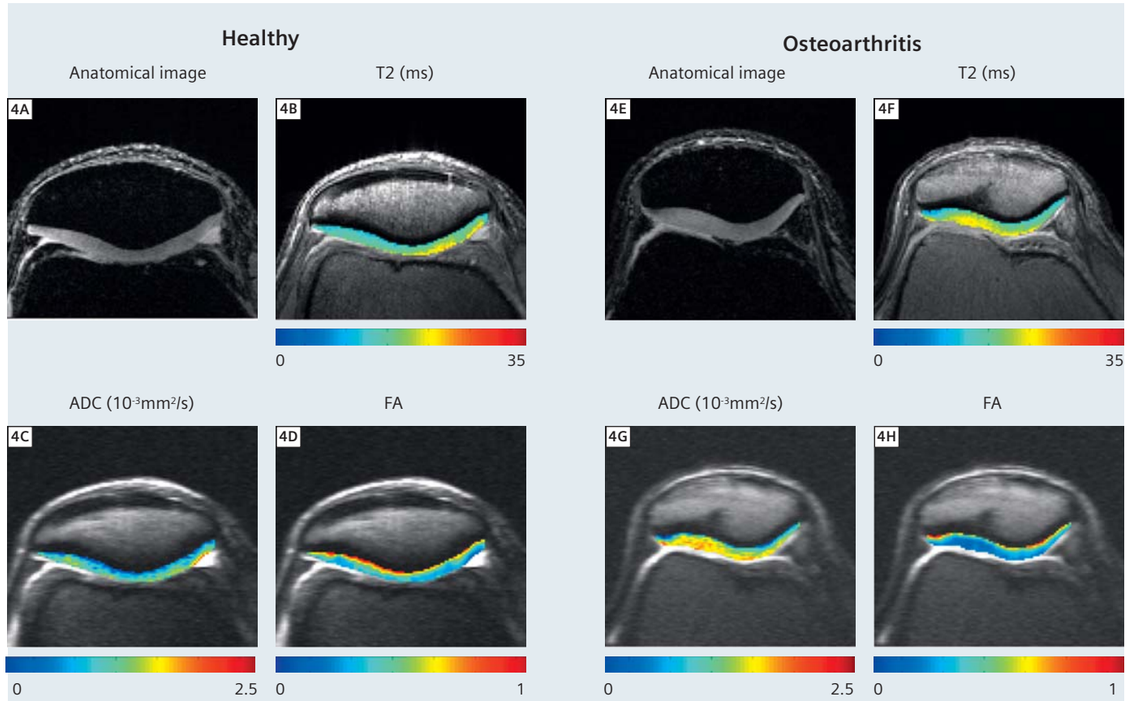

4 Apparent diffusion constant (ADC) and fractional anisotropy (FA) maps derived from line-scan diffusion acquisitions (bottom row) juxtaposed to anatomical images and T_2 maps in the knees of a healthy adult subject (left) and a patient with osteoarthritis (right). Increased ADC and decreased FA are seen in diseased tissue, reflecting microscopic changes in the fiber structure of the cartilage. (Line Scan Diffusion Tensor Imaging sequence: TE/TR/TReff 46/180/2890 ms, 0.6 x 0.6 x 2 mm³, 5 slices, b-values 5, 450 s/mm², 6 directions, fat-saturation, acquisition time 14:00 min; Anatomical images: T_2*-weighted fat-saturated GRE, TE/TR 9.2/40 ms, 0.5 x 0.5 x 0.5 mm², acquisition time 10:00 min; T_2-mapping acquisitions: multi-slice 2D multi-echo fat-saturated sequence with stimulated echo suppression, TE/TR 16/3500 ms, 0.6 x 0.6 x 2 mm³, 5 slices, echo train length 8, acquisition time 13:35 min. QED 28-element 7T knee array used in all cases. *Images courtesy of Jose Raya, Ph.D., NYULMC, USA.*)

mercially in the near future. The 0.23 x 0.23 mm² in-plane spatial resolution of the sagittal images in Figure 3 is sufficient for direct visual appreciation of the diffusely thinned and irregular cartilage surface in the osteoarthritic patient. The images in Figure 4, on the other hand, are targeted to microscopic changes in cartilage structure and function. In addition to anatomical images and T_2 maps, maps of apparent diffusion constant (ADC) and fractional anistropy (FA) are shown, derived from line-scan diffusion acquisitions. The decreased FA in the cartilage of subjects with osteoarthritis is consistent with structural damage to the collagen network. The increased ADC, on the other hand, may be shown to result from reduced proteoglycan content. Figure 5 illustrates the potential value of 7T scanning for a complementary evaluation of proteoglycan content, and therefore of cartilage function. These images represent various slices through 3D volumetric sodium concentration maps encompassing the whole knee in a healthy subject as compared with a patient with osteoarthritis (OA). The enhanced SNR available at 7T enabled whole-knee acquisitions at 2 mm isotropic resolution in less than 15 minutes. Such acquisitions would not be possible at lower field strengths, given inherently low MR sensitivity to sodium nuclei. Through appropriate calibration, sodium images were converted into quantitative sodium concentrations, which may be seen to be generally decreased in the osteoarthritic as compared with the healthy knee cartilage. Indeed, the average sodium concentration across the knee cartilage in 5 patients with OA was noticeably lower than that in a group of 5 healthy controls. This change reflects a loss of proteoglycans, the removal of whose net negative charge results in a corresponding loss of positively-charged sodium ions to preserve charge balance.

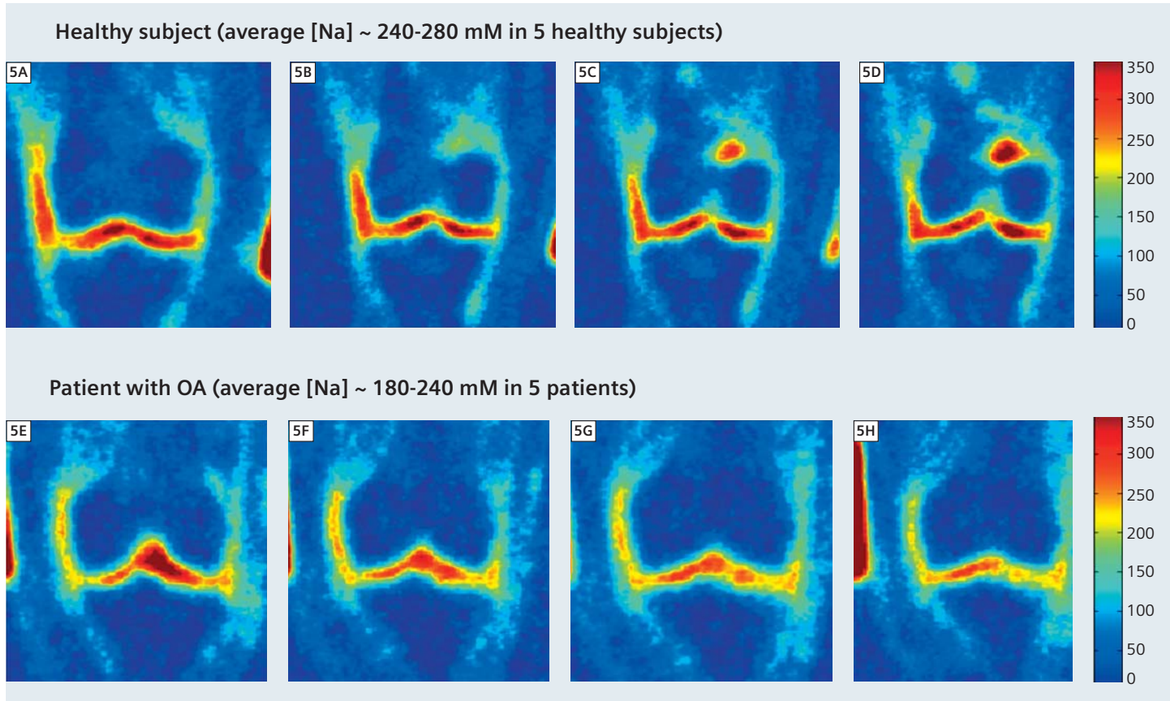

5 7T sodium imaging of cartilage in a healthy subject (top) and a patient with osteoarthritis (bottom). 7T field strength enabled whole-knee 3D volumetric sodium concentration maps at comparatively high resolution in less than 15 minutes. Note reductions in average sodium concentration in arthritic versus healthy cartilage, both in the individual knees shown and in ensembles of 5 patients and 5 controls. (Undersampled 3D radial pulse sequence, TR/TE 80/0.2 ms, 2.0 x 2.0 x 2.0 mm³, single-tuned quadrature sodium coil custom-designed in collaboration with Rapid Biomedical, GmbH. *Images courtesy of Ravi Regatte, Ph.D., Department of Radiology, NYULMC, USA.*)

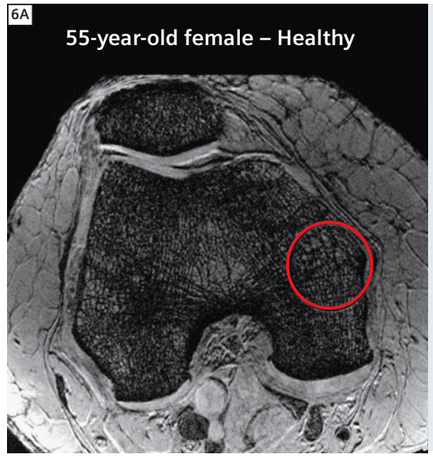

6 Images of the distal femur of a healthy subject (left) and a patient with osteoporosis (right). Note the reduction in density of trabecular bone structure in the patient as compared with the control (for example, in the circled regions of interest). (3D FLASH, TR/TE 20/5.1ms, 0.23 x 0.23 x 1.0 mm³, 80 partitions, acquisition time 7:09 min, QED 28-element knee coil array. *Images courtesy of Gregory Chang, M.D., Department of Radiology, NYULMC, USA.*)

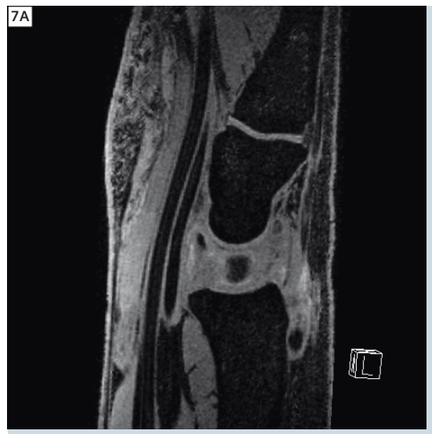

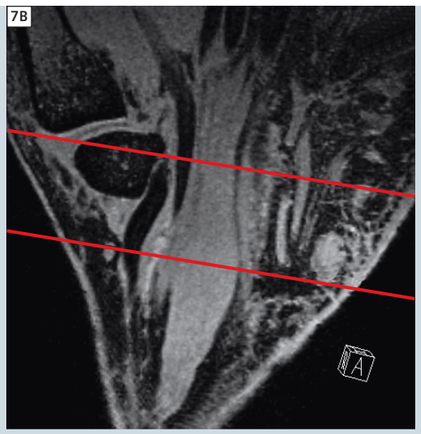

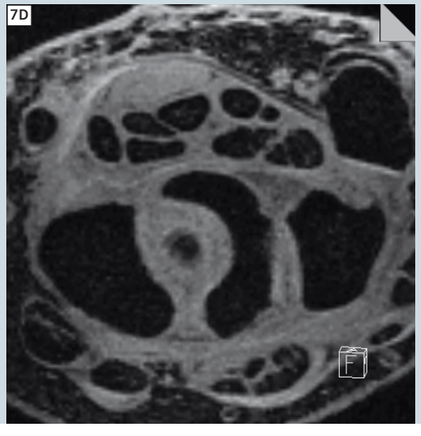

7 Images from a 0.33 mm³ isotropic 3D gradient-echo acquisition in a patient with Carpal Tunnel Syndrome. The red lines in the top right image indicate the image plane geometry of the bottom two images. The anatomy within the carpal tunnel is clearly delineated, and pronounced swelling of the median nerve may be appreciated. (3D FLASH, TR/TE 40/3.2 ms, 0.33 x 0.33 x 0.33 mm³, 128 partitions, acquisition time 7:10 min, custom-built 8-element 7T extremity coil array. *Images obtained as part of a collaboration with Dr. David Chiu, Department of Surgery, NYULMC, USA.*)

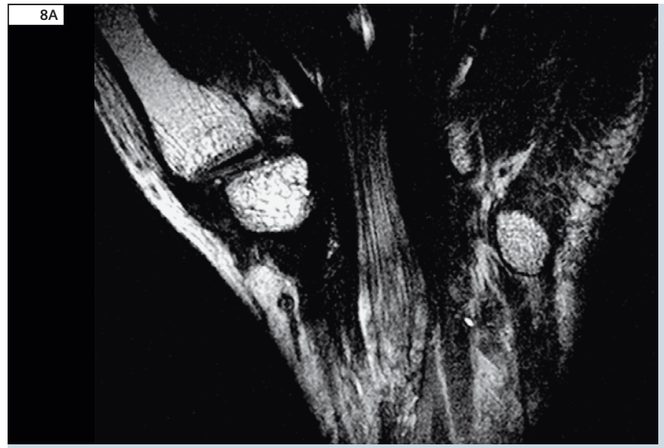

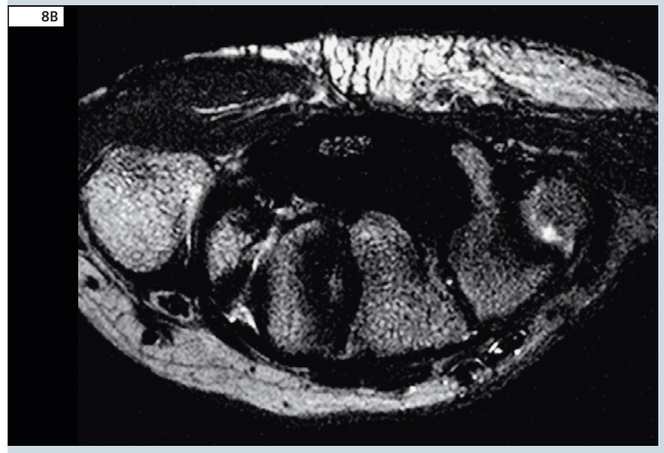

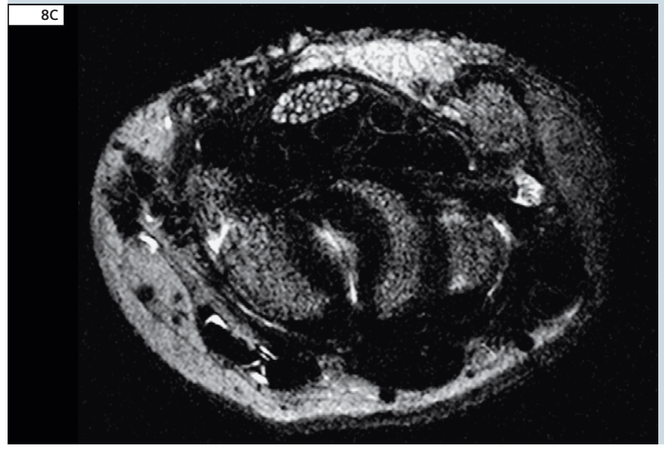

8 2D spin-echo images of a patient with Carpal Tunnel Syndrome. Individual fascicles of the inflamed median nerve can be tracked even through the constriction at the carpal tunnel. (2D TSE, TR/TE 5500/87 ms, 0.2 x 0.2 x 1 mm³, 13 slices, Turbo Factor 13, acqui-sition time 3:35 min, custom-built 8-element 7T extremity coil array. *Images obtained as part of a collaboration with Dr. David Chiu, Department of Surgery, NYULMC, USA.*)

Osteoporosis

In Figure 6, osteoporotic changes in trabecular bone structure may be appreciated directly from axial 7T images, rather than being probed indirectly through projection-based densitometry. This enables assessment not only of bone density but also of bone quality [3, 4]. The image of the osteoporotic patient shows fewer and more widely-separated dark trabeculae with larger marrow spaces between them. This structure reflects a reduced bone strength and a correspondingly increased fracture risk. In fact, it is believed that bone density alone accounts for only 50–60% of the fracture risk in osteoporotic patients, with the remaining risk attributable to bone quality [3]. Thus, 7T imaging has the potential to improve our ability to assess bone strength and clinical fracture risk.

Wrist
Carpal Tunnel Syndrome

In collaboration with interested surgeons at our institution, we have begun to study patients with Carpal Tunnel Syndrome at 7T. The resulting high-resolution depiction of structures surrounding and running through the carpal tunnel, as exemplified in Figures 7 and 8, will enable definitive diagnosis, as well as helping to define surgical approaches and allowing the creation of detailed anatomical atlases in the presence and the absence of pathology.

9 Sagittal 7T images (left, full field-of-view; right, close-up of boxed area) of the spine of a 19 year-old male with a cavernous angioma at T5 discovered incidentally on earlier lower-field MR scans. Imaging at 7T improved spatial resolution and lesion visualization as compared with 1.5T and 3T scans, though certain details are still obscured by susceptibility artifacts from residual blood products. (2D TSE 0.55 x 0.55 x 1.5 mm³, TR/TE 6000/10 ms, 11 slices, acquisition time 4:55 min, custom-built transmit-receive 7T spine array with 8 receive elements.)

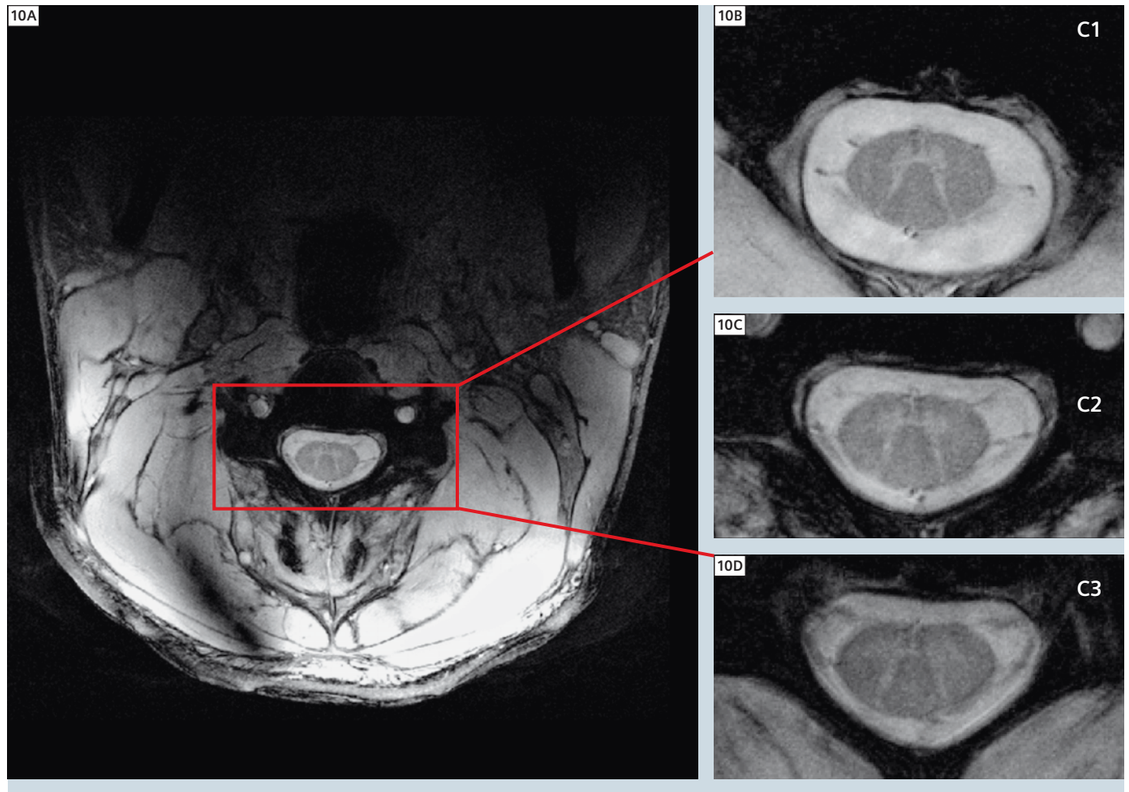

10 High spatial resolution enables noninvasive visualization of spinal cord structure with unprecedented detail. (2D gradient echo, 0.18 x 0.18 x 3.0 mm³, TR/TE 500/4.91 ms, 5 slices, 4 element transmit-receive C-spine array from Rapid Biomedical GmbH. *Images courtesy of Eric Sigmund, Ph.D., Department of Radiology, NYULMC, USA.*)

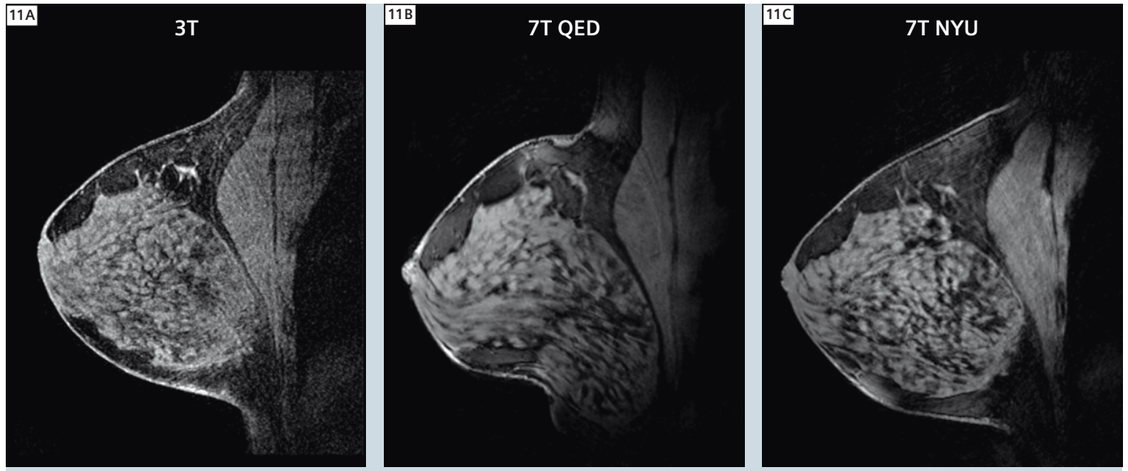

11 Comparison of 3T (left, In Vivo Corp. 4-element receive coil array) and 7T breast images (middle: QED 16-element coil array; right: NYU custom-designed 2-element coil array). 7T images have significantly higher SNR for the same image resolution and total acquisition time. (3D GRE with Fat Saturation, TR/TE 4.37/1.92 ms, 0.6 x 0.6 x 0.6 mm³, 208 partitions, acquisition time 4:28 min. *Images courtesy of Ryan Brown, Ph.D., NYULMC, USA.*)

Thoracic Spine
Cavernoma

Figure 9 documents the case of a 19-year-old patient whose cavernous angioma at thoracic spinal level T5 was discovered incidentally on a 1.5T MR scan at another institution following a sporting accident. Subsequent 3T imaging was also performed in an attempt to determine the feasibility and advisability of surgery for this otherwise asymptomatic young man, but image quality was insufficient to define the detailed internal structure of the lesion and the surrounding spinal cord. The family came to our center in the hope that 7T imaging could further inform their decision and guide a potential surgical approach. A team of physicists, RF engineers, technologists, neuroradiologists, and spinal surgeons was mobilized to address this challenging question. Figure 9 shows sagittal images at two magnifications highlighting the lesion. Using a custom-built 8-channel transmit-receive 7T spine array [5] and optimized gradient-echo and spin-echo pulse sequences, nearby cord structure could be defined with unprecedented detail. Unfortunately, residual blood products in the vascular lesion resulted in susceptibility-related signal voids in the immediate vicinity of the lesion, preventing ideal delineation. Work is now underway to apply susceptibility-insensitive approaches for further improved visualization. This example highlights both the promise and some of the ongoing practical challenges associated with clinical 7T studies.

Cervical Spine

Figure 10, on the other hand, shows the exquisite delineation of spinal cord substructure which may be achieved at 7T in regions not subject to high susceptibility gradients. In these images, obtained with a 4-element transmit-receive C-spine coil array from Rapid Biomedical, GmbH, excellent spatial detail is observed, differentiating gray/white matter tissue, dorsal and ventral nerve roots, denticulate ligaments, dura mater, pia mater, and rostral-caudal blood vessels.

Breast

Figure 11 compares breast images obtained in the same healthy adult subject at 3T and at 7T. Substantial increases in SNR are evident for the same spatial resolution and total acquisition time in the 7T images. 3T images were acquired using a commercially-available 4-element receive-only 3T breast array from In Vivo Corp. 7T images were acquired both with a commercial transmit-receive breast coil array with 16 receive elements from QED and with a custom-designed 2-element transmit-receive breast array developed at our Center. Our custom-designed 7T coil array has also been used to characterize the distribution of T_1 and T_2 values and B_0 field distribution in healthy breast tissue [6], in preparation for clinical studies to come. Some further development and pulse sequence optimization is called for to reap the full benefits of 7T SNR enhancements, but 7T imaging may be expected to shift favorably the balance of spatial and temporal resolution which is so crucial for characterization of breast cancer.

Brain

For neurological applications, the high intrinsic SNR and the correspondingly high achievable spatial resolution at 7T may be used to resolve brain structures which have until now eluded direct visualization with MR. Susceptibility- or T_2*-weighted images in particular can provide extraordinarily high levels of anatomical detail, in addition to affording striking tissue contrast, some of whose precise physical sources are still being investigated. At NYU we have begun to scan volunteers with a variety of known brain diseases to begin exploring what new clinically- and biologically-relevant information may be found at 7T.

Tuberous sclerosis

Recently, a collaboration has arisen between basic researchers, pediatric neuroradiologists, pediatric neurosurgeons, and epileptologists at our institution, aimed at investigating the biological substrate of tuberous sclerosis, a group of genetic disorders with a spectrum of symptoms including potentially intractable seizures. Figure 12 shows images from a patient with tuberous sclerosis. This patient was imaged first with a high resolution T_1-weighted MPRAGE sequence and then with a 3D FLAIR sequence. The high isotropic spatial resolution of these images allows visualization not only of tubers (like the one indicated by red arrows in the figure), but also of subtle signs of cortical dysplasia (blue arrow).

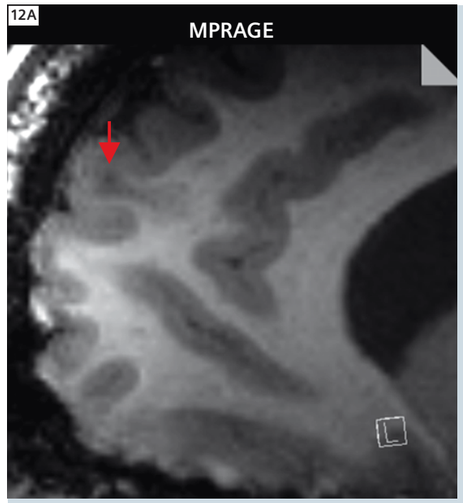

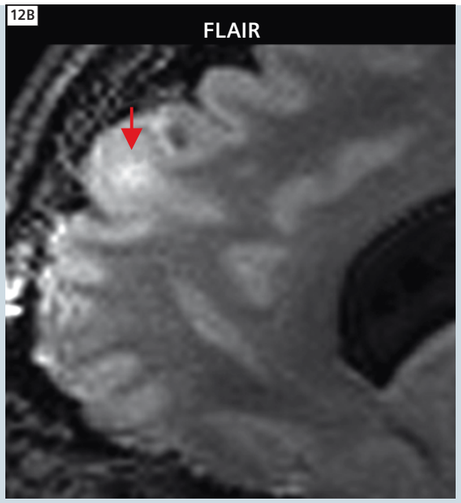

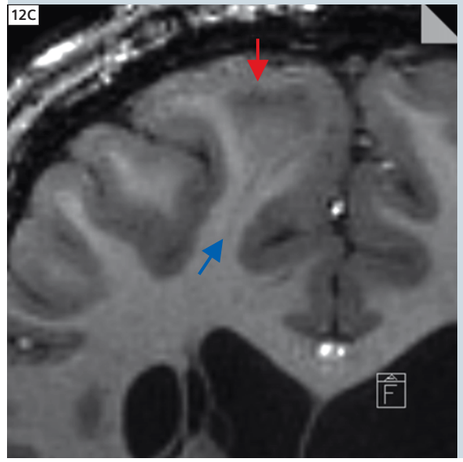

12 Depiction of cortical tuber (red arrows) at 7T with 0.8 mm isotropic MPRAGE (left) and 1 mm isotropic SPACE FLAIR (right). A thin ribbon of grey matter can be seen tracking in towards the ventricle in an axial view (bottom left, blue arrow) – an example of cortical dysplasia. The tuber is hyperintense in the FLAIR images (right). (MPRAGE, 0.8 x 0.8 x 0.8 mm³, TR/ TE 2250/3.8 ms, TI 1100 ms, acquisition time 5:30 min; SPACE-FLAIR, 1.0 x 1.0 x 1.0 mm³, TR/ TE 8000/380 ms, TI 2100 ms, 160 partitions, acquisition time 9:39 min. Nova Medical Inc single-element transmit 24-element receive 7T close-fitting brain array.)

Schizophrenia

Another collaboration between the Departments of Psychiatry and Radiology at our institution resulted in the recent publication of 7T images of the human hippocampus *in vivo* [7], with spatial resolution sufficient to visualize directly such small but important structures as the dentate granule cell layer, which is known to be a locus of neural stem cells. Figure 13 extends this work, showing a direct comparison of coronal and sagittal images between a schizophrenic patient and a healthy control. The smooth regular contour of the inferior border of the hippocampus and the well-defined dentate granule cell layer in the healthy subject may be compared to the ridged appearance of the inferior border and general poor visibility of the dentate layer in the patient. Note that the dentate granule cell layer cannot be seen in images taken at lower magnetic field strengths. The use of images such as these is now being contemplated to identify prodromal individuals at risk of developing schizophrenia, in time to initiate preventive treatment before development of chronic life-altering mental illness. Considering the early age of onset of schizophrenia (typically in the late teens to early 20s), prevention has significant social and economic consequences.

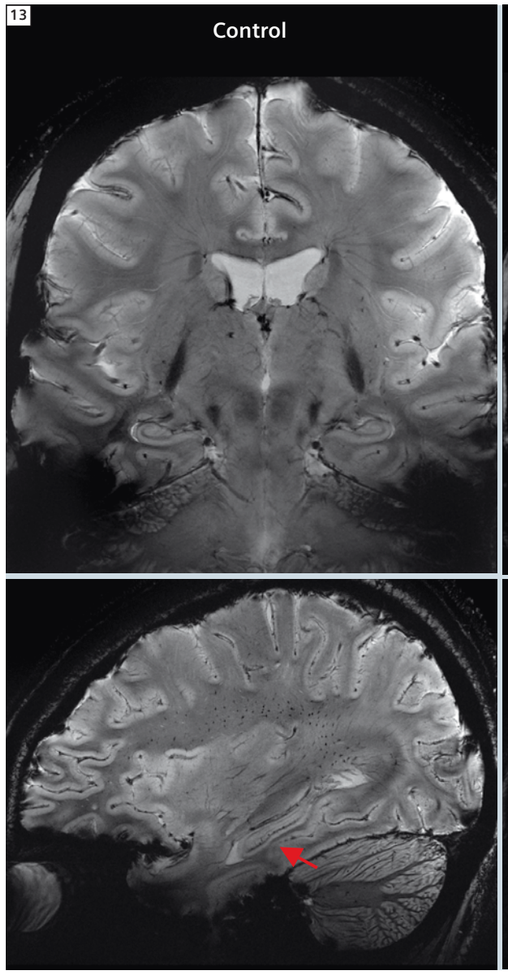

13 T_2*-weighted GRE images of a normal control (left) and a schizophrenic patient (right). Notice the smooth regular contour of the inferior border of the hippocampus and the well-defined dentate granule cell layer in the control, as compared to the ridged appearance of the inferior border and poor visibility of the dentate layer in the patient (arrows). Note also the high contrast in the basal ganglia and in small blood vessels throughout the brain. (T_2*-weighted 2D gradient-echo sequence, TR/TE 944/25 ms, 0.232 × 0.232 ×1.0 mm³, 17 slices, acquisition time 14:00 min. Nova Medical Inc 24-element 7T head array. *Images courtesy of Oded Gonen, Ph.D., NYULMC, USA.*)

Capturing routine clinical information:

Towards a general purpose clinical 7T neuroimaging protocol

Despite the extraordinary image quality available for selected applications, as evidenced by the examples provided earlier in this article, potential clinical enthusiasm for 7T imaging has been hindered by concerns about its ability to support the range of sequence types and provide the range of image contrasts used for routine clinical evaluations at lower field strengths. In this section, we demonstrate that, with appropriate RF coils and pulse sequence modifications, 7T can in fact provide image quality at least equivalent to that available at 3T for a typical clinical neuroimaging protocol. We have developed a set of protocols at 7T which aim to match or exceed the image quality and coverage of the standard 3T clinical protocol within the same total scan time. This makes it possible to obtain a set of images which correspond closely to familiar 3T scans, but also to take advantage of the unique benefits of 7T through increased resolution or through adding on to the protocol specific scans of interest such as T_2*-weighted GRE, very high resolution MP2RAGE, or Time-of-Flight angiography, obtaining precisely co-registered images in a single scan session. We have chosen certain strategies for optimization of the 7T protocols, but make no claim that these are the optimum sequences for the purpose and offer them primarily as an example and a starting point for others.

While there are particular sequences which routinely produce superior results at 7T than at lower field strength, for maximum diagnostic power the clinician would like to have images of the whole brain in a number of standard contrasts and formats. A typical 3T clinical brain protocol at NYU includes axial T_2-weighted TSE, axial FLAIR, axial T_1-weighted MPRAGE, axial HemoFLASH, axial Diffusion, and possibly also sagittal FLAIR. Imaging with this 3T protocol is typically performed using the standard Siemens 12-channel Matrix head coil. At 7T we use what has become our workhorse 7T head coil array – a single-element transmit, 24-element receive head array from Nova Medical, Inc (the same coil used to obtain the images in Figures 12–13). Note that Nova Medical has also developed a 32-element head array of similar design for use at 7T, and this array is available as part of the Siemens 7T coil portfolio. Both 7T arrays have very close-fitting geometries, which gives them an advantage in SNR compared to the larger Matrix coil, above and beyond the SNR increase due solely to the increased magnetic field strength.

Our image comparisons, therefore, should not be taken as a strict study of field-strength-related behavior, but rather as an investigation into whether we can use available equipment at 7T to match or exceed the accepted clinical standard at 3T. One additional caveat regarding presentation of the images to follow involves image intensity normalization, which we have used in most cases to remove the variation in brightness caused by the sensitivity profiles of the receive array. At lower field strength, the body coil can be used as a relatively uniform reference to determine the bias field, but there is no clear uniform reference at 7T. While there is a 2D normalization filter on the scanner, it is not always able to correct for steep intensity gradients near the receive elements, and it is not appropriate for 3D scans. Therefore, for this article we have processed 7T images with an off-line intensity normalization algorithm provided with the Firevoxel software, a data analysis tool developed by researchers at NYU [8].

For the interested reader, detailed scan parameters for 3T and 7T protocols will be provided in an online supplement to this article (see URL reference at the end). By leveraging the increased SNR at 7T and by carefully calibrating the required transmit power, we can trade off parameters in the various imaging sequences to address issues of inhomogeneity and SAR. To this end, one addition we have made to the standard 3T protocol is an in-house-developed 'B_1 scout,' which uses a nonselective preparation pulse and a TurboFLASH readout to determine what scanner transmitter calibration voltage will produce a 90 degree flip in the center of the head [9]. The standard scanner transmitter calibration routine can provide widely varying estimates of the transmitter calibration voltage, depending on head placement relative to isocenter and other issues. We set the transmitter calibration by hand to an expected value based on previous scans (in this case to 270 volts) and then run our B_1 Scout, which acquires a series of 6 images with different preparation pulses (Fig. 14). The RF voltage for the nominally 90 degree preparation pulse is varied from 80% of the value corresponding to the current transmitter calibration value up to 130% in 10% steps, and the entire series is obtained in 10 seconds. When this series is analyzed with the Mean Curve task card we see that the center of the head reaches a 90 degree flip angle when the transmitter calibration voltage is 270. Looking at the series of B_1 Scout images we can also see that more peripheral regions of the brain do not receive the prescribed excitation even with 130% of the manually entered transmitter calibration voltage. This is the familiar B_1^+ inhomogeneity problem, and we keep this in mind as we optimize our acquisitions during the scan session. After acquisition of localizers and the B_1 scout, the first clinical sequence we run at 7T is a 3D MPRAGE with a sagittal slice prescription (adjusted to match the head orientation as seen in the initial 3-plane localizers). The sagittal orientation and 3D nature of this first scan facilitates slice prescriptions for subsequent scans based on anatomical landmarks in the brain such as the anterior commissure – posterior commissure (AC-PC) line. Given that MPRAGE is a low SAR sequence, and that we know the transmitter reference voltage needed to reach the target flip angle in peripheral brain regions is higher than for central regions, we open the adjustments task card before running the scan and set the transmitter reference voltage to 375 for this scan. For comparison to the 3T standard, we reformat the scan into 1 mm thick axial planes, as shown in figure 15. Even with the higher resolution at 7T the SNR clearly exceeds that of the 3T image, and lengthening the inversion time (TI) to 1100 ms maintains good grey-white contrast. The 7T image clearly depicts thin perivascular spaces in the white matter which are lost in the noise in the 3T image. It should be noted, however, that while the MPRAGE sequence produces high quality T_1-weighted images at 7T, there are some issues such as loss of contrast immediately superior to the nasal and auditory sinuses (due to B_0 variation) and in the inferior temporal lobes and inferior cerebellum (due to weak RF transmit field in these regions). These artifacts may be reduced through sequence modifications [10, 11] but we have used the standard ("product") sequence here.

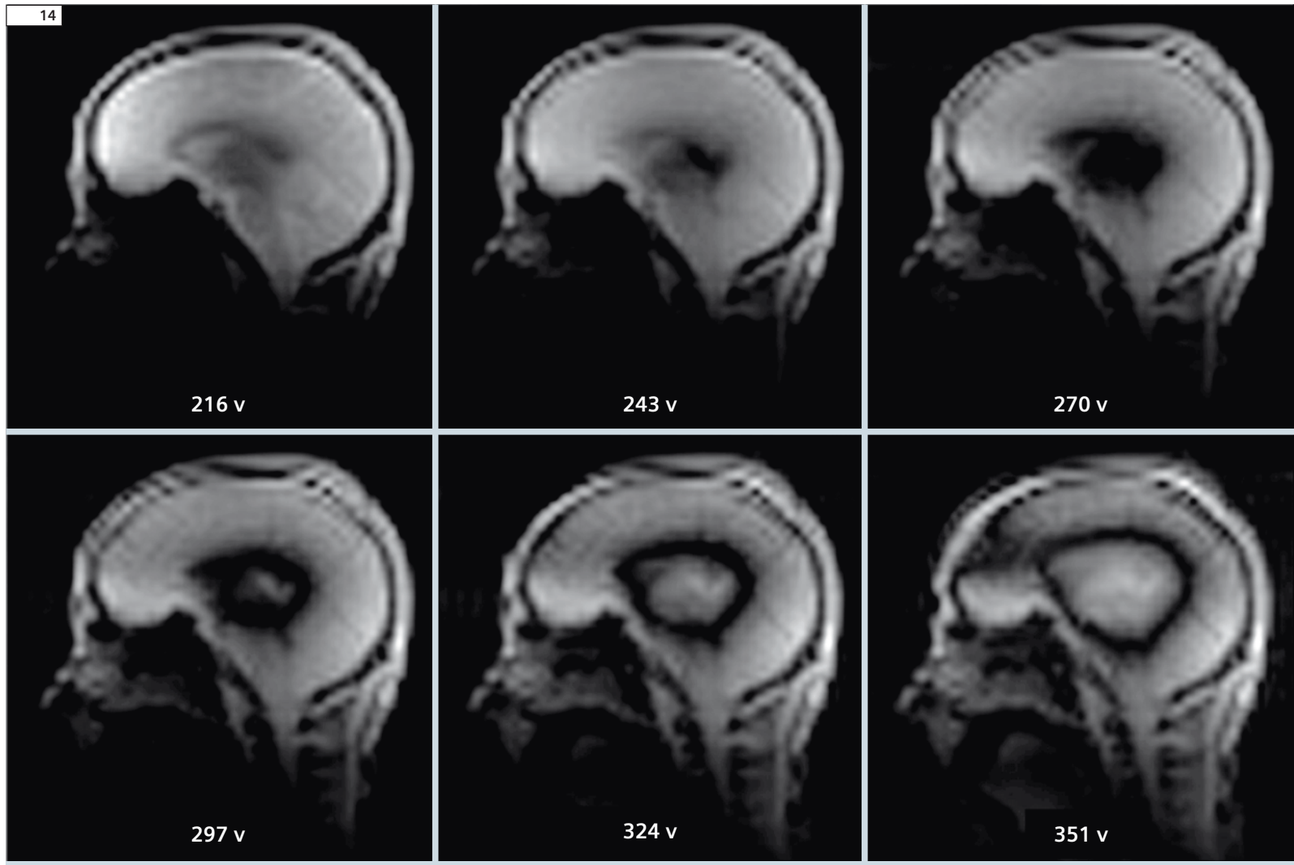

14 In-house-developed 'B_1 Scout', which applies a non-selective preparation pulse of different magnitudes before a TurboFLASH readout. The preparation pulse corresponds to 90 degrees flip at the transmitter reference voltage listed below each image. Black areas represent regions where the preparation pulse achieved a 90 degree excitation. With a transmitter reference of 270 volts we achieve the prescribed flip angle at the center of the head. (TR/TE 2000/1.3 ms, BW 2000, flip angle 8°, 4.7 x 4.7 x 8 mm^3, acquisition time 0:12 min.)

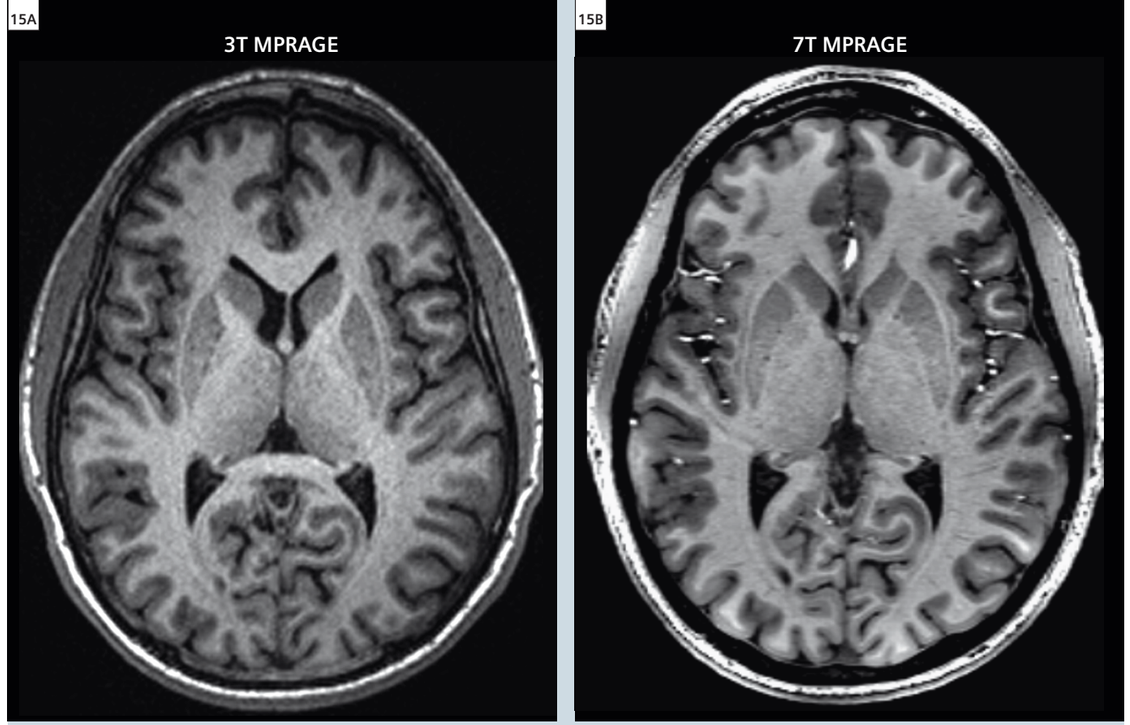

15 Comparison of 3T and 7T MPRAGE scans. Left: 3T, 1.0 x 1.0 x 1.0 mm³ isotropic resolution, acquisition time 4:31. Right: 7T, reformatted to 0.7 x 1.0 x 1.0 mm³, acquisition time 4:38.

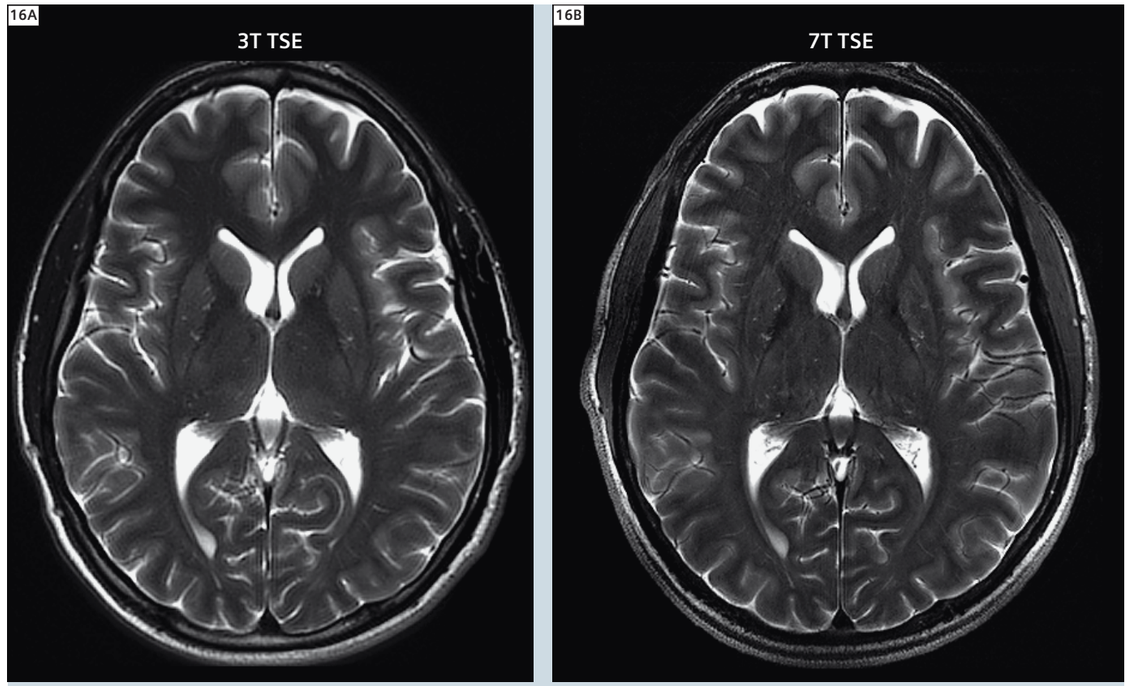

16 Comparison of 3T and 7T TSE images. Left: 3T, 0.7 x 0.7 x 5.0 mm³, 30 slices, acquisition time 3:16 min. Right: 7T, 0.5 x 0.5 x 3.5 mm, 40 slices, acquisition time 3:06 min.

The next sequence is a T_2-weighted TSE. The TSE sequence is a high SAR sequence due to its series of refocusing pulses. However, thanks to the high SNR provided by our 7T system we can lengthen TR and reduce the field of view, still reaching higher resolution than at 3T within the same total scan time. With regards to the transmitter reference voltage, here our strategy is to use the highest voltage that can be set without triggering the SAR monitor, so that we can get the full number of slices we desire. In this case we set the transmitter reference voltage to 230 volts. The comparison images (Fig. 16, details in Fig. 17) show that we have achieved very similar contrast and superior image quality with the 7T image.

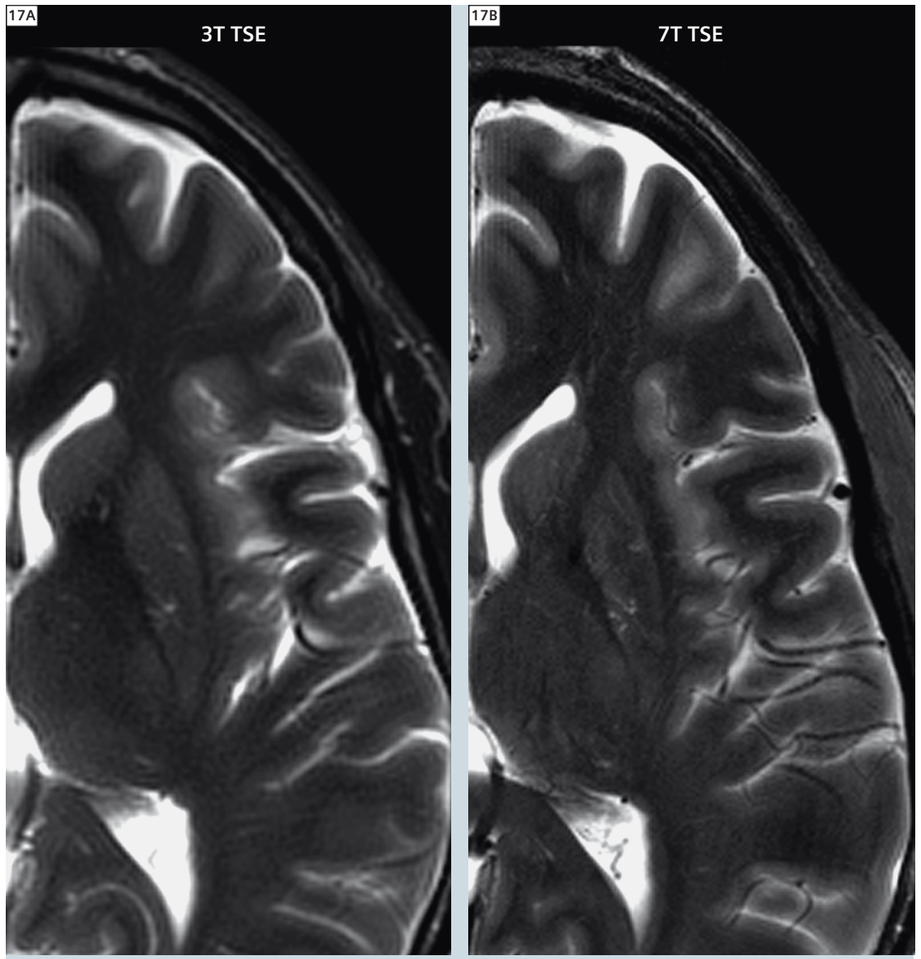

17 Details from images in Figure 16.

Standard FLAIR sequences are difficult to utilize at 7T because their inversion pulse and multiple refocusing pulses result in very high SAR. We have achieved similar image contrast to 3T FLAIR images with 2D sequences, but only with a limited number of slices in the standard scan time due to SAR restrictions. However, a Siemens works in progress (WIP) sequence is available based on the 3D SPACE sequence which provides FLAIR-like contrast. We run this at 1 mm isotropic resolution, and the scan time is roughly equivalent to the combined time taken for axial and sagittal FLAIR scans at 3T. The isotropic 7T data set can then be reformatted into any plane. With this set of parameters we are able to boost the transmitter reference voltage again without exceeding the SAR limits, in this case to 350 volts. We compare 3T images with corresponding 7T reformats in Figures 18–19. There are some differences in the contrast and image quality between the 3T and 7T scans, but with this new sequence we can add FLAIR contrast to our standard protocol at 7T. We have not yet evaluated whether the two approaches yield equivalent diagnostic information about brain lesions, but the 7T SPACE-FLAIR is a powerful addition to the array of sequences which can be run routinely at 7T.

HemoFLASH is a 2D FLASH sequence with a relatively long TE to create low signal in regions of high susceptibility, such as where there are blood products from hemorrhage or microbleeds. At 3T a TE of 20 ms is used, with a slice thickness of 5 mm. Given that T_2 in the brain is shorter at 7T than at 3T, we reduce TE to 15 ms, and also reduce the slice thickness to 3 mm to reduce signal dropout over the nasal sinus due to through-plane dephasing. Since FLASH is a low SAR sequence, we leave the transmitter reference voltage at 350. We achieved similar image contrast at higher resolution in the same total scan time as compared to 3T (Fig. 20), though there is still some signal dropout over the nasal sinus at this level of the brain. Further sequence optimization might reduce the sensitivity to susceptibility to a level more similar to 3T if desired.

Diffusion-weighted sequences are especially challenging at 7T. They are particularly susceptible to distortions due to B_0 variations, which are larger at 7T than at 3T even with diligent shimming, and the shorter T_2 at 7T leads to loss of signal because of the long readout time. Various strategies can be employed to overcome these issues, such as using higher acceleration rates with parallel imaging, and using thinner slices. We have reduced the matrix size and increased the acceleration compared to the 3T protocol, resulting in a lower in-plane resolution, and have reduced the slice thickness to 3 mm from 5 mm to reduce through-plane dephasing. SAR constraints prevented us from obtaining more than 22 slices with the nominal 270 volt transmitter reference. The 7T diffusion images shown in figure 21 are not of equal quality to those that are routinely obtained at 3T. That said, substantial research efforts have been devoted to diffusion imaging at 7T, and specialized sequences may well be able to achieve improved results [12–15].

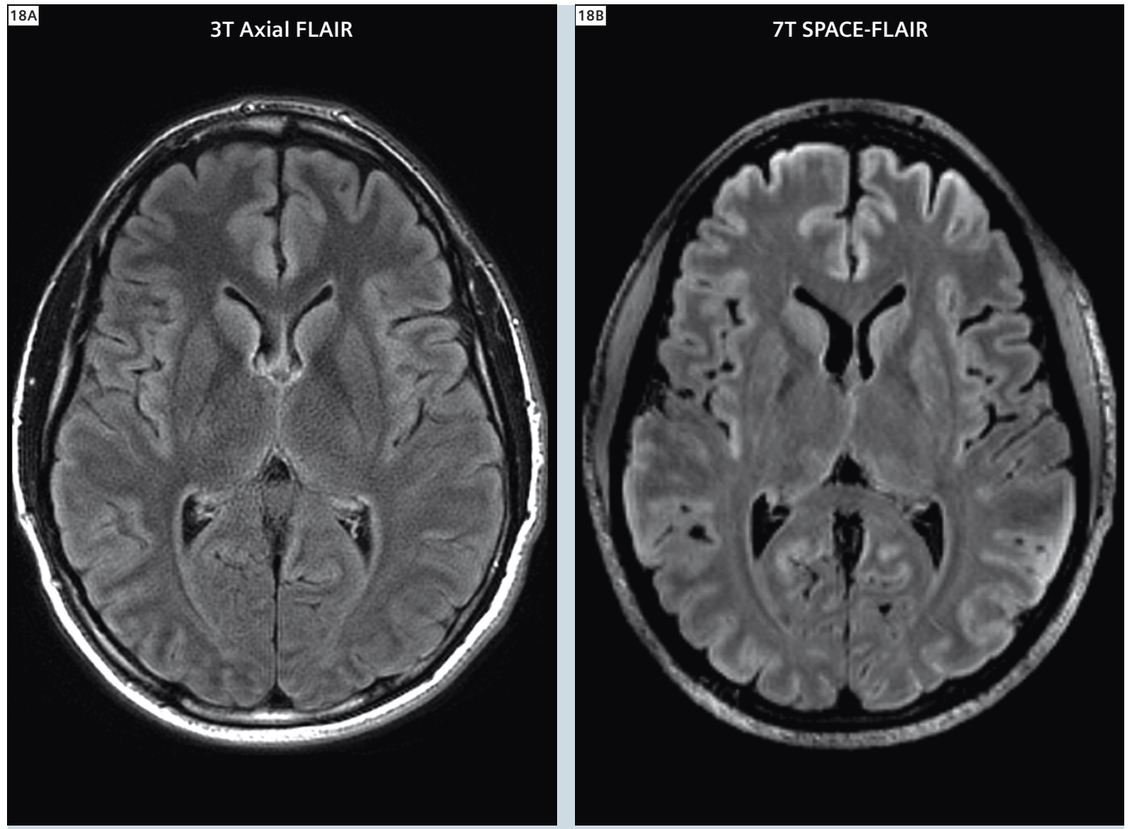

18 Comparison of 3T and 7T FLAIR images. Left: 3T axial FLAIR, 0.7 x 0.7 x 5.0 mm³, 30 slices, acquisition time 3:02 min. Right: 7T SPACE-FLAIR (3D), 1.0 x 1.0 x 1.0 mm³, 160 sagittal slices, axial reformat, acquisition time 7:22 min.

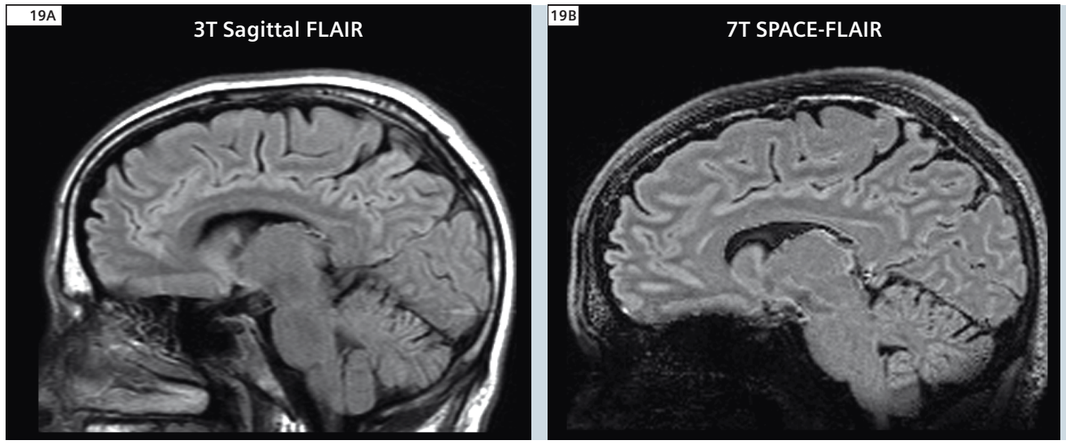

19 Comparison of 3T and 7T FLAIR images. Left: 3T sagittal FLAIR, 1.3 x 0.9 x 5.0 mm³, 30 slices, acquisition time 4:03 min. Right: 7T SPACE-FLAIR (3D), 1.0 x 1.0 x 1.0 mm³, 160 sagittal slices, native sagittal image from the same dataset as for figure 18, acquisition time 7:22 min.

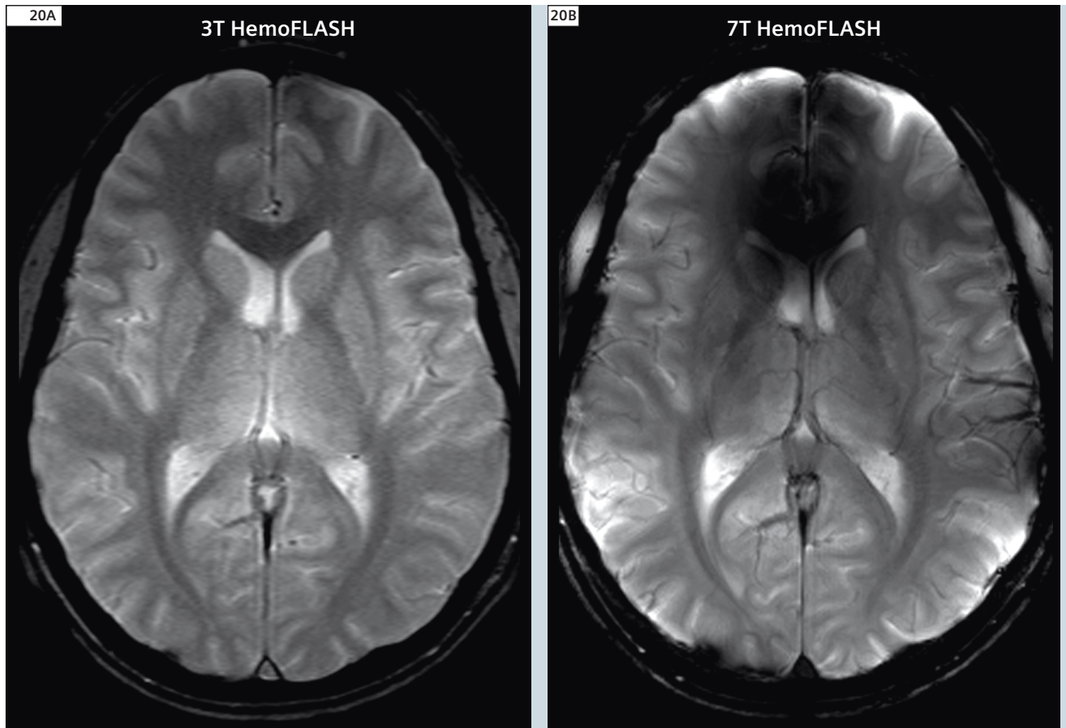

20 Comparison of 3T and 7T HemoFLASH images. Left: 3T, 1.1 x 0.7 x 5.0 mm³, 30 slices, acquisition time 2:35 min. Right: 7T, 0.7 x 0.7 x 3.0 mm³, 45 slices, acquisition time 2:38 min.

In total, not including time spent on localizers, adjustments and slice placement, the 3T protocol occupies 21 minutes 23 seconds, while the 7T protocol requires exactly 22 minutes. In these essentially equivalent times we have produced improved T_1- and T_2-weighted images at higher resolution, comparable FLAIR images, and higher-resolution HemoFLASH images which suffer from greater artifacts near regions of high susceptibility gradient than corresponding 3T images. Only with diffusion imaging do we encounter a real challenge in matching the image quality routinely obtained at 3T, consistent with the general experience that diffusion imaging requires additional optimization at 7T. There are a few caveats for the 7T protocol. To match the imaging time we often used a reduced phase field-of-view, creating a rectangular field-of-view that requires more careful placement and may not provide sufficient coverage for all heads. We have also been unable within the scope of this article to show the entire set of slices covering the whole brain, and there are a few regions in the inferior portion of the brain where susceptibility and RF inhomogeneity artifacts are more pronounced in the 7T images than in the 3T images.
Figure 22 summarizes the results just presented, illustrating graphically the near-equivalence of routine clinical image content at 3T and 7T, combined, of course, with the potential for unique information only at 7T. Note that similar imaging protocol optimizations are likely to be possible for routine musculoskeletal imaging, and further work may bring other body areas to a similar state.

Conclusions

As is evidenced by the images presented here, unique information relevant to various disease processes is currently available at 7T. There has been some hesitation in the past about clinical use of 7T, given concerns about whether traditional clinical information remained available despite changes in contrast, signal inhomogeneity, SAR limitations, etc. Here we demonstrate for a neuroimaging protocol that, with appropriate RF coils, pulse sequence modifications, and imaging protocol optimizations, 7T scanners may be used without losing most of the key clinical information content present in traditional imaging protocols at lower field strengths. This means that unique information of new clinical value may now be accessed without sacrificing routine clinical information. After a period of exploratory development, a portfolio of robust commercially-available coils is now available for 7T use. Availability of self-shielded 7T scanner designs should facilitate incorporation into hospital settings, and ongoing work on 7T body imaging should continue to expand the list of indications for 7T imaging.
In summary, the tool of 7T MRI has been carefully tuned over the past several years. And increasingly, when we are asked the question *'When will 7 Tesla scanners be ready for clinical use?'* we may finally respond: *'Bring on the patients!'*

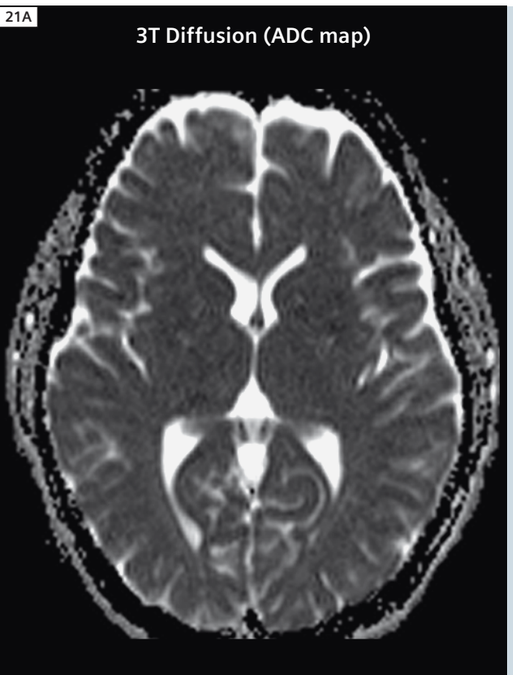

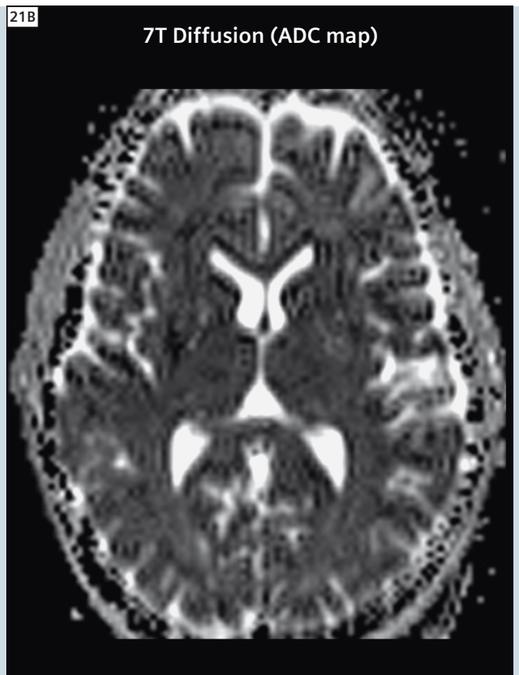

21 Comparison of apparent diffusion constant (ADC) maps at 3T and 7T. Left: 3T, 1.2 x 1.2 x 5.0 mm^3, 30 slices acquisition time 3:56 min. Right: 7T, 1.8 x 1.8 x 3.0 mm^3, 22 slices, distance factor 66%, acquisition time 4:06 min.

Acknowlegments

In addition to all of the colleagues who have generously provided images for this article, we would like to thank Dr. Christian Glaser for helpful conversations and consultations. We are also grateful to the Siemens 7T team and particularly to Bernd Stoeckel for his ongoing collaboration, motivation, and support of our 7T work.

Note on online content

Detailed pulse sequence parameters for the images and scanning protocols described in this article may be found at **www.siemens.com/magnetom-world**

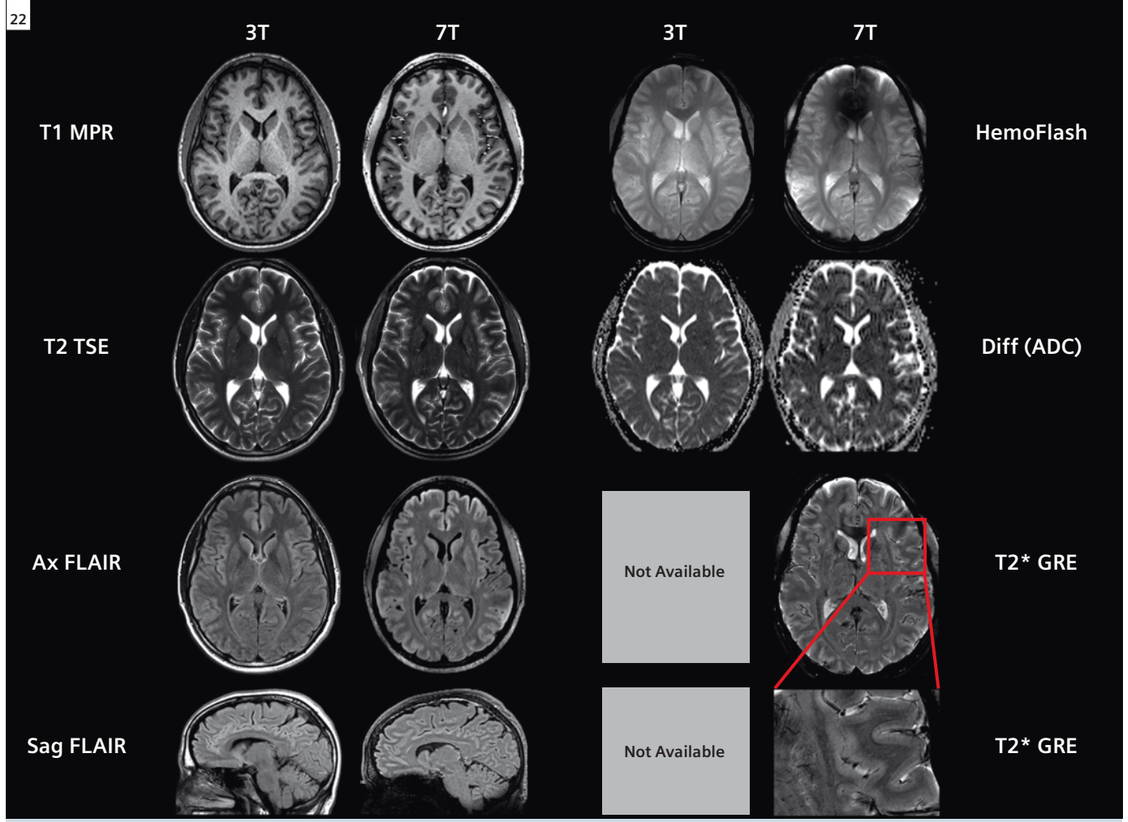

22 Summary of results from 3T and 7T neuroimaging protocols. Images at the bottom right indicate that traditional clinical information, preserved by the 7T protocol, may be supplemented by sequences which provide unique information at 7T.

References

1. Wiggins G, Zhang B, Duan Q, Lattanzi R, Biber S, Stoeckel B, McGorty K, Sodickson D. 7 Tesla Transmit-Receive Array for Carotid Imaging: Simulation and Experiment. Proceedings 17th Scientific Meeting, International Society for Magnetic Resonance in Medicine, 2009:393.
2. Finnerty M, Yang X, Zheng T, et al. A 7-Tesla High Density Transmit with 28-Channel Receive-Only Array Knee Coil. Proceedings 18th Scientific Meeting, International Society for Magnetic Resonance in Medicine. Stockholm, Sweden., 2010:642.
3. Wehrli FW, Song HK, Saha PK, Wright AC. Quantitative MRI for the assessment of bone structure and function. NMR Biomed 2006;19(7):731-64.
4. Chang G, Pakin SK, Schweitzer ME, Saha PK, Regatte RR. Adaptations in trabecular bone microarchitecture in Olympic athletes determined by 7T MRI. J Magn Reson Imaging 2008;27(5):1089-95.
5. Duan Q, Sodickson DK, Lattanzi R, Zhang B, Wiggins G. Optimizing 7T Spine Array Design through Offsetting of Transmit and Receive Elements and Quadrature Excitation. Proceedings 18th Scientific Meeting, International Society for Magnetic Resonance in Medicine. Stockholm, Sweden., 2010:51.
6. Brown R, McGorty K, Moy L, DeGregorio S, Sodickson DK, Wiggins GC. Sub-Millimeter Breast Imaging and Relaxivity Characterization at 7T. Proceedings 19th Scientific Meeting, International Society for Magnetic Resonance in Medicine. Montreal, CA, 2011:3092.
7. Prudent V, Kumar A, Liu S, Wiggins G, Malaspina D, Gonen O. Human hippocampal subfields in young adults at 7.0 T: feasibility of imaging. Radiology;254(3):900-6.
8. Mikheev A, Nevsky G, Govindan S, Grossman R, Rusinek H. Fully automatic segmentation of the brain from T1-weighted MRI using Bridge Burner algorithm. J Magn Reson Imaging 2008;27:1235-1241 (https://files.nyu.edu/hr18/public/projects.html).
9. Chung S, Kim D, Breton E, Axel L. Rapid B_1^+ mapping using a preconditioning RF pulse with TurboFLASH readout. Magn Reson Med 2010;64(2):439-46.
10. Wiggins C. A Simple Method Of Improving MPRAGE Inversion Coverage at 7T. Proceedings 15th Scientific Meeting, International Society for Magnetic Resonance in Medicine. Seattle, WA, USA, 2007:3448.
11. Marques JP, Kober T, Krueger G, W. van der Zwang W, Van de Moortele P-F, Gruetter R. MP2RAGE contrast optimization at 7T and applications. Proceedings 17th Scientific Meeting, International Society for Magnetic Resonance in Medicine. Honolulu, HI, USA, 2009:2698.
12. Mukherjee P, Hess CP, Xu D, Han ET, Kelley DA, Vigneron DB. Development and initial evaluation of 7-T q-ball imaging of the human brain. Magn Reson Imaging 2008;26(2):171-80.
13. Heidemann RM, Porter DA, Anwander A, Feiweier T, Heberlein K, Knosche TR, Turner R. Diffusion imaging in humans at 7T using readout-segmented EPI and GRAPPA. Magn Reson Med 2010;64(1):9-14.
14. von Morze C, Kelley DA, Shepherd TM, Banerjee S, Xu D, Hess CP. Reduced field-of-view diffusion-weighted imaging of the brain at 7 T. Magn Reson Imaging 2010;28(10):1541-5.
15. Sigmund EE, Gutman D. Diffusion-weighted Imaging of the Brain at 7 T with Echo-planar and Turbo Spin Echo Sequences: Preliminary Results. Magnetic Resonance Imaging 2011:in press.

Contact
Daniel K. Sodickson, MD, PhD
Vice-Chair for Research, Department of Radiology
Director, Center for Biomedical Imaging
New York University Langone Medical Center
660 First Avenue, Fourth Floor
New York, NY 10016
USA
Phone: +1 212-263-4844
Daniel.Sodickson@med.nyu.edu

Not for distribution in the US.

Body Imaging at 7 Tesla with Multichannel Transmit Capability

K. Ugurbil[1]; J.T. Vaughan[1]; G.J. Metzger[1]; P.-F. van de Moortele[1]; C.J. Snyder[1]; L. DelaBarre[1]; P. Bolan[1]; E Auerbach[1]; P. Weale[2]; S. Zuehlsdorff[2]; S. Nielles-Vallespin[2,3]; R. Jerecic[2]

[1]*Center for Magnetic Resonance Research (CMRR), Dept. of Radiology, University of Minnesota, Minneapolis, USA*
[2]*Siemens Healthcare*
[3]*Current address: Royal Brompton Hospital, London, UK*

In the last two decades, a plethora of magnetic resonance (MR) techniques, such as functional magnetic resonance imaging (fMRI), have come to play an indispensable role in the neurosciences. In our laboratory, the Center for Magnetic Resonance Research (CMRR) at the University of Minnesota, the evolution of such methods has been intricately tied with the development of high field MR, starting with the installation of one of the first three 4 Tesla (T) scanners in approximately 1990, followed by the establishment of the very first 7 Tesla system in 1999 (e.g. reviews [1–5]). The development of this 7T scanner for human imaging was justified based on the results of numerous human and animal model studies conducted at 4 and 9.4T, respectively, in our lab through the mid-nineties. These studies demonstrated that despite many contravening notions of the time, high magnetic fields could provide significant advantages. Using this first ultra-high[1] field 7T system, we were able to demonstrate that challenges faced at such field strengths in human imaging could be overcome. Although it is taken for granted today, at the time we started working with 7T, even field-dependent signal-to-noise ratio (SNR) gains in the human head were questioned. In one of first 7T studies, however, we were able to experimentally demonstrate for the first time that SNR does increase with magnetic field in the human head, though this increase was complex and spatially non-uniform [6]. More importantly, over the years, 7T has been shown to provide unique anatomical, functional and physiologic information beyond just gains in SNR (e.g. [7–11]). With the rapidly increasing number of recent 7T installations, demonstration of such unique uses of ultra-high fields is also rapidly blooming. For approximately a decade, 7T studies were restricted to the human head. Ever since the discouraging early 4T results from manufacturers' laboratories [12], the human torso has been considered too difficult to tackle at ultra-high fields. The large B_1 and signal intensity inhomogeneities noted in these early 4T head and body images were ascribed to "dielectric resonances". However, some of the first experiments we conducted at 7T to understand the RF behavior in the human body at the proton Larmor frequency at this field strength (300 MHz) indicated that we are not dealing with a "resonance" phenomenon. Rather, in a paper we and our collaborators from Penn State University published in 2001 [13], we concluded that 300 MHz RF behaves as a damped traveling wave in the human body and that (to quote from our original paper) "the characteristic image intensity distribution in the human head is the result of spatial phase distribution and amplitude modulation by the interference of the RF traveling waves determined by a given sample-coil configuration". Later studies further confirmed that when the object size exceeds the wavelength of the RF used, we operate in the damped traveling wave regime, leading to large and spatially rapid phase variations over the object, resulting in destructive interferences [14] and these destructive interferences are responsible for the spatially non-uniform SNR gains that was noted in our earlier study [6]. This was in fact good news: Resonance phenomena are difficult to deal with for recovering signal where there is virtually none; but destructive interferences due to traveling waves can be managed to extract full SNR gains intrinsically provided by increasing magnetic fields.
This complex RF behavior at ultra-high fields in fact turns out to be a major advantage for signal reception, leading to significantly better parallel imaging performance on the receive side at 7T or above. Thus, as the magnetic field increases, spatial encoding information provided by the receive array replaces k-space data to a larger extend due to the complex RF phase and amplitude over the sample [15–17]. However, the consequences of damped traveling wave behavior is a major problem on the transmit side and it is particularly severe in the human body where the object size is 4 to 6 (or more) times larger than the 300 MHz wavelength, which is ~12 cm in human tissues such as muscle and brain.

Figure 1 illustrates electro-dynamic simulations taken from our recent paper [18] for the human body at 7T: The RF field and SAR were modeled by the finite difference time domain (FDTD) method, for a "body" coil at 7T with and without the human body loading the coil.
The circularly polarized transmit B_1 (i.e. B_1^+) field magnitude generated in the unloaded body coil shown in figure 1 was *uniform* in a cylindrical volume with a length slightly less than the length of the resonant elements in this coil (33 cm). The axial plane shown in figure 1 (top row, left) is for a slice in the center of this volume. Despite the uniformity of B_1^+ in the *unloaded* coil, upon loading with a human body, the magnetic field and consequently power deposition becomes extremely non-uniform (Fig. 1, lower part). There are regions in the center of the body where there is virtually no RF (light blue color). Note that highest intensity of the B_1^+ and the largest SAR is in the human head, even though the head is significantly outside the coil and that when unloaded the coil does not have any significant B_1^+ in the region where the head is.
Our solution to the destructive interferences induced by traveling waves has been the use of multichannel parallel transmit (pTx) with channel-specific independent control [19–22, 18]. With this approach, the B_1^+ fields can be targeted and homogenized over a predefined region, enabling body imaging for the first time in the human torso at 7T [23, 24, 18]. The strategy is not to aim for a homogeneous image over the entire slice but rather over the targeted organ. Figure 2 illustrates the cardiac set-up, the B_1^+ distribution before and after B_1^+ optimization over the heart (images in color) and the resultant cardiac image at 7T. In this approach, we employ a dual 8-channel transmit and receive array placed one above and one below the human torso for a total of 16 transmit and receive elements (Fig. 2). Excellent quality cardiac images were also obtained using a more traditional circumscribing TEM body coil but driven as a 16-channel transmit and receive array [18]. Two cardiac imaging examples from such a body coil are illustrated in figure 3. Functional cardiac cines of these and other cardiac images can be found at http://www.cmrr.umn.edu/research/videos/. We have had similar success with imaging the prostate [23] and the kidney (unpublished results), demonstrating the feasibility of excellent high resolution torso imaging at 7T (Fig. 3). So far, we have employed multichannel transmit only for "B_1^+shimming" but not for generating spatially targeted pulses (e.g. [25–28]) using transmit SENSE principles [29, 30]. In the B_1^+shimming approach, all pTx channels transmit the same RF pulse waveform but with differing phases and/or amplitudes. This approach is particularly suitable in body imaging where the targeted organ is often much smaller then the dimensions of the torso, which dictates the dimensions of the RF transmit array to be used. When the target covers a small portion of the entire field of view, optimizing the B_1^+ over this target in fact results in decreases in power deposition (SAR) [23], which is a major confound at ultra-high field applications. Spatially tailored pulses, on the other hand rely on different modulation patterns on each channel, which can be generated on the Siemens pTx system. Such pulses have been known

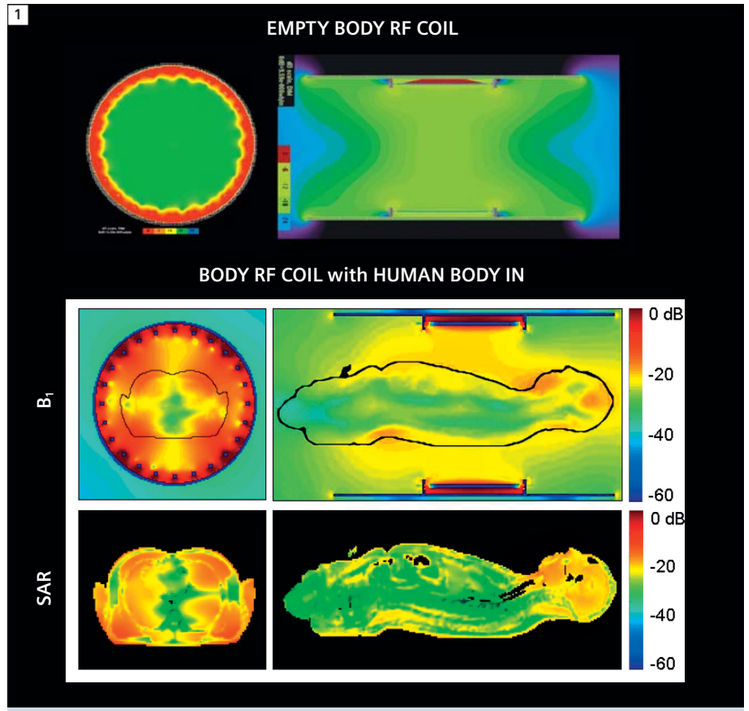

1 B_1 and SAR calculations for a TEM Body RF coil tuned to 300 MHz with and without the human body in the coil. The body model used was derived from the National Library of Medicine (NLM) Visual Human digital atlas whose segmented anatomy was adjusted to match the conductivity and permittivity of tissues at 300 MHz. The coil was driven at four ports (45°, 135°, 225°, and 315°).

[1] The radiofrequency band 300 MHz to 3 GHz is defined as Ultra high frequency (UHF) (see http://en.wikipedia.org/wiki/Ultra_high_frequency). The hydrogen nucleus resonance frequency at 7T is 300 MHz i.e. in UHF band. Therefore, 7T to 70T can be defined as Ultra High Field (UHF).

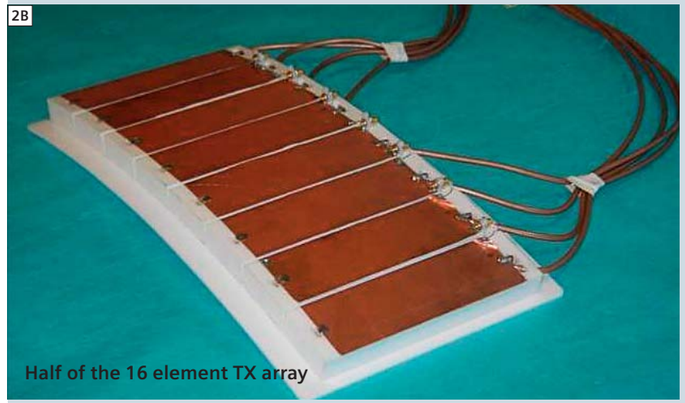

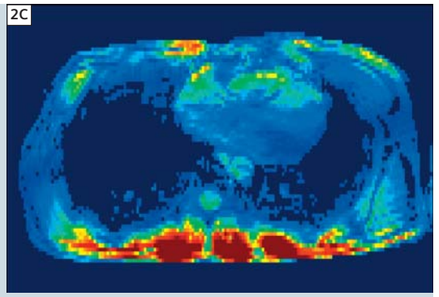

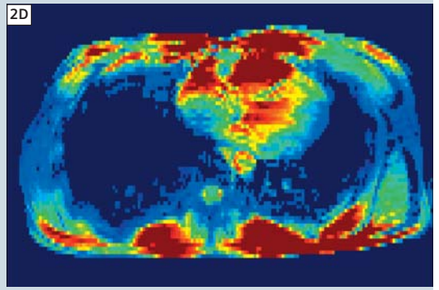

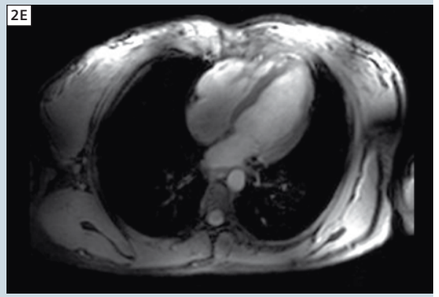

2 The multichannel transmit and receive array coil that is used for body imaging at 7T. Only the 8 elements positioned superior to the subject are shown. An identical unit is placed below the subject. The images in color display the B_1^+ map before and after optimization over the heart. Lower right shows the resulting cardiac image at 7T. TR/TE=45/3.06 ms; 2.0 x 2.0 x 5.5 mm resolution; Matrix size 144 x 192; Breath held and ECG retrogated; Snyder, et. al. MRM 61, 517 (2009); Vaughan, et. al. MRM 61, 244 (2009)

for some time; however, they are typically very long when applied with a single transmit channel and as such not practical in most human applications. The use of pTx capability, however, enables the spatial encoding to be performed in part by the coil transmit sensitivity profiles, leading to a significant shortening of the pulse. This shortening, however, results in substantial increases in peak voltage that must be used, and hence SAR. Strategies to control this SAR amplification are pursued in several laboratories and will be critical in successfully using this approach. The number of channels employed likely plays an important role in SAR deposition with pTx applications. Just as in spatial encoding with multichannel receive to replace k-space encoding [15–17], spatial encoding to shorten the k-space trajectory in spatially targeted RF pulses works much more efficiently as the relative object size gets larger. Thus, the acceleration factors that can be achieved to shorten otherwise extremely long, and, as such, impractical pulses also improve with higher magnetic fields and with a larger object size. Thus, one solution to the ultra-high field transmit RF non-uniformity problem is actually a strategy that works particularly well in ultra-high fields. Provided that SAR limitations can be overcome, spatially targeted pulses applied using pTx introduces the possibility of applications beyond just B_1 flattening, such as restricted FOV

Not for distribution in the US.

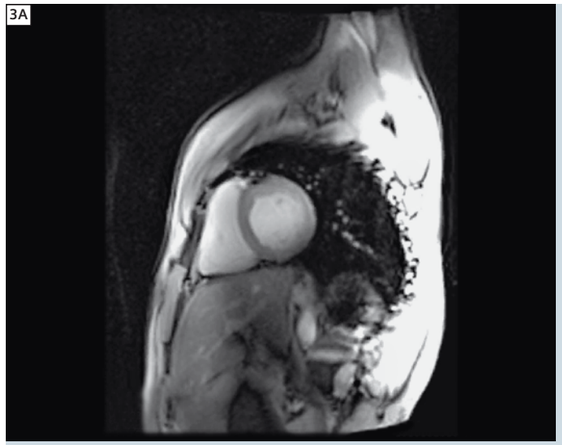

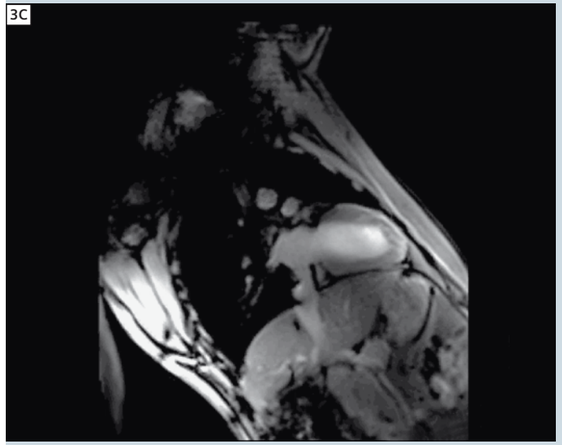

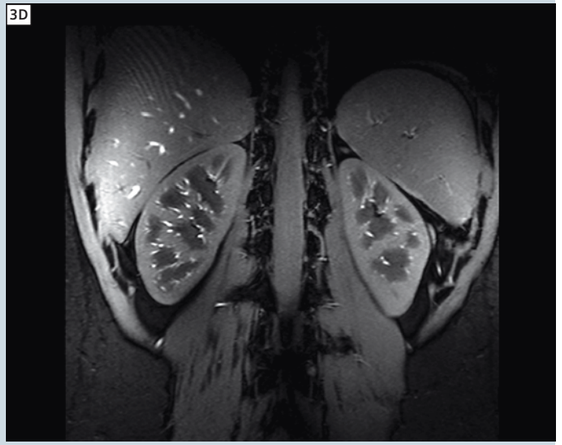

3 7T body images with targeted B_1 shimming using 16-channel pTx capability; cardiac images (on two different planes), a transaxial image through the torso at the level of prostate and a coronal plane through the kidneys obtained using pTx and multichannel receive technology. Note that while there exists strong non-uniformities in the entire image, the image over the targeted organ(s) (heart, prostate and kidneys) is relatively uniform.

"zoomed" imaging, vessel selective angiography etc.
These initial results are a prelude to dramatic improvements that are sure to come in body imaging using pTx methodology and enabling the exploitation of advantages provided by ultrahigh fields, such as improved SNR, improved contrast in many instances, longer T1 times of blood, and improved parallel imaging. In particular, many SNR limited applications in the body, such as angiography and perfusion imaging without using an exogenous contrast agent, vessel wall imaging, high resolution imaging of pathology and of musculoskeletal structures and high resolution spectroscopy, to name a few potential applications, will come to exist and will be further enhanced even at higher magnetic fields. Finally, it is inevitable that these successes will impact, in some fashion, how we do body imaging at the lower magnetic field of 3 or even 1.5T.

Contact
Professor Kamil Ugurbil, Ph.D.
Center for Magnetic Resonance Research
Dept. of Radiology
University of Minnesota
Minneapolis, 55455
USA
kamil@cmrr.umn.edu

References

1 Ugurbil, K., G. Adriany, P. Andersen, W. Chen, M. Garwood, R. Gruetter, P.G. Henry, S.G. Kim, H. Lieu, I. Tkac, T. Vaughan, P.F. Van De Moortele, E. Yacoub, and X.H. Zhu, *Ultrahigh field magnetic resonance imaging and spectroscopy. Magn Reson Imaging,* 2003. 21(10): p. 1263–81.

2 Ugurbil, K., L. Toth, and D.S. Kim, *How accurate is magnetic resonance imaging of brain function?* Trends Neurosci, 2003. 26(2): p. 108–14.

3 Harel, N., K. Ugurbil, K. Uludag, and E. Yacoub, *Frontiers of brain mapping using MRI.* J Magn Reson Imaging, 2006. 23(6): p. 945–57.

4 Ugurbil, K., G. Adriany, C. Akgün, P. Andersen, W. Chen, M. Garwood, R. Gruetter, P.-G. Henry, M. Marjanska, S. Moeller, P.-F. Van de Moortele, K. Prüssmann, I. Tkac, J.T. Vaughan, F. Wiesinger, E. Yacoub, and X.-H. Zhu, *High Magnetic Fields for Imaging Cerebral Morphology, Function and Biochemistry, in Biological Magnetic Resonance: Ultra High Field Magnetic Resonance Imaging*, P.M.L. Robitaille, and Berliner, L.J., Editor. 2006, Springer: New York. p. 285–342.

5 Ugurbil, K., W. Chen, N. Harel, P.-F. Van de Moortele, E. Yacoub, X.H. Zhu, and K. Uludag, *Brain Function, Magnetic Resonance Imaging of, in Wiley Encyclopedia of Biomedical Engineering*, M. Akay, Editor. 2006, John Wiley & Sons, Inc: Hoboken. p. 647–668.

6 Vaughan, J.T., M. Garwood, C.M. Collins, W. Liu, L. DelaBarre, G. Adriany, P. Andersen, H. Merkle, R. Goebel, M.B. Smith, and K. Ugurbil, *7T vs. 4T: RF power, homogeneity, and signal-to-noise comparison in head images.* Magn Reson Med, 2001. 46(1): p. 24–30.

7 Duyn, J.H., P. van Gelderen, T.Q. Li, J.A. de Zwart, A.P. Koretsky, and M. Fukunaga, *High-field MRI of brain cortical substructure based on signal phase.* Proc Natl Acad Sci U S A, 2007. 104(28): p. 11796–801.

8 Rooney, W.D., G. Johnson, X. Li, E.R. Cohen, S.G. Kim, K. Ugurbil, and C.S. Springer, Jr., *Magnetic field and tissue dependencies of human brain longitudinal 1H2O relaxation in vivo.* Magn Reson Med, 2007. 57(2): p. 308–18.

9 Yacoub, E., A. Shmuel, N. Logothetis, and K. Ugurbil, *Robust detection of ocular dominance columns in humans using Hahn Spin Echo BOLD functional MRI at 7 Tesla.* Neuroimage, 2007. 37(4): p. 1161–77.

10 Cho, Z.H., C.K. Kang, J.Y. Han, S.H. Kim, K.N. Kim, S.M. Hong, C.W. Park, and Y.B. Kim, *Observation of the lenticulostriate arteries in the human brain in vivo using 7.0T MR angiography.* Stroke, 2008. 39(5): p. 1604–6.

11 Yacoub, E., N. Harel, and K. Ugurbil, *High-field fMRI unveils orientation columns in humans.* Proc Natl Acad Sci U S A, 2008. 105(30): p. 10607–12.

12 Barfuss, H., H. Fischer, D. Hentschel, R. Ladebeck, A. Oppelt, R. Wittig, W. Duerr, and R. Oppelt, *In vivo magnetic resonance imaging and spectroscopy of humans with a 4 T whole-body magnet.* NMR Biomed, 1990. 3(1): p. 31–45.

13 Yang, Q.X., J. Wang, X. Zhang, C.M. Collins, M.B. Smith, H. Liu, X.H. Zhu, J.T. Vaughan, K. Ugurbil, and W. Chen, *Analysis of wave behavior in lossy dielectric samples at high field.* Magn Reson Med, 2002. 47(5): p. 982–989.

14 Van de Moortele, P.F., C. Akgun, G. Adriany, S. Moeller, J. Ritter, C.M. Collins, M.B. Smith, J.T. Vaughan, and K. *Ugurbil, B(1) destructive interferences and spatial phase patterns at 7 T with a head transceiver array coil.* Magn Reson Med, 2005. 54(6): p. 1503–18.

15 Ohliger, M.A., A.K. Grant, and D.K. Sodickson, *Ultimate intrinsic signal-to-noise ratio for parallel MRI: electromagnetic field considerations.* Magn Reson Med, 2003. 50(5): p. 1018–30.

16 Wiesinger, F., P.F. Van de Moortele, G. Adriany, N. De Zanche, K. Ugurbil, and K.P. Pruessmann, *Parallel imaging performance as a function of field strength--an experimental investigation using electrodynamic scaling.* Magn Reson Med, 2004. 52(5): p. 953–64.

17 Wiesinger, F., P.F. Van de Moortele, G. Adriany, N. De Zanche, K. Ugurbil, and K.P. Pruessmann, *Potential and feasibility of parallel MRI at high field.* NMR Biomed, 2006. 19(3): p. 368–78.

18 Vaughan, J.T., C.J. Snyder, L.J. DelaBarre, P.J. Bolan, J. Tian, L. Bolinger, G. Adriany, P. Andersen, J. Strupp, and K. Ugurbil, *Whole-body imaging at 7T: preliminary results.* Magn Reson Med, 2009. 61(1): p. 244–8.

19 Vaughan, J., RF coil for imaging system. 2003: USA patent 6,633,161.

20 Adriany, G., P.F. Van de Moortele, F. Wiesinger, S. Moeller, J.P. Strupp, P. Andersen, C. Snyder, X. Zhang, W. Chen, K.P. Pruessmann, P. Boesiger, T. Vaughan, and K. Ugurbil, *Transmit and receive transmission line arrays for 7 Tesla parallel imaging.* Magn Reson Med, 2005. 53(2): p. 434–445.

21 Vaughan, J., G. Adriany, K. Ugurbil, J. Strupp, and P. Andersen, *University of Minnesota, assignee. Parallel Transceiver for Nuclear Magnetic Resonance System.* 2005, University of Minnesota: USA 6,969,992.

22 Vaughan, T., L. DelaBarre, C. Snyder, J. Tian, C. Akgun, D. Shrivastava, W. Liu, C. Olson, G. Adriany, J. Strupp, P. Andersen, A. Gopinath, P.F. van de Moortele, M. Garwood, and K. Ugurbil, *9.4T human MRI: preliminary results.* Magn Reson Med, 2006. 56(6): p. 1274–82.

23 Metzger, G.J., C. Snyder, C. Akgun, T. Vaughan, K. Ugurbil, and P.F. Van de Moortele, *Local B_1^+ shimming for prostate imaging with transceiver arrays at 7T based on subject-dependent transmit phase measurements.* Magn Reson Med, 2008. 59(2): p. 396–409.

24 Snyder, C.J., L. DelaBarre, G.J. Metzger, P.F. van de Moortele, C. Akgun, K. Ugurbil, and J.T. Vaughan, *Initial results of cardiac imaging at 7 Tesla.* Magn Reson Med, 2009. 61(3): p. 517–24.

25 Setsompop, K., L.L. Wald, V. Alagappan, B. Gagoski, F. Hebrank, U. Fontius, F. Schmitt, and E. Adalsteinsson, *Parallel RF transmission with eight channels at 3 Tesla.* Magn Reson Med, 2006. 56(5): p. 1163–71.

26 Setsompop, K., V. Alagappan, A.C. Zelinski, A. Potthast, U. Fontius, F. Hebrank, F. Schmitt, L.L. Wald, and E. Adalsteinsson, *High-flip-angle slice-selective parallel RF transmission with 8 channels at 7 T.* J Magn Reson, 2008. 195(1): p. 76–84.

27 Zelinski, A.C., L.L. Wald, K. Setsompop, V. Alagappan, B.A. Gagoski, V.K. Goyal, and E. Adalsteinsson, *Fast slice-selective radio-frequency excitation pulses for mitigating B+1 inhomogeneity in the human brain at 7 Tesla.* Magn Reson Med, 2008. 59(6): p. 1355–64.

28 Wu, X., J.T. Vaughan, K. Ugurbil, and P.F. Van de Moortele, *Parallel excitation in the human brain at 9.4 T counteracting k-space errors with RF pulse design.* Magn Reson Med, 2010. 63(2): p. 524–9.

29 Katscher, U., P. Bornert, C. Leussler, and J.S. van den Brink, *Transmit SENSE.* Magn Reson Med, 2003. 49(1): p. 144–50.

30 Grissom, W.A., C.-Y. Yip, and D.C. Noll, *An image domain approach for the design of RF pulses in transmit SENSE.* Proc. Intl. Soc. Mag. Reson. Med., 2005. 13: p. 19.

Not for distribution in the US.

Specific Absorption Rate (SAR) in Parallel Transmission (pTx)

Lawrence L. Wald[1]; Elfar Adalsteinsson[1,2]

[1]*Athinoula A. Martinos Center for Biomedical Imaging, Department of Radiology, Massachusetts General Hospital. Harvard Medical School and Harvard-MIT Division of Health Sciences and Technology, Boston, MA, USA*
[2]*Department of Electrical Engineering and Computer Science, Massachusetts Institute of Technology, Boston, MA, USA*

Introduction

Parallel transmission (pTx) uses multiple excitation coils driven by independent RF pulse waveforms to subdivide the transmit field into multiple spatial regions each controlled by a separate transmit channel. Increasing the number of spatially distinct transmit elements and temporally distinct RF pulse waveforms compared to conventional single-channel RF systems creates spatial degrees of freedom that allow the spatial information in the array to be exploited in the excitation process. Previous pTx work has concentrated on the potential to utilize this additional flexibility in spatial information to move beyond the uniform slice-select excitation to generate spatially tailored RF pulses; excitation pulses with a carefully controlled spatially varying flip angle pattern or excitation phase that can mitigate artifacts or isolate specific anatomy. Operating in analogy to parallel reception, parallel transmission offers the possibility to move beyond the uniform slice-select excitation and create a more anatomy-specific excitation which could mitigate drop-out regions from inhomogeneous excitation fields at 3T or 7T, reduce image encoding needs (e.g. for cardiac or shoulder imaging) by reducing the needed field-of-view, allow selective spin-tagging excitations (potentially allowing vessel territory perfusion imaging), or simply provide clinically useful but non-traditional excitations such as curved saturation bands for the spine or brain.

While the development of these novel RF pulse designs and applications continue to be an area of intense development, the clinical utility of a given RF excitation pulse is characterized by more than just its spatial fidelity. The Specific Absorption Rate (SAR) of an excitation pulse is often the critical limiting factor when applied to a clinical imaging sequence. The need to stay below safe SAR limits often requires unfavorable tradeoffs in acquisition parameters such as increased TR or reduced flip angle. This is especially problematic at 3T, where the power needed for a given flip angle increases as much as 4 fold compared to 1.5T applications, and thus the SAR ceiling is acutely felt.

Fortunately, while the use of parallel transmission creates some SAR problems of its own (such as the need to carefully monitor for local SAR hotspots in a specific RF pulse design), the spatial degrees of freedom that give rise to the wealth of spatial design potential also offers novel opportunities for SAR manipulation. While attempts to minimize SAR during the design of parallel transmit pulses has been ongoing since the first pTx papers, the full potential of our ability to manipulate these degrees of freedom as well as the engineering solutions needed to realize SAR reduction and management via pTx are just appearing.

In this article we review some of the progress which has been made toward strategies for reducing SAR with pTx in a prototype Siemens MAGNETOM Trio, a Tim System, and a MAGNETOM 7T. We review the pTx SAR problem and discuss some of the recent advances in calculating parallel transmit RF pulses for spatially tailored excitation with optimization methods which penalize global and local SAR. Further, we describe some recent advances in real-time SAR monitoring as well as outstanding issues that must be overcome for routine application.

SAR in spatially tailored excitations

To achieve an arbitrary spatial flip angle distribution after excitation, we modulate the RF waveform in amplitude and phase during a time-varying gradient waveform. These "spatially tailored" RF excitations have been pursued for more than two decades [1]. The design procedure is illustrated in figure 1, where the Fourier transform of the desired pattern is sampled on a spiral excitation k-space trajectory to produce the amplitude and phase modulations needed during the gradient waveform.

Although spatially tailored excitation pulses are easily demonstrated, there are serious engineering challenges to their routine and practical use. First and foremost is the lengthy and largely impractical encoding period needed (as long as 50 ms). Parallel excitation directly addresses this problem by allowing the

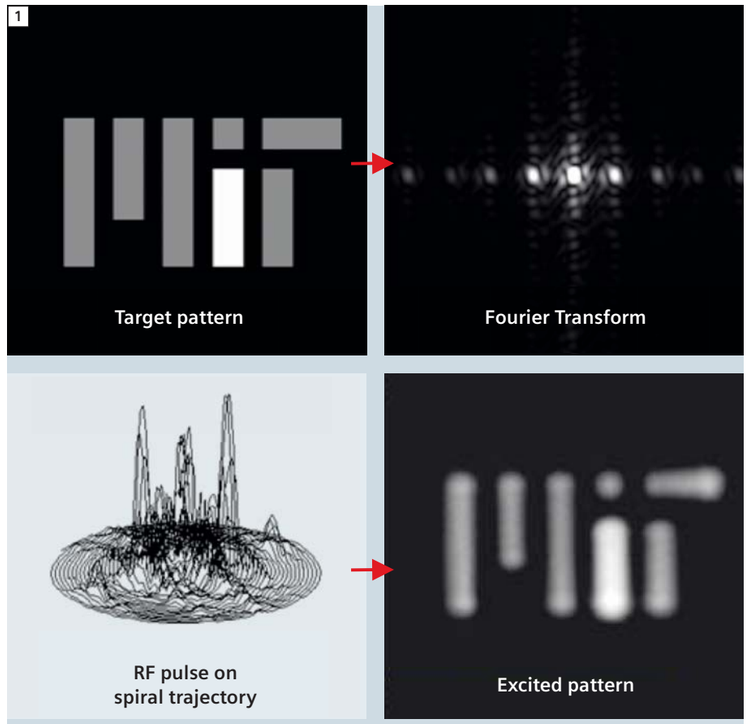

1 The design of a spatially tailored excitation starts with a choice of a spatial target pattern (in this case the MIT logo), and a gradient trajectory such as the spiral trajectory shown. The Fourier transform of the target pattern is used to modulate the amplitude and phase of the RF excitation waveform to achieve the desired distribution in excitation k-space. The RF waveform is played out during the gradient trajectory resulting in the desired excited magnetization pattern.

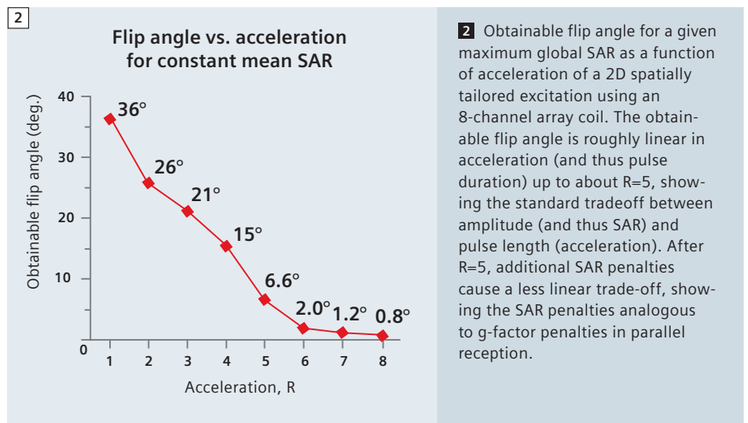

2 Obtainable flip angle for a given maximum global SAR as a function of acceleration of a 2D spatially tailored excitation using an 8-channel array coil. The obtainable flip angle is roughly linear in acceleration (and thus pulse duration) up to about R=5, showing the standard tradeoff between amplitude (and thus SAR) and pulse length (acceleration). After R=5, additional SAR penalties cause a less linear trade-off, showing the SAR penalties analogous to g-factor penalties in parallel reception.

"excitation k-space" trajectory to be undersampled, analogous to the reductions in encoding trajectory steps in parallel reception, but with some interesting contrasting properties. For instance, in accelerated parallel reception we are often limited by the image Signal-to-Noise Ratio (SNR) losses associated with the procedure. In parallel transmission, the RF waveforms take the position mathematically analogous to the final image in parallel reception and start with extraordinary high SNR since they are generated with robust digital-to-analog technology. Therefore, even with a modest 8-channel transmit array, we can reduce the duration of the pulse up to 6 fold without suffering from noise enhancement of the calculated RF pulse waveforms [2, 3]. Note that this level of acceleration would be difficult to achieve in parallel reception.

Instead, it is the SAR of the excitation that constitutes the limiting penalty in accelerating spatially tailored excitations with parallel transmission, with a secondary limitation arising from artifacts in the transmitted pattern due to imperfect knowledge of the array coil excitation profiles. The dramatic increase in SAR with acceleration can be understood intuitively. First, as the pulse length is reduced, the amplitude must be increased accordingly to achieve a given pulse area (flip angle). Increases in pulse amplitudes are expensive in SAR since the SAR increases with the square of the applied RF voltage. As a square pulse is shortened, the pulse amplitude must be increased linearly to maintain a given flip angle (pulse area). The instantaneous SAR thus increases inversely with the square of the duration, and the SAR associated with the use of this pulse within a fixed TR pulse sequence also increases linearly. Figure 2 demonstrates this effect for an eight-channel loop array at 7T as a nearly linear decrease in obtainable flip angle for a given global SAR value as a spatially tailored 2D excitation is accelerated by factor R via undersampling of its excitation k-space trajectory.

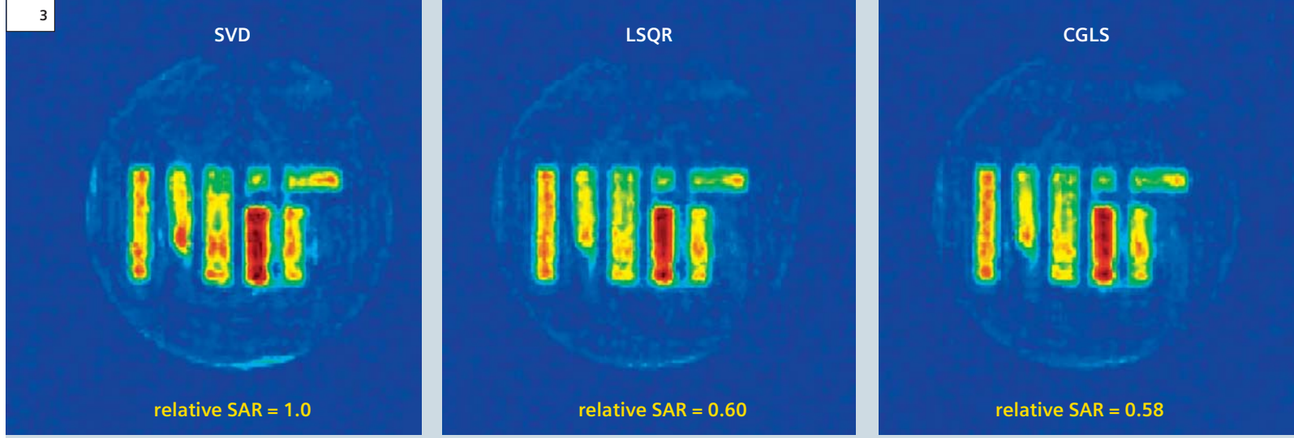

3 Accelerated spiral trajectory pulses with R=4 acceleration with approximately equal RMSE compared to the target pattern ("MIT" logo), but with the least-squares optimization performed with either the SVD, LSQR or CGLS method. In this case the global SAR was considerably lower for the LSQR or CGLS method compared to SVD. During the original work, we did not analyze the local SAR pattern, but now hypothesize that the local SAR pattern will be even more different among the three solutions.

Second, the impressive spatial definition of pTx excitation patterns obtained by these pulses come at a cost in SAR. The spatial pattern is achieved by temporally modulating the RF pulse in the presence of time-varying gradient waveforms, causing phase shifts in the excited magnetization that superimpose over time to achieve the desired pattern. Unfortunately, temporally modulating a pulse in amplitude or phase tends to create instances of higher peak power (as well temporal nulls in the pulse voltage) as the RF pulse deposits the requisite energy along the traversed excitation trajectory. Again the fact that instantaneous SAR is proportional to the square of the pulse waveform enhances the problem. Due to the nonlinear relationship between pulse amplitude and instantaneous SAR, the nulls do not counterbalance the increased peak values when the SAR is integrated over the pulse duration. This leads to increased SAR whenever a pulse is temporally modulated.

When the spatially tailored excitation strategy is generalized to multiple RF excitation channels, the excitation pattern is not simply the Fourier transform of the excitation k-space, but is determined from a linear model of the undersampled Fourier encoding and the spatial profiles of the transmit coils. This over-determined linear model is inverted to yield the needed RF waveforms. The optimization process used to invert the over-determined linear problem also gives rise to procedures for managing SAR. The simplest cost function for the optimization includes only a cost for the difference between actual excitation pattern and the original target. It is also straight forward to include a cost for the average pulse amplitude, thus acknowledging the cost of increased global SAR in the optimization. An obvious choice would be to also penalize local SAR by including the peak local SAR value in the cost function. Methods for rendering this latter approach computationally tractable are discussed below.

Aside from direct regularization procedures for global and local SAR such as the cost function modifications mentioned above, the pulse optimization offers multiple other possibilities for controlling local and global SAR. The next sections illustrate some of the approaches being pursued.

One-pulse design problem; many solutions

The first insight into controlling local and global SAR comes from the observation that the linear optimization problem generates many possible pulses with spatially similar transverse magnetization patterns, but which differ in other properties. Figure 3 illustrates one aspect of this finding by showing magnetization patterns obtained from 2D spiral-based pTx excitation patterns accelerated by R=4 for an 8 channel loop array at 7T. The optimization problem was identically posed, attempting to spatially match a target pattern (flip angle distribution in the shape of the MIT logo) with an additional term in the cost function penalizing the root-mean-squared (RMS) waveform average (proportional to global SAR). While it was expected that the three numerical approaches might obtain different degrees of accuracy, or have different computation burdens, the methods, in fact, produced very similar spatial solutions but with strikingly different global SAR. The SAR reduction amounted to 40% for the Least Squares QR decomposition (LSQR) and Conjugate Gradient Least Squares (CGLS) methods compared to the Singular Value Decomposition (SVD) method even though all of these methods attempted to penalize global SAR in the same way [4]. The fact that the solution space for the flip angle has many similar solutions but with a wide range of different power characteristics suggests that we can pick and chose from nearly equal spatial fidelities in order to improve other aspects of the excitation.

Not for distribution in the US.

4

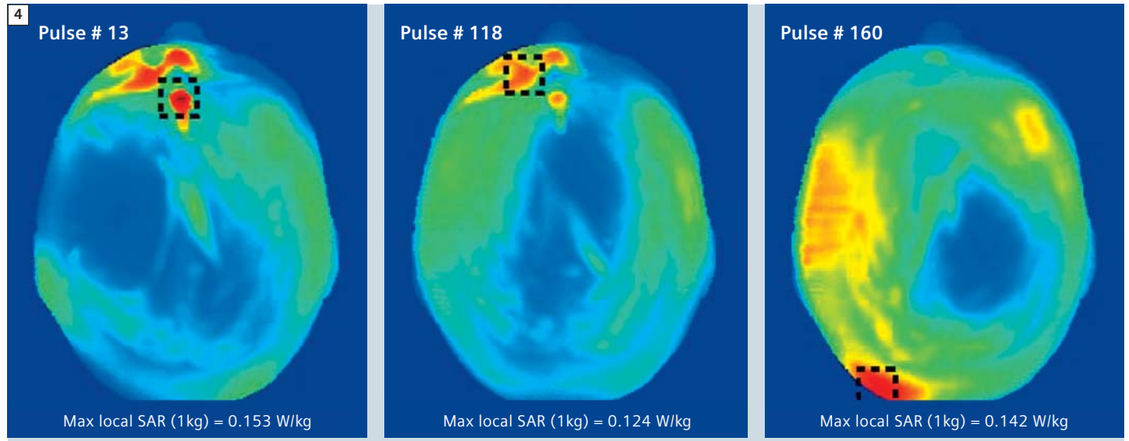

4 Maximum intensity projection of local SAR maps for 3 pulses from a set of 162 designed to produce a uniform flip angle distribution in an axial slice through the head at 7T. Maps are 1g SAR averages obtained from a tissue head model and FDTD simulation of the electric fields of the pulse. Although the pulses achieved nearly identical excitation patterns, the local SAR pattern is very different and would not coherently average with time if the acquisition could cycle through such pulses. *(Figure courtesy of Adam Zelinski.)*

SAR on the run...

A related strategy that expands on this core idea is to generate a family of solutions having similar spatial patterns but differing in the pattern of local SAR. When this set of pulses is used, for example, each pulse for a different imaging slice or even for each phase encode step, the local SAR hotspot will jump around spatially and not coherently time-average into a single long-term hotspot, thus spatially distributing the local SAR load [5-8]. Since the safety concern is local temperature increases which build up over minutes, this spatial-temporal averaging forms a meaningful solution and a viable approach to SAR management in pTx. Even if only two hotspot locations are possible, alternating between the two can lead to a 50% reduction in local SAR. An additional way to potentially force yet different local SAR patterns is to employ slightly different gradient trajectories for each pulse [8]. For example, a slice selective spokes excitation could be generated from any one of hundreds of trajectories. Combing through these solutions produces dozens of candidates within a given spatial fidelity and with different local SAR patterns. An even more sophisticated formalism computes the average SAR pattern from the collection of pulses and optimizes the individual pulses based on this time-averaged pattern [8]. Figure 4 shows the local SAR map for 3 pulses from a set of 162 calculated to mitigate B1+ inhomogeneities in the brain at 7T. The average spatial similarity of the SAR maps for a given pair of pulses was 87%, as computed from the spatial correlation of their SAR maps.

No place to hide...

In addition to forcing the local SAR hotspot to jump around in space, we pursue the regularization of local SAR in the pTx pulse design. Namely, we seek to penalize a potential pulse design during optimization by including its local SAR value into the cost function. The most straightforward way of doing this is to perform an exhaustive search of each pulse's local SAR during the iterative pulse design process. Unfortunately, computing and searching for the local SAR maximum based on the E field maps of an electromagnetic simulation is very computationally demanding, even on a relatively course grid. So while it is desirable to incorporate an exhaustive search over all spatial locations into pTx pulse design, it is currently not computationally feasible. A compromise has been proposed where the pulse is calculated without local SAR in the cost function, note the location of the local SAR hotspot and then redo the design with a penalty for local SAR at that one location [9]. This strategy, however, is likely to simply force the local SAR peak to pop up at a different spatial location. What is needed is a comprehensive regularization which gives the local SAR no place to hide.

Towards this end, Gebhardt and colleagues at Siemens Healthcare and at the University of Erlangen-Nuernberg have noted that the E field data for a coil array is "compressible" in a sense analogous to how a compressed image can provide a nearly faithful image representation at a fraction of the disk space of the original bitmap. Using a fraction of the hundreds of thousands of phase and amplitude representations that would be needed to represent all of the possible excitation combinations of an 8-channel array, the local SAR can be reasonably predicted by a subset of 36 "virtual observation points" [10]. While this subset alone does not promise a fully accurate depiction of local SAR and would not be a replacement for actually checking the local SAR maximum of a pulse, it offers a computational approximation with dramatically reduced computational burden that can be used to penalize local SAR during pulse design while covering nearly all "hiding places." After pulse design, the accurate SAR limits of the pulse would be traditionally calculated. Figure 6 shows the application of the virtual observation compression to regularization of the local SAR [11]. The graph shows the tradeoff between local SAR (y axis) and excitation error compared to the target pattern (x axis) as the relative weight of these two penalties is varied via the regularization parameter. Penalizing the local SAR in this way resulted in a 38% decrease in local SAR for this 8-channel array, spoke design slice-selective pulse for B1+ mitigation in the head at 7T.

5

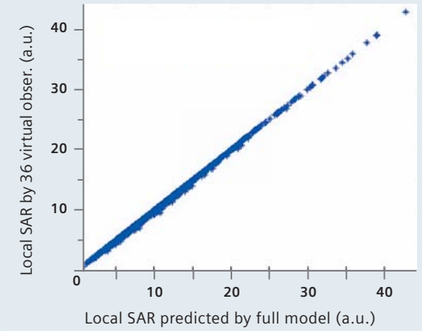

5 Comparison of the local SAR from 1000 randomly chosen transmit combinations evaluated with a full local SAR evaluation (x axis) vs evaluation through 36 virtual observation points (y axis). While the agreement between the two methods is not perfect, the vastly simpler 36 virtual observations reproduce the local SAR with good accuracy. *(Figure courtesy of M. Gebhardt, Siemens Healthcare.)*

6

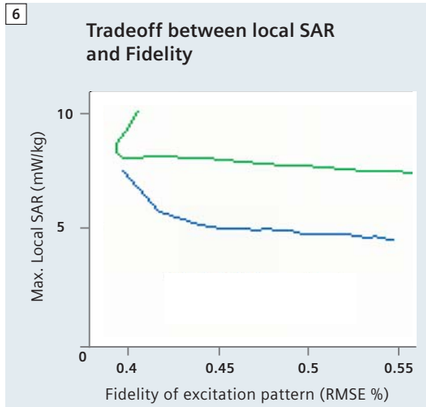

6 Trade-off between excitation error (x axis) and maximum local SAR as the regularization parameter λ is varied. Here the local SAR of the pulse is calculated from a set of 40 virtual observation points. A 38% decrease in local SAR is possible with this method.

Exploiting the choice of excitation coil mode

Since the above discussion centers on exploiting the spatial degrees of freedom in the pulse design process, it is worth considering hardware adaptations which can potentially further extend the number of spatial degrees of freedom. One obvious possibility is to increase the number of transmit channels. Some early exploration of this pathway has suggested significant SAR reduction might be possible with more highly parallel transmit arrays [12]. In this work Lattanzi and colleagues simulated increasing numbers (1, 8, 12, and 20) of circular transmit elements tiling a 30 cm diameter sphere at 7T. They compared the SAR values needed for producing a uniform excitation using RF shimming or a 2D pTx spatially tailored excitation pulse. As seen in practice [2], the pTx pulse was able to achieve a high degree of flip angle uniformity in human head at 7T even with

Not for distribution in the US.

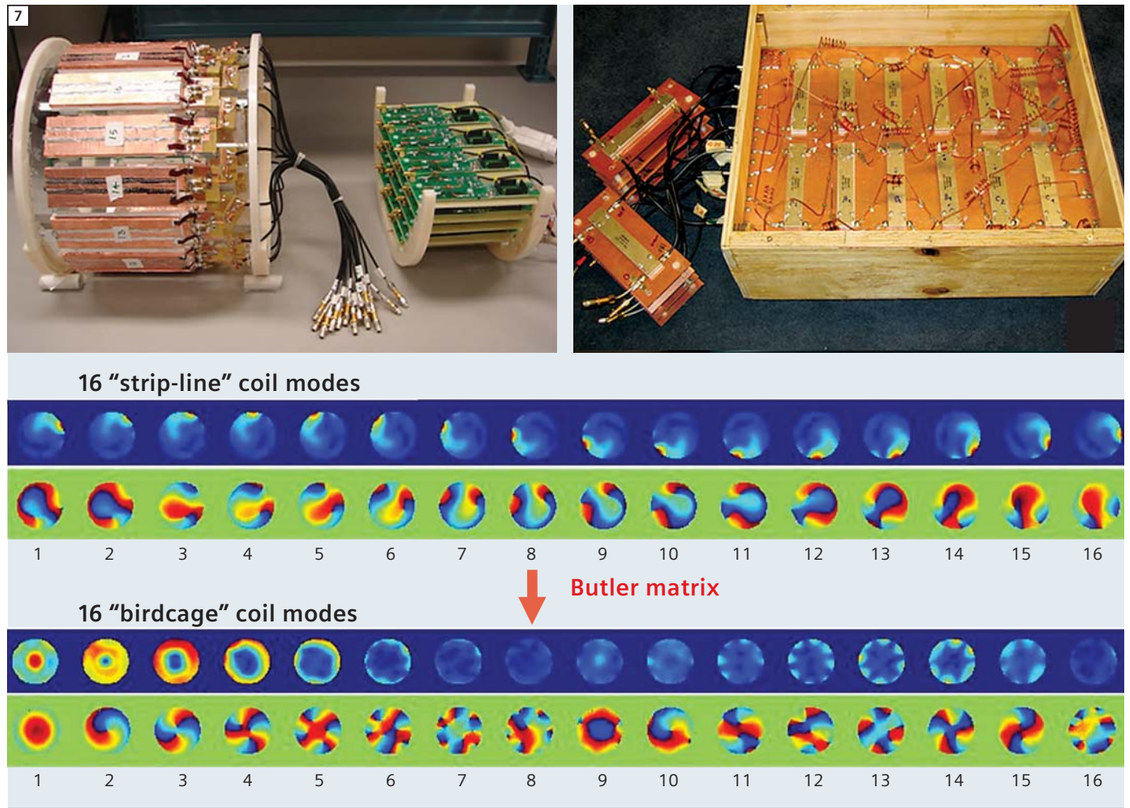

7 A 16-channel 7T strip-line array for the head (upper left) and a 16 x 8 Butler matrix (upper right). Below are the magnitude and phase B1 maps of each of the 16-channels for both the “strip-line” basis set, and the “birdcage” basis set. While excitation ability is roughly equally divided among the strip-line modes, it is concentrated in a few valuable modes in the birdcage basis set. We can choose which 8 modes to drive based on their performance. *(Figure courtesy of Vijay Alagappan, MGH.)*

the 8 coil array, while the RF shimming approach had difficulty even with 20 array elements. Although the additional elements were not needed from a spatial excitation fidelity point of view, they were helpful in reducing global SAR. Global SAR was seen to reduce from 7.9, to 5.5, to 3.3 as the element count increased from 8, to 12, to 20 array elements. Even more interesting, Lattanzi and colleagues calculated the “ultimate intrinsic SAR” consistent with array fields derived from conductor distributions outside the body and satisfying Maxwell’s equations. Constructed in analogy to previous work calculating the ultimate SNR for array distributions, this represents the minimum global SAR possible with a theoretically perfectly optimized array (of however many elements needed). The ultimate intrinsic SAR was an additional 3 fold lower than that obtained with the 20-channel array, suggesting that if additional transmit channels can be engineered in an appropriate and cost effective way, there is potential to utilize element counts well above 20 for reduced SAR in pTx.

By constructing an array with more coil elements than channels to drive them, we can potentially provide the benefit of a higher element count transmit array without actually having to increase the number of RF transmit channels. This is a relatively cost-effective approach since the transmit channels with their power amplifiers and power monitoring equipment are generally more expensive than the array elements themselves. While not increasing the number of transmit elements, this strategy still increases the available degrees of freedom by providing options in how we connect transmit channels to coils. It turns out that these are relatively uninteresting choices for conventional arrays, with transmit elements equally spaced around a cylinder, but it becomes more interesting when the spatial patterns of each array element are not just rotated version of their neighbors. If we think of the spatial distributions of the individual array elements as vectors, then the maximum degrees of freedom derived from this strategy occurs when these vectors are orthogonal. Thus we seek to transform our ‘boring” array of elements around a cylinder into orthogonal modes by finding a suitable linear combination. For loop arrays distributed around a cylinder, an effective linear combination to achieve this goal is the discrete Fourier transform and the resulting basis set is known as the “modes” of the birdcage coil. Similar optimizations in phased array radar have even provided us with a simple hardware realization of this transformation; the Butler matrix [13], which is a generalization of a quadrature hybrid. Figure 7 shows the transformation of the spatial patterns of a 16-element strip-line array into the 16 birdcage modes via the Butler matrix. Since the Butler matrix achieves these modes through simple linear combinations, at first blush it would appear that this “basis set” of excitation patterns would be no better or worse for accelerating spatially tailored excitation than simply driving the strip-line array directly. The superiority of the Butler matrix driven array becomes apparent when only a subset of the array modes is chosen for excitation. The truncation captures a majority of the transmit efficiency and acceleration capabilities in a valuable subset of the channels (and ignoring the less valuable channels). We explored this “array compression” principle by driving a 16-channel strip-line array for 7T head transmit with a 16 x16 Butler matrix connected to the 8-channel transmit system, and demonstrated the theoretically predicted tradeoffs. The excitation configuration that integrates a Butler matrix in this manner allowed us to pick and choose among the modes of a 16-channel array and drive only the best subset of the 16 available modes with our 8 transmit channels. The choice of the optimum 8 birdcage modes compared to 8 strip-line elements allowed a flip-angle inhomogeneity mitigating excitation to achieve a 43% more uniform excitation and 17% lower peak pulse power in a water phantom at 7T [14, 15]. Exploiting these degrees of freedom afforded by choosing among the unequal birdcage modes even further, Zelinski demonstrated that both excitation pattern fidelity and SAR can be improved by choosing the mode set based on the desired excitation pattern [16].

Verifying and monitoring local SAR

As demonstrated in the examples above, the pTx pulse design process has unprecedented ability to impact both global and local SAR. This suggests that global and local SAR need to be carefully checked for each new RF pulse design to insure safety and regulatory compliance. In the most ambitious applications, the pulse design is envisioned to be tailored to the needs of the patient on the table, e.g. providing a volume selective excitation including only the heart, or a curved saturation band following the spine. In this case, in addition to calculating the pulse during the examination, the expected global and local SAR must be checked against regulatory limits. Since the scanner can only monitor total power absorbed by the coil/body, calculations using the pulse shape and modeled E and B fields expected in the body are the only current method available to ensure that local SAR limits are not exceeded before global SAR limits. The scanner can measure the power to each channel, but not the local superposition of E fields in the conductive tissue which gives rise to SAR. This global and local SAR simulation must be performed for every pTx pulse created since a unique spatial-temporal combination of the transmit array elements are used. This is in contrast to conventional single-channel systems where SAR need only be checked once and scaled appropriately based on the transmit power and pulse duration. Therefore, the strategy for ensuring global and local SAR compliance in a parallel transmit system is a generalization of the single transmit case. A full workflow for pTx imaging requires integrated transmit field mapping followed by RF pulse design. The SAR distribution must then be calculated for the pulse based on pre-calculated B_1 and E_1 fields in the appropriate body and coil model. Once the local maximum SAR is found, the local-to-global SAR ratio is examined and the global power limit derated so that the scanner will shut down if the real-time measure of global power to each channel indicates that either the global or local SAR limit exceeded.

An important additional safety check is to monitor in real-time what is actually being transmited by each channel using either field sensing probes or directional couplers on each transmit channel [17]. Then if a single transmit channel fails, the scan can be stopped. This is important since a given transmit channel can create an E_1 field which opposes that of the other channels. In this case, transmit power to that channel reduces local SAR. Alternatively, disruption of a single channel can cause an unpredicted increase in local SAR.

Figure 8 shows the three sections of the workflow tools designed for preliminary pTx studies [18]. The top tool generates the B_1 fields from the data provided by the mapping sequence; a step which ultimately will be performed by the image reconstruction system in an integrated prescan step. The middle panel shows the RF pulse design tool, which at this stage is intended for development use. The

Not for distribution in the US.

8

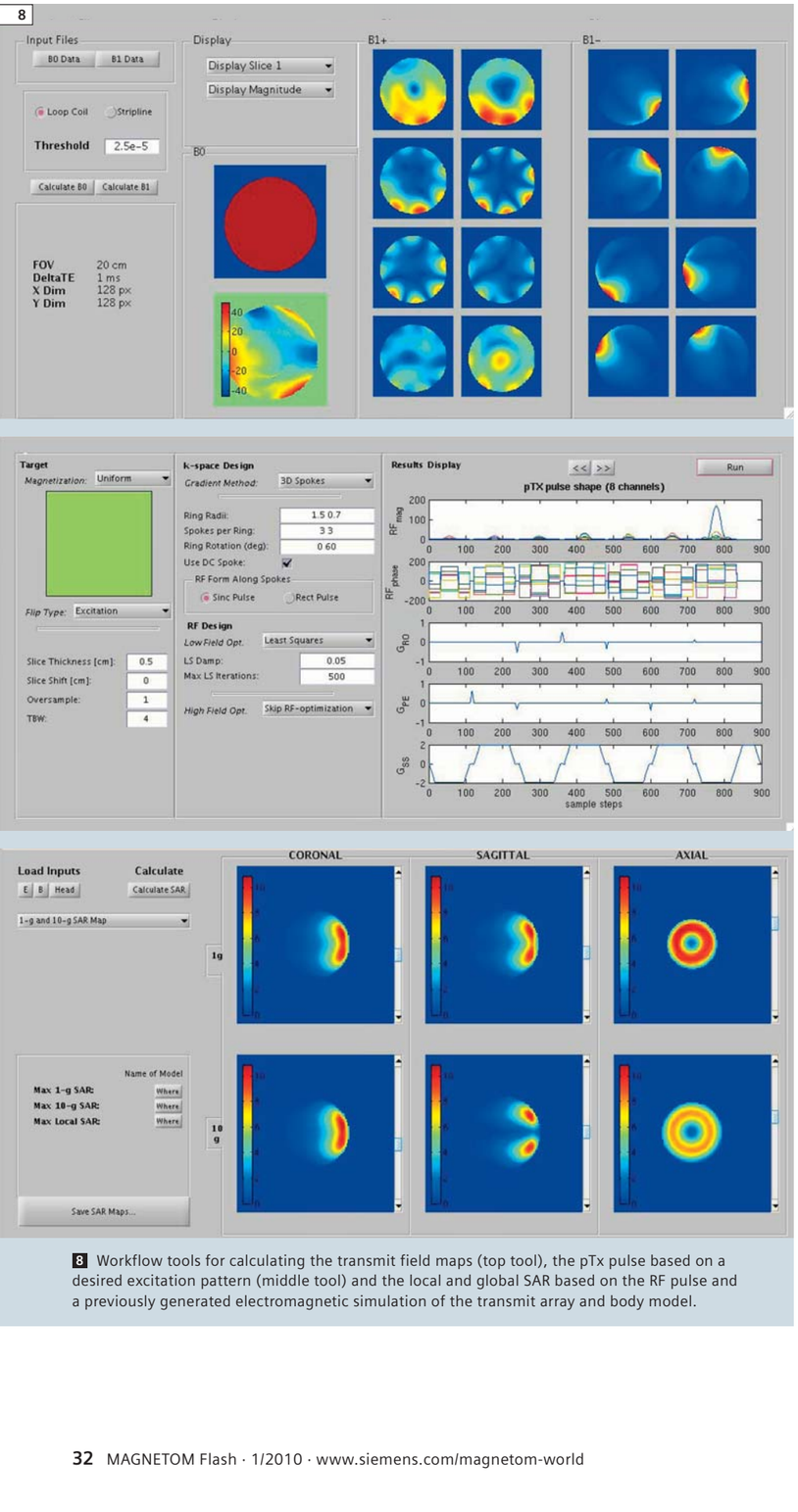

8 Workflow tools for calculating the transmit field maps (top tool), the pTx pulse based on a desired excitation pattern (middle tool) and the local and global SAR based on the RF pulse and a previously generated electromagnetic simulation of the transmit array and body model.

bottom panel shows the SAR maps generated based on the pTx pulse created in the pulse design tool using a previously calculated electromagnetic simulation of the array coil and body model. The SAR-check tool calculates the global power deratings needed in each channel to ensure that both global and local SAR are below safety limits. This information is incorporated into the header of the RF pulse file which is read by the pulse sequence. After checking that the pulse was SAR-checked and that the coil model used matches the coil on the scanner, the pulse sequence transfers the pulse waveforms to the image reconstruction computer where they are compared to the forward and reflected power from the directional couplers on each transmit channel. A disagreement between the measured and expected waveforms on any channel generates a fault which halts the scan.

Conclusions

Theoretical work on parallel RF transmission and recent experimental validations on 8-channel prototype systems at 3T and 7T indicate that parallel excitation has the potential to overcome critical obstacles to robust and routine human scanning at high field strength and enable new applications based on spatially selective excitations. Furthermore, the flexible exploitation of the degrees of freedom in the pulse design problem provides the potential to significantly decrease SAR. While most work has been concentrated on head-sized transmitters, the methods are rapidly translating to body transmit coils at 3T where clinical need is the highest and new generations of scanners offer a system architecture which is pTx-ready. Of course, intriguing research questions remain open in several areas such as the development of rapid and robust RF pulse designs that extend the current low-flip angle domain to arbitrary excitation angle, such as spin echoes, saturation, and inversions pulses. However, with continued development in these areas, progress is likely to accelerate, ultimately supporting fast, subject- and application-tailored RF pulse designs to extend MR excitation from the simple slice-select to the more generally tailored anatomy- or application-specific RF excitation pattern.

Acknowledgements

The authors would like to acknowledge the many researchers, students, and post-docs at Siemens, MGH and MIT whose work is summarized here. We especially acknowledge Kawin Setsompop, Vijay Alagappan, and Adam Zelinski whose thesis work was reviewed here. We also thank Ulrich Fontius and Andreas Potthast for their work setting up the 8-channel 3T and 7T systems and Franz Hebrank and Franz Schmitt for their leadership role in the collaboration and Michael Hamm, Josef Pfeuffer, Axel vom Endt, Mattias Gebhardt and Hans-Peter Fautz for their on-going support.
We acknowledge grant support from the NIH (P41RR14075, R01EB007942, and R01EB006847) and a research agreement and research support from Siemens Healthcare and the Siemens-MIT Alliance.

Contact
Lawrence L. Wald
Associate Professor of Radiology
Athinoula A. Martinos Center for Biomedical Imaging
Department of Radiology
Massachusetts General Hospital
Harvard-MIT Division of Health Sciences and Technology
wald@nmr.mgh.harvard.edu

Elfar Adalsteinsson
Associate Professor
Department of Electrical Engineering and Computer Science
Harvard-MIT Division of Health Sciences and Technology
Massachusetts Institute of Technology
elfar@mit.edu

References

1 Pauly, J., D. Nishimura, and A. Macovski, *A k-space analysis of small-tip angle excitation.* J Magn Reson, 1989. 81: p. 43–56.
2 Setsompop, K., et al., *Slice-selective RF pulses for in vivo B1+ inhomogeneity mitigation at 7 tesla using parallel RF excitation with a 16-element coil.* Magn Reson Med, 2008. 60(6): p. 1422–32.
3 Setsompop, K., et al., *Parallel RF transmission with eight channels at 3 Tesla.* Magn Reson Med, 2006. 56(5): p. 1163–71.
4 Zelinski, A.C., et al., *Comparison of Three Algorithms for Solving Linearized Systems of Parallel Excitation RF Waveform Design Equations: Experiments on an Eight-Channel System at 3 Tesla.* Concepts in Magnetic Resonance Part B (Magnetic Resonance Engineering), 2007. 31B(3): p. 176–190.
5 Adalsteinsson, A., et al., *Method For Reducing Maximum Local Specific Absorption Rate In Magnetic Resonance Imaging,* United States of America Serial No. 12/580076, Filed October 15, 2009.
6 Bornert, P., J. Weller, and I. Graesslin. *SAR Reduction in Parallel Transmission by k-Space Dependent RF Pulse Selection. in Proceedings of the ISMRM.* 2009. Honolulu Hawaii: p. 2600.
7 Graesslin, I., et al. *SAR Hotspot Reduction by Temporal Averaging in Parallel Transmission. in Proceedings of the ISMRM.* 2009: p. 176.
8 Zeliniski, A.C., *Improvements in Magnetic Resonance Imaging Excitation Pulse Design, in Electrical Engineering and Computer Science.* PhD Thesis, 2008, Massachusetts Institute of Technology: Cambridge MA. http://hdl.handle.net/1721.1/45862
9 Graesslin, I. *A Minimum SAR RF Pulse Design Approach for Parallel Tx with Local Hot Spot Suppression and Exact Fidelity Constraint. in Proceedings of the ISMRM.* 2008. Toronto Canada: p. 621.
10 Gebhardt, M., et al. *Evaluation of maximum local SAR for parallel transmission (pTx) pulses based on pre-calculated field data using a selected subset of "Virtual Observation Points". in ISMRM.* 2010.
11 Lee, J., et al. *Parallel Transmit RF Design with Local SAR Constraints. in Proceedings of the ISMRM.* 2010. Stockholm Sweden.
12 Lattanzi, R., et al., *Electrodynamic constraints on homogeneity and radiofrequency power deposition in multiple coil excitations.* Magn Reson Med, 2009. 61(2): p. 315–34.
13 Butler, J. and R. Lowe, *Beamforming matrix simplifies design of electronically scanned antennas.* Electron. Design, 1961. 9: p. 170–173.
14 Alagappan, V., et al. *A Simplified 16-channel Butler Matrix for Parallel Excitation with the Birdcage Modes at 7T. in International Society for Magnetic Resonance in Medicine.* 2008. Toronto, Canada: p. 144.
15 Alagappan, V., et al. *Mode Compression of Transmit and Receive Arrays for Parallel Imaging at 7T. in International Society for Magnetic Resonance in Medicine.* 2008. Toronto, Canada: p. 619.
16 Zelinski, A., et al. *Sparsity-Enforced Coil Array Mode Compression for Parallel Transmission. in International Society for Magnetic Resonance in Medicine.* 2008. Toronto, Canada: p. 1302.
17 Gagoski, B.A., et al. *Real time RF monitoring in a 7T parallel transmit system. in Proceedings of the ISMRM.* 2010. Stockholm Sweden.
18 Makhoul, K., et al. *SAR Monitoring and Pulse Design Workflow in Parallel Transmission at 7 Tesla. in Proceedings of the ISMRM.* 2010. Stockholm Sweden.

Not for distribution in the US.

Time-of-Flight MRA at 7 Tesla

Michael Bock[1]; Armin Nagel[1]; Sebastian Schmitter[1,2]; Sören Johst[1]; Lars Gerigk[3]; Armin Biller[3,4]; Angelika Milker-Zabel[5]; Lydia Schuster[3]; Marco Essig[3]; Heinz-Peter Schlemmer[3]; Wolfhard Semmler[1]

[1]Dept. of Medical Physics in Radiology, German Cancer Research Center (DKFZ), Heidelberg, Germany
[2]Center for Magnetic Resonance Research (CMRR), University of Minnesota, USA
[3]Dept. of Radiology, German Cancer Research Center (DKFZ), Heidelberg, Germany
[4]Dept. of Diagnostic and Interventional Radiology, University Hospital Heidelberg, Germany
[5]Dept. of Radiotherapy, University Hospital Heidelberg, Germany

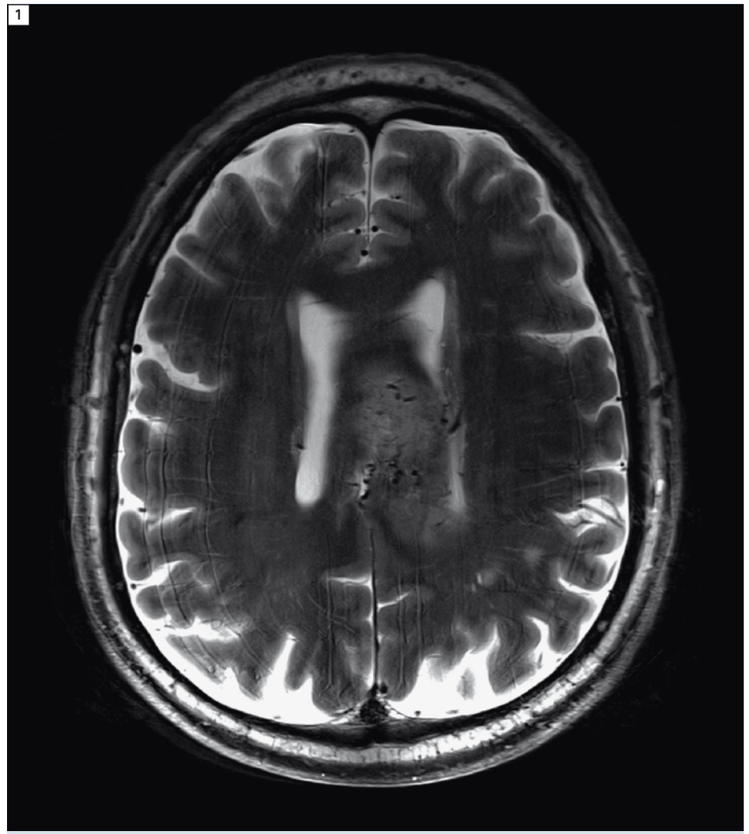

1 T2w TSE image with 300 µm in-plane resolution of a 70-year-old patient with a glioblastoma. The central lesion is visualized with excellent detail, in particular the internal venous vascular network.

Introduction

Over the recent 10 years more than 20 whole-body high field MR systems with field strengths exceeding 4 Tesla have been installed worldwide. The majority of these systems operate at a B_0 of 7 Tesla; however, already four 9.4 Tesla systems are in operation, and an 11.7 Tesla installation in Paris is expected to be finished soon.
The increased signal and the specific new contrasts available at higher magnetic field strengths have been used in various applications. The higher signal strength has been utilized to acquire high-resolution morphologic MR images with 200 µm in-plane voxel size. The enhanced susceptibility difference between oxygenated and de-oxygenated blood, which increases the BOLD contrast nearly linearly with field strength, has been exploited in neuro-functional MRI studies. The prolonged longitudinal relaxation time of blood has been used in arterial spin labeling perfusion studies to visualize the tagged blood for a longer time during the passage through the tissue. Finally, high field MR systems have allowed acquiring spectroscopic data sets with a better spectral differentiation of the individual metabolites.

Time-of-Flight MR Angiography (TOF-MRA)

One particular application that has been shown to profit from higher field strengths is time-of-flight (TOF) MR angiography [5, 16, 10, 7]. In TOF-MRA

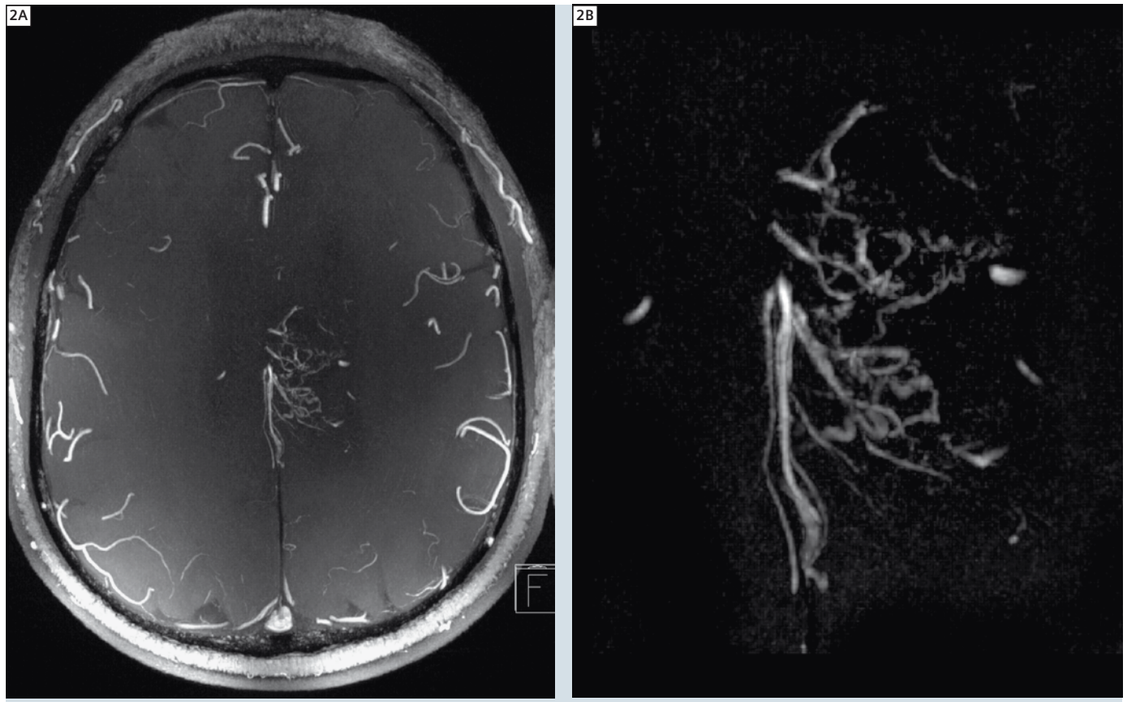

2 Targeted MIP image of a 3D TOF-MRA data set from the same patient as in Fig 1. The irregular tumor-supplying vessels are clearly visualized in the high-resolution MRA data.

use is made of the signal difference between the unsaturated blood flowing into an imaging slab and the partially or fully saturated signal of the static tissue surrounding the blood vessels. The 3D TOF-MRA data sets show the vessels against a dark background, and for data post-processing and visualization typically maximum intensity projections (MIP) are calculated. TOF-MRA is preferably used in the delineation of the arterial intracranial vessels, because the direction of the flow from the arteries in the neck into the skull is clearly defined. Furthermore, in the brain long image acquisition times of 5 to 10 min are possible due to the lack of patient motion.
To acquire the TOF-MRA data sets 3D spoiled gradient echo (FLASH) pulse sequences are applied with flow compensation in all three directions to minimize flow-related signal voids in the vessels. In TOF-MRA not a single thick 3D imaging slab is used as in morphologic 3D imaging, but multiple overlapping thin slabs (MOTSA) are sequentially acquired to reduce the progressive saturation that the blood experiences during its passage through the imaging slab. To further reduce this saturation effect, the flip angle is often increased over the slab (Tilted Optimized Nonsaturating Excitation, TONE) which leads to a nearly constant signal for those blood spins that traverse the slab at a predefined velocity. Furthermore, magnetization transfer contrast (MTC) pulses are applied to selectively saturate the static tissue and thus to increase the vessel-to-background contrast.
Theoretically, TOF-MRA profits twofold from higher field strengths. First, the increased MR signal allows reducing the voxel size so that smaller vessels can be delineated. Unfortunately, the SNR increase is scaling only linearly with field strength, whereas the increase in spatial resolution – if isotropic – reduces the signal by the third power of the linear voxel dimensions (Δx). Thus, to maintain the SNR, with an increase of the field strength by a factor of 2.3 (e.g. from 3T to 7T) Δx can theoretically only be reduced by a factor of $\sqrt[3]{2.3}$=1.3. Fortunately, this argument is only valid if the signal within the voxel is homogeneously distributed – in TOF-MRA, small blood vessels can occupy only a fraction of the voxel volume (partial volume effect), and thus a reduction of Δx does not necessarily reduce the amount of signal-emitting spins from blood. In practice, the linear voxel dimensions are therefore often reduced further than the theoretical limits given above.
A second advantage of higher field

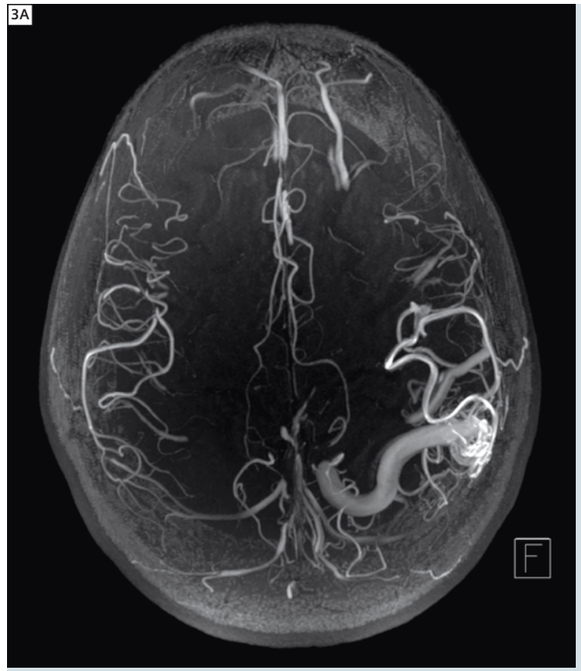

3 Comparison of a 3D TOF-MRA of a 33-year-old AVM patient acquired at 3T and at 7T. In the 3T data the arterial feeders of the AVM appear with a stronger signal, but they are also clearly seen at 7T. Smaller vessels in the AVM nidus are better delineated at 7T demonstrating the complexity of the vascular network. Note that at 7T no venous suppression was applied due to SAR constraints and, thus, the sagittal sinus remains visible.

strengths is the increase of the longitudinal relaxation time T1 with B_0. For the same imaging parameters, longer T1 values lead to a lower FLASH steady state signal of static tissue, and tissue background suppression is becoming more effective. At 3 Tesla, the T1 of white brain matter is 840 ms [17], which increases to 1130 ms at 7 Tesla. For typical TOF-MRA imaging parameters of TR = 15 ms and $\alpha = 20°$ the FLASH signal of white brain matter is then reduced by 22%. At 7 Tesla the background signal constitutes only 18% of the blood signal, so that it often becomes indistinguishable from noise. Note, that this estimate is only valid near the entry of the vessel into the imaging slab where the blood signal has not experienced any RF excitations. The longer the blood remains in the slab the more it gets saturated. Since the blood T1 is also prolonged at higher field strengths this saturation significantly reduces the contrast-to-noise ratio along the path of the blood vessel [3].

Challenges of TOF-MRA at high magnetic fields

The implementation of TOF-MRA protocols at high magnetic fields is challenging due to a number of different problems. At tissue boundaries the static gradients caused by the susceptibility differences have to be compensated by the imaging gradients to avoid local image distortions. In TOF-MRA of the brain this effect is noticeable near the nasal cavities where tissue-air interfaces are present, but it is less pronounced in the brain itself, which has a relatively homogeneous susceptibility.
A more severe limitation is given by the increased energy deposition of the RF system – to achieve the same flip angle as at 3 Tesla the amount of RF energy at 7 Tesla needs to be increased by a factor of $(7/3)^2 = 5.3$. Thus, energy-intensive RF pulses such as MTC pulses cannot be applied due to regulatory constraints (i.e., specific absorption rate or SAR limits). Since background suppression is already very effective at higher fields, the omission of the MTC pulses is no fundamental problem. Another sort of RF pulse, however, is also difficult to integrate due to the SAR limitations: parallel saturation slab pulses, which suppress the signal from venous blood to avoid venous signal overlay in the MIP reconstructions.
Fortunately, there are several options to integrate saturation pulses into TOF-MRA sequences that lead only to a limited increase of the time-averaged SAR. The saturation pulses can be applied less often than the normal excitation pulses – if e.g. the saturation pulse is inserted only after every 10^{th} k-space line, this significantly reduces the total SAR of the pulse sequence. One drawback of this implementation is the reduced saturation efficiency which can lead to non-vanishing signal in veins with a moderate to high blood flow velocity.
Another method to reduce the RF energy of a pulse is given by the variable rate selective excitation (VERSE) technique [2]: here, use is made of the fact that only a certain fraction of the pulse (typically, the so-called main lobe) is contributing most to the SAR of the RF pulse. By selectively reducing the RF amplitude in combination with the gradient amplitude the duration of the RF pulse is only moderately increased, but a substantial reduction in RF power is achieved. In principle, VERSE can be used with every slice-selective RF pulse, and so a SAR reduction can be achieved both for the normal slab-selective excitation pulse as well as for the 90° saturation pulses [6]. VERSE requires a very good synchronization of the gradient activity with the RF pulse modulation, it increases the sound pressure levels [13] and it makes the RF pulse more susceptible to off-resonance effects due to the lower gradient amplitudes [12]. Thus, in practice a compromise between SAR reduction, off-resonance susceptibility and gradient noise needs to be found.

Clinical applications of TOF-MRA at 7 Tesla

In the following two clinical applications of TOF-MRA of the brain are presented, that profit especially from the increased spatial resolution provided by the higher field strength: imaging of tumor blood vessels and of arterio-venous malformations.

Tumor vasculature

The growth of highly malignant brain tumors is facilitated by the ability to induce neoangiogenesis to maintain the supply with nutrients. This is mainly achieved by expression of several growth factors, the most important being vascular endothelial growth factor (VEGF) [8]. Neoangiogenesis leads to a higher microvascular density inside the tumor. Modern therapies target the factor mediated signaling cascade to inhibit neoangiogenesis. One of the most recent agents is Bevacixumab (Avastin), a monoclonal antibody against VEGF [15]. Alternatively, radiotherapy and radiosurgery target the neovasculature of the tumor.
High-grade brain tumors often show a diffuse network of blood vessels, which are less organized [1], more tortuous and of more irregular diameter than normal brain vessels. During tumor growth, the vascular pattern changes from regularly shaped vessels as found in normal tissue to more dilate and higher caliber vessels as well as glomeruloid vessels in glioblastoma [1]. This reorganization leads to a decrease in microvascular density, i.e. the number of vessel cross sections in a given area, but an increase in the mean area occupied by vessels.
As the size of the induced microvessels is usually below the detection limit of MRI at 1.5 or 3T, perfusion MRI markers like relative cerebral blood volume (rCBV) or relative cerebral blood flow (rCBF) have been investigated. Whereas a differentiation of lower and higher grade tumors according to their rCBV and rCBF levels is usually possible in large patient groups, due to the limited reproducibility of perfusion MRI it is difficult to use them for follow-up examinations in clinical routine. In addition, VEGF also increases vascular permeability, leading to an extravasation of contrast agent into the tissue, which is not accounted for in most perfusion models. With conventional MRI at 1.5T or 3T the small 100 µm to 300 µm vasculature is not directly visible due to limitations in both spatial resolution and SNR. At 7 Tesla TOF-MRA can be applied with a spatial resolution of 300 µm and better. In combination with an excellent background suppression of the signal from static tissue this higher resolution is capable of visualizing the neovasculature of malignant brain tumors. In Figure 1, a T2w 7 Tesla image of a 70-year-old patient with an astrocytoma WHO grade IV (glioblastoma) is shown. The lesion is visualized with very good contrast in both T1 and T2-weighted images, and the heterogeneous interior is clearly resolved in susceptibility-weighted images that particularly highlight the venous vasculature [4].
In the TOF-MRA data of the same patient the arterial vasculature is highlighted (Fig. 2), and the highly anomalous vessels are seen - this vascular network can clearly be identified as neo-vasculature because of its irregular shape and surplus vessels not found in normal brain parenchyma. The following imaging parameters were used: TR 15 ms, TE 4.8 ms, flip angle 19°, TONE setting 70%, parallel imaging GRAPPA 2x, bandwidth 165 Hz/pixel, matrix 516 x 704, FOV 14 x 200 mm², 4 slabs, partition thickness 410 µm, TA 4x 2:34 min. At a lower field strength this vessel network could not be visualized. Thus, there is first evidence that therapies targeting neo-angiogenesis might be better assessed with high-resolution TOF-MRA providing comparable results than the different perfusion imaging techniques.

Arteriovenous malformations (AVM)

Arteriovenous malformations are congenital vascular lesions that arise during the embryonic stage from capillary dismorphogenesis. As a consequence, AVMs manifest as one or more arteries that feed a nidus of abnormal vessels instead of the normal capillary bed, and

which are then drained by one or more veins. AVMs are the cause of 1–2% of all strokes, and have a 2–3% risk of hemorrhage [9]. TOF-MRA can provide an overview of the architecture of the AVM, and it helps to identify abnormally dilated feeding and draining vessels. At present, X-ray digital subtraction angiography is still considered the gold standard for AVM imaging due to the higher spatial resolution that allows identifying very small feeding vessels.

With TOF MRA at 7 Tesla the feeding arteries, the nidus and the draining veins are excellently visualized (Fig. 3). Compared to TOF-MRA data acquired at 3T, at first glance no significant difference between the 3T and the 7T data is visible. However, the more detailed visualization of the small sub-millimeter vasculature of the nidus at 7 Tesla becomes apparent. If not operable, AVMs are treated either by embolisation to occlude the feeding arteries, or with radiation therapy to initiate an endothelial reaction which will gradually reduce the free vessel lumen and thus increase the vascular resistance. With the high spatial resolution provided with TOF-MRA, which is delineating the free vessel lumen, the slow lumen reduction of the feeding arteries might be visualized directly, so that treatment-related changes in the angioarchitecture can be identified at an earlier stage.

A quantitative comparison between the 3T and the 7T data is difficult, because different RF coils were used for data acquisition. At 3T, the MAGNETOM Tim Trio system's 32-channel receive-only head coil was used, whereas at 7T a 24-channel transmit receive coil was applied. Due to the intrinsic transmit inhomogeneity at 7 Tesla, a spatially varying contrast is seen in the 7T TOF data, because the flip angle decreases from the center of the coil (where flip angle calibration was performed) to the periphery.

Conclusion

Time-of-flight MRA benefits from the increased SNR and the different contrasts available at higher field strengths. The increase in spatial resolution is particularly beneficial for the assessment of intracranial lesions such as AVMs and high-grade gliomas.

References

1 Bulnes S, Bilbao J, Lafuente JV. *Microvascular adaptive changes in experimental endogenous brain gliomas.* Histol Histopathol 24 (6): 693–706, 2009.

2 Conolly S, Nishimura DG, Macovski A, Glover G. *Variable-rate selective excitation.* J Magn Reson 78:440–458, 1988.

3 Eissa A, Wilman A. *3D TOF MRA of the intracranial arteries: effects of increasing magnetic field to 4.7T.* Proc. Intl. Soc. Mag. Reson. Med. Vol. 14, pp. 1945, 2006.

4 Gerigk L, Nagel A, Biller A, Dinkel J, Schuster L, Hauser T, Puderbach M, Essig M, Delorme S, Bock M. *Assessment of Vascularity in Malignant Glioma: Development of an Imaging Protocol at 7 T.* Proc. Intl. Soc. Mag. Reson. Med. Vol 18, pp. 4424, 2010

5 Heverhagen JT, Duraj J, Schmalbrock P, Thompson MR, Chakeres D, Knopp MV. *Ultrahigh Field (>7T) Time-of-Flight and Phase Contrast Magnetic Resonance Angiography of the Intracerebral Arteries.* Proc. Intl. Soc. Mag. Reson. Med. Vol. 14, pp. 814, 2006.

6 Johst S, Schmitter S, Bock M. *Towards True Arterial Intracranial TOF-MRA at 7T: Protocol Optimization Using VERSE Pulses.* Proc. Intl. Soc. Mag. Reson. Med. Vol 18, pp. 2252, 2010.

7 Kang CK, Hong SM, Han JY, Kim KN, Kim SH, Kim YB, Cho ZH. *Evaluation of MR angiography at 7.0 Tesla MRI using birdcage radio frequency coils with end caps.* Magn Reson Med 60 (2): 330–8, 2008.

8 Kapoor GS, Gocke TA, Chawla S, Whitmore RG, Nabavizadeh A, Krejza J, Lopinto J, Plaum J, Maloney-Wilensky E, Poptani H, Melhem ER, Judy KD, O'Rourke DM. *Magnetic resonance perfusion-weighted imaging defines angiogenic subtypes of oligodendroglioma according to 1p19q and EGFR status.* J Neurooncol 92 (3): 373–86, 2009.

9 Ko H, Johnston S, Young W, Singh V, Klatsky A. *Distinguishing intracerebral hemorrhages caused by arteriovenous malformations.* Cerebrovascular Disease 15: 206–209, 2003.

10 Maderwald S, Ladd SC, Gizewski ER, Kraff O, Theysohn JM, Wicklow K, Moenninghoff C, Wanke I, Ladd ME, Quick HH. *To TOF or not to TOF: strategies for non-contrast-enhanced intracranial MRA at 7 T.* MAGMA 21 (1–2): 159–67, 2008.

11 Narayana A, Kelly P, Golfinos J, Parker E, Johnson G, Knopp E, Zagzag D, Fischer I, Raza S, Medabalmi P, Eagan P, Gruber ML. *Antiangiogenic therapy using bevacizumab in recurrent high-grade glioma: impact on local control and patient survival.* J Neurosurg 110 (1): 173–80, 2009.

12 Schmitter S, Johst S, Bock M, Ugurbil K, van de Moortele PF. *Implementing VERSE for Time of Flight RF pulses at 7Tesla: Methodological Considerations.* Proc. Intl. Soc. Mag. Reson. Med. Vol 18, pp. 4424, 2010.

13 Schmitter S, Mueller M, Semmler W, Bock M. *A VERSE algorithm with additional acoustic noise constraints.* Proc. Intl. Soc. Mag. Reson. Med. Vol 17, pp. 179, 2009.

14 Suzuki M, Matsui O, Kobayashi K, Ueda F, Saitoh C, Katagiri A, Sanada J, Tawara M, Terayama N, Kawashima H, Kida S, Yamashita J. *Contrast-enhanced MRA for investigation of cerebral arteriovenous malformations.* Neuroradiology 45 (4): 231–5, 2003.

15 Verhoeff JJ, van Tellingen O, Claes A, Stalpers LJ, van Linde ME, Richel DJ, Leenders WP, van Furth WR. *Concerns about anti-angiogenic treatment in patients with glioblastoma multiforme.* BMC Cancer 9: 444, 2009.

16 von Morze C, Xu D, Purcell DD, Hess CP, Mukherjee P, Saloner D, Kelley DA, Vigneron DB. *Intracranial time-of-flight MR angiography at 7T with comparison to 3T.* J Magn Reson Imaging 26 (4): 900–4, 2007.

17 Wright PJ, Mougin OE, Totman JJ, Peters AM, Brookes MJ, Coxon R, Morris PE, Clemence M, Francis ST, Bowtell RW, Gowland PA. *Water proton T1 measurements in brain tissue at 7, 3, and 1.5 T using IR-EPI, IR-TSE, and MPRAGE: results and optimization.* MAGMA 21 (1–2): 121–30, 2008.

Contact
Michael Bock, PD Dr. rer. nat. Dipl. Phys.
German Cancer Research Center (DKFZ)
Dept. Medical Physics in Radiology
Im Neuenheimer Feld 280
69120 Heidelberg
Germany
Phone: ++49 6221 42-2528 or -3063
m.bock@dkfz.de

Parallel Transmit Technology for High Field MRI

Lawrence L. Wald[1, 2, 3]; Elfar Adalsteinsson[1, 3, 4]

[1]Athinoula A. Martinos Center for Biomedical Imaging, Department of Radiology, Massachusetts General Hospital, Boston, MA, USA
[2]Harvard Medical School, Boston, MA, USA
[3]Harvard-MIT Division of Health Sciences and Technology, Boston, MA, USA
[4]Department of Electrical Engineering and Computer Science, Massachusetts Institute of Technology, Boston, MA, USA

Introduction

The success of parallel reconstruction methods and their impact on image encoding has sparked a great deal of interest in using the spatial distribution of transmit coils in an analogous fashion. Namely, by breaking down the transmit field into multiple regions each controlled by a separate transmit channel, spatial degrees of freedom are created that allow the spatial information in the array to be exploited in the excitation process. While a homogeneous birdcage-type body-coil driven by a single RF pulse waveform has served the MR community well, it does not possess spatial degrees of freedom, and subsequently works best for uniform excitations. Parallel excitation arrays and the potential to utilize the spatial information in an array during RF transmission offer the possibility to move beyond the uniform slice-select excitation, and to generate spatially tailored RF pulses; excitation pulses with a carefully controlled spatially varying flip angle or excitation phase that can mitigate artifacts or isolate specific anatomy.

While the concept of spatially tailored excitation pulses has been known for some time, the implementation of such pulses is largely impractical on conventional single-channel excitation systems, and only by introducing the additional spatial degrees of freedom in a transmit array do they achieve practical durations for clinical imaging. An early application of spatially tailored parallel excitation was to mitigate the non-uniform flip angle problem created by RF wavelength effects at high field (Fig. 1). These non-uniformities arise when the wavelength of the RF approaches the dimension of the human head or body and create destructive excitation field interference among sections of a conventional transmit coil. This is most noticeable in the head at 7T where a strong center brightening is a typical feature (perhaps more properly termed peripheral darkening) and in the body at 3T where shading is seen near large regions of non-fatty tissue in the abdomen. Unlike detection inhomogeniety that manifests primarily as image intensity shading, a non-uniform transmit B_1 field results in spatially dependent tissue contrast and therefore reduced diagnostic power, which cannot be recovered with an image normalization scheme. A spatially tailored excitation mitigates this problem by anticipating the flip angle inhomogeniety and compensating for it in the spatial profile of the excitation. Once the technology is in place for spatially tailored RF excitations, the ability to generalize excitation profiles beyond the slice-select pulse offers many exciting opportunities for selective excitations of anatomically tailored volumes. An anatomy-specific excitation could potentially reduce image encoding needs (e.g. for cardiac or shoulder imaging) by reducing the effective field-of-view, it could enable more accurate CSI exams in tissues with many interfaces like in the prostate, and allow selective spin-tagging excitations (potentially allowing vessel territory perfusion imaging), or simply provide clinically useful but non-traditional excitations such as curved saturation bands for the spine or brain.

In this article we review some of the progress which has been made with a prototype 8-channel parallel transmit system integrated into a Siemens MAGNETOM Trio, A Tim System, and a 7 Tesla MAGNETOM system. We discuss some of the recent advances in calculating parallel transmit RF pulses for spatially tailored excitation and show examples of B_1 transmit mitigation at 3T and 7T. Further, we describe some of the recent advances in methodology as well as some of the outstanding issues that must be overcome for routine application.

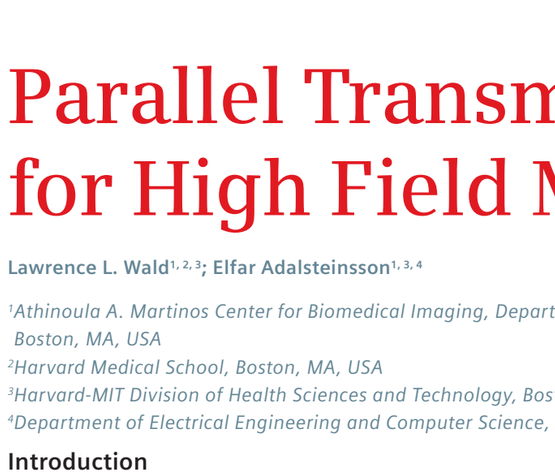

1 Flip angle inhomogeneity resulting from wavelength effects in the brain at 7T (central brightening) and liver at 3T (drop-out). Spatial variations in the transmit efficiency, and therefore the flip angle, are more problematic than the receive inhomogeneities since they lead not only to image shading, but more importantly, image contrast alterations.

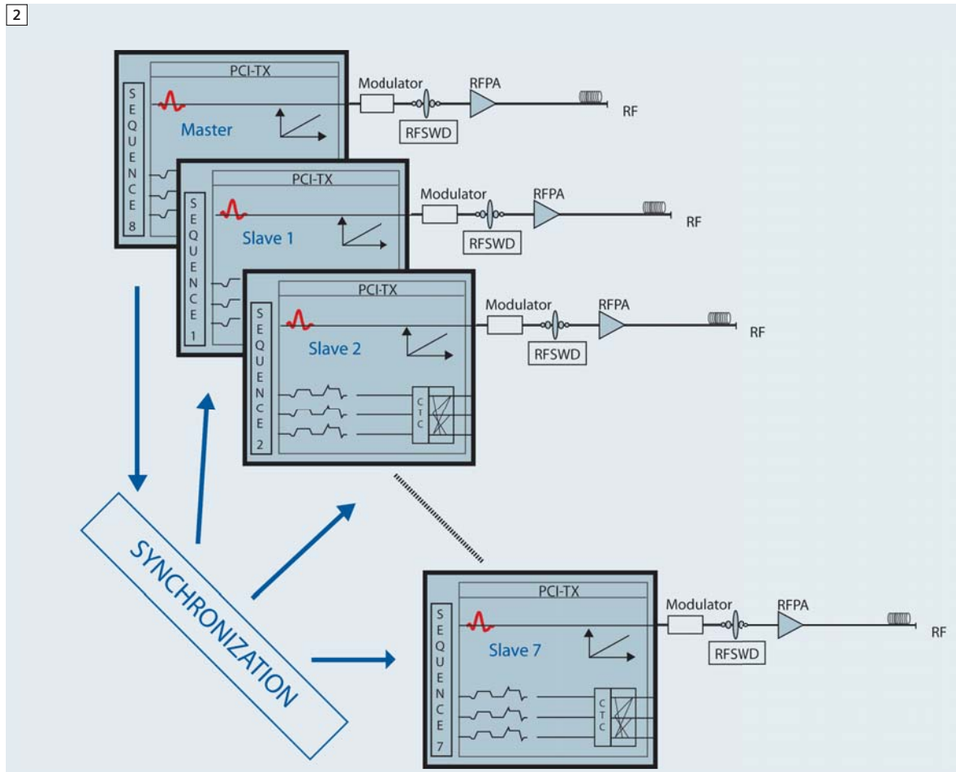

2 System schematic of the 8-channel transmit system. *(Figure courtesy of U. Fontius, Siemens Healthcare.)*

Experimental Setup

Flexible delivery of independent RF waveforms to each channel of the array is needed to realize the full potential of parallel transmission. Additionally, fast gradient trajectories are required during the RF pulses to modulate the spatial profile of the excitation. Since eddy current compensation is performed during the RF waveform generation using knowledge of the gradient history, each RF channel

needs to be fully integrated into the full waveform generation system of the scanner. To achieve this, a prototype 8-channel transmit system was set up in a master-slave configuration with each channel capable of running an independent pulse sequence, and importantly, independent B_0 eddy current compensation. Finally each channel utilized a separate RF power amplifier (8 kW each in the 3T case and 1 kW each in the 7T case) and fully independent SAR monitoring on each channel.

Which RF transmit array configurations capture the maximum ability to capitalize on the parallel nature of the excitation? This question is central to the optimal design of a flexible parallel excitation system and remains an open research problem. Two principles guide our design of the array configuration:

- obtaining the maximum benefit from the limited (expensive) number of excitation channels, and
- retaining the simplicity of birdcage-like excitation in one channel.

These two goals are elegantly achieved when a so-called "Butler matrix" [1] is inserted in the path from the RF amplifiers to the coil elements to drive a ring of excitation coils on a cylindrical former. In contrast to a direct drive of the coil elements by the RF amplifiers, the Butler matrix transforms the phase relationship of the array elements so that each RF excitation channel drives not just a single RF element but influences all of them in a specific (and familiar) relationship; namely the spatially orthogonal modes of a birdcage coil. The spatial patterns of these modes and the phase relationships needed to generate them are well known from birdcage theory [2], and when achieved, have several benefits. Firstly, it allows the "master" channel of the array to operate as a uniform birdcage-like excitation coil. Although at high field the so-called uniform birdcage mode generates significant field variation (one of the original motivations for parallel TX technology), it is useful in practice to have one of the channels operate from this well established and efficient starting point. The other channels then span progressively higher-order modes of the birdcage coils with their spatially specific amplitude and phase variations.

3

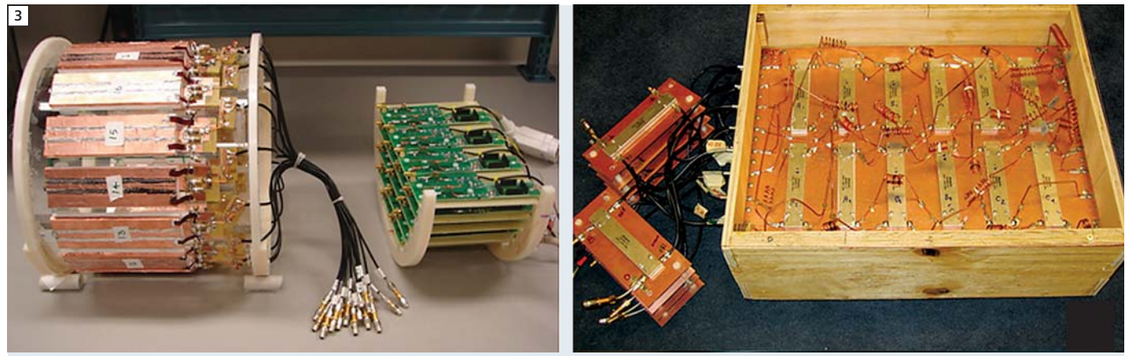

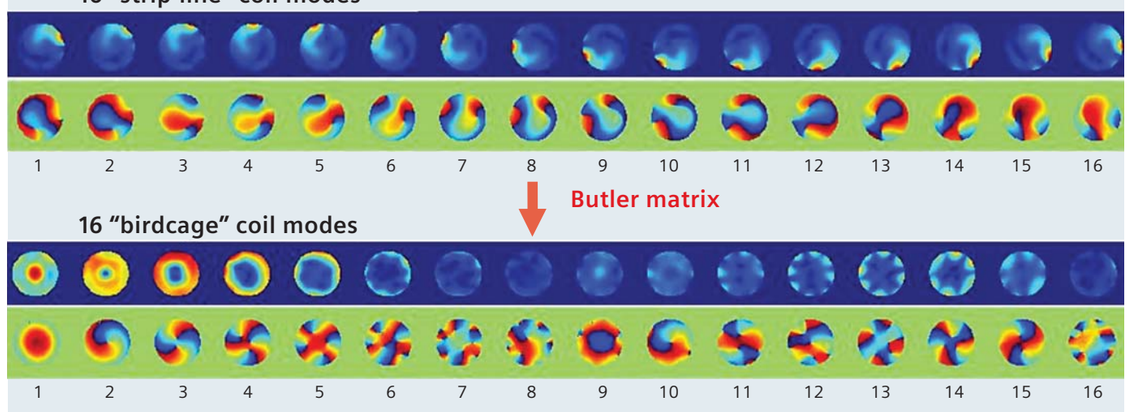

3 A 16-channel 7T strip-line array for the head (upper left) and a 16 x 8 Butler matrix (upper right). Below are the magnitude and phase B_1 maps of each of the 16-channels for both the "strip-line" basis set, and the "birdcage" basis set. While excitation ability is roughly equally divided among the strip-line modes, it is concentrated in a few valuable modes in the birdcage basis set. We can choose which 8 modes to drive based on their performance. *(Figure courtesy of Vijay Alagappan, MGH.)*

Since the Butler matrix achieves these modes through simple linear combinations, at first blush it would appear that this "basis set" of excitation patterns would be no better or worse for accelerating spatially tailored excitation than simply driving the array of elements one at a time. The superiority of the Butler matrix driven array becomes apparent when only a subset of the array modes is chosen for excitation. In practice this allows the benefit of a larger array to be captured in a system with fewer transmit channels (i.e. lower cost) by capturing a majority of the transmit efficiency and acceleration capabilities in a valuable subset of the channels (and ignoring the less valuable channels). We explored this "array compression" principle by driving a 16-channel stripline array for 7T head transmit with a 16 x 16 Butler matrix connected to the 8-channel transmit system [3], and demonstrated the theoretically predicted tradeoffs. The excitation configuration that integrates a Butler matrix in this manner allowed us to pick and chose among the modes of a 16-channel array and drive only the best subset of the 16 available modes with our 8 transmit channels. The choice of the optimum 8 birdcage modes compared to 8 strip-line elements allowed a flip-angle inhomogeneity mitigating excitation to achieve a 43% more uniform excitation and 17% lower peak pulse power in a water phantom at 7T [3].

4

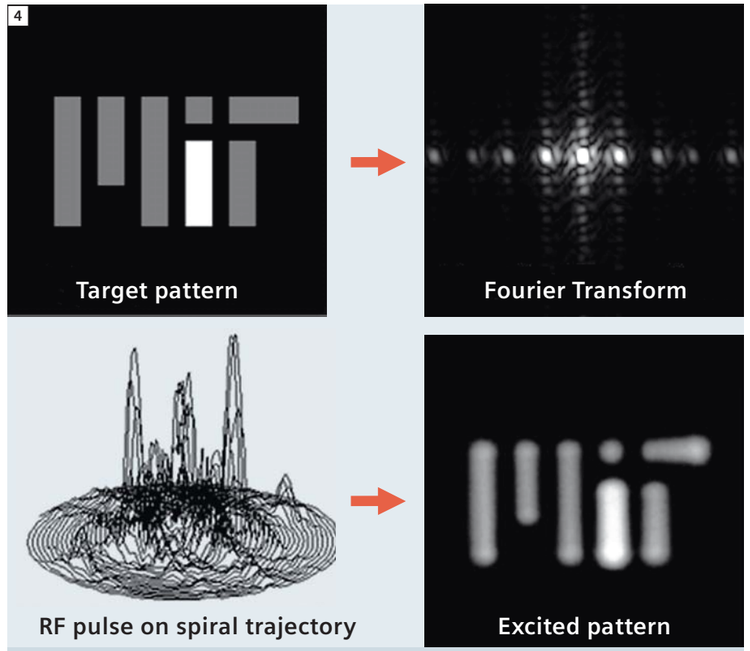

4 RF pulse design for a 2D spatially tailored excitation. Use of parallel transmit allows the spiral gradient trajectory to be accelerated. In this case a 4 x acceleration of the spiral trajectory allowed the excitation pattern to be achieved with a 2.4 ms duration RF pulse. *(Figure courtesy of Kawin Setsompop, MGH, MIT.)*

Spatially tailored RF excitation

RF excitations appropriately modulated in amplitude and phase during time-varying gradients offer the potential of spatially tailored RF phase and amplitude in the excitation [4]. Although such pulses have been demonstrated for many years, the lengthy encoding period needed duration of these pulses (as long as 50 ms) has precluded their routine use. Parallel transmission addresses this limitation by accelerating the excitation encoding gradient trajectory analogously to how parallel receive provides unaliased images with an accelerated encoding trajectory [5, 6]. A practical goal is to achieve 3D excitation pulses in less than 5 ms with a spatial profile that can mitigate the observed B_1 pattern in the head or body. This short duration is needed to be useful in common anatomical imaging sequences such as TSE, MPRAGE and FLASH.

Shaping the 2D spatial flip-angle distribution of an RF excitation requires modulated RF amplitude and phase while the gradients trace an excitation k-space trajectory, typically a spiral or echo-planar path. In practice, we first choose a target magnetization map, which is proportional to the flip angle map for small flip angles. For example, the target magnetization map might be a uniform flip-angle distribution or a selected region around the anatomy of interest (for zoomed imaging). The calculation of the corresponding RF waveform is greatly simplified in the low flip angle case where it can be reduced to a k-space or Fourier analysis [4]. The RF excitation during such a gradient traversal is viewed as a series of short, small flip angle excitations. The phase and amplitude of these small RF pulses is altered so that the deposition of RF energy in the "excitation k-space" matrix is the Fourier transform of the desired spatial flip-angle map. In parallel transmit, the pulse duration is significantly reduced since an accelerated, under-sampled excitation k-space trajectory is used. The missing information is provided by incorporation of the spatial profiles of the multiple transmit array elements in the design process so that an unaliased excitation pattern is achieved.

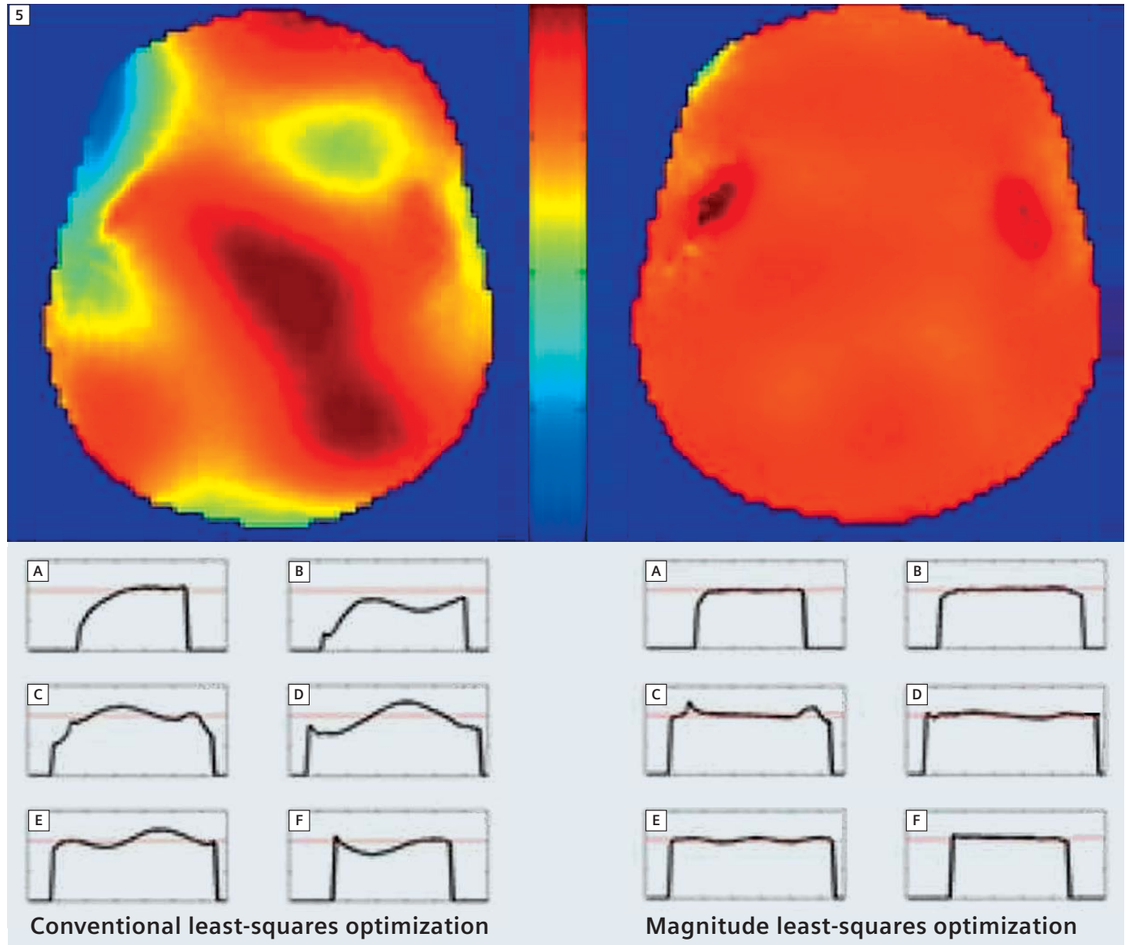

5 Measured flip-angle profiles for a 2.4 ms duration, flip-angle mitigating pulse (uniform target profile) for 7T demonstrated in a head-shaped water phantom. The MLS optimization achieves nearly 4 fold lower error compared to the conventional least-squares optimization. *(Figure courtesy of Kawin Setsompop, MGH, MIT.)*

Regularization of Specific Absorption Rate (SAR) and relaxation of phase constraints

A critical observation about the parallel transmit pulse design problem is that there are many different solutions for the RF pulses that achieve a very similar fidelity to the target excitation pattern. Knowing this, it is beneficial to choose a solution which produces a "close enough" pattern but minimizes SAR. This can be achieved by explicitly penalizing pulse amplitude when solving for the optimal pulse shapes, thus resulting in a significantly lower global SAR with little loss of excitation pattern fidelity [7].
Another important observation that yields significant payoff in the RF design is that the vast majority of MR applications ignore the phase in the final image (only magnitude images are viewed). In this case, the excitation can tolerate a slow phase roll across the FOV with no impact on the final image. We have capitalized on the relaxation of the phase restraint by developing a "Magnitude Least Squares" (MLS) algorithm for solving the parallel transmit pulse design optimization [8]. In this scheme, the algorithm attempts to achieve the target excitation pattern in magnitude, but allows slow phase variations across the FOV. The relaxed constraint allows a higher fidelity in the magnitude pattern or a lower pulse power (i.e. low global SAR). Figure 5 compares the MLS result for a slice-selective excitation with uniform target flip-angle distribution to the conventional Least Squares optimization. A two-fold improvement in target magnitude fidelity was achieved with similar SAR. Conversely, the same target fidelity could be achieved with a ~2 fold reduction in SAR.

3D shaped excitations

Extending accelerated spatially tailored pulses to general 3D shapes requires covering k-space in 3 directions and is consequently very time consuming. Nonetheless, full 3D excitation is required for many applications, including adding in-plane flip-angle modulation to the traditional slice-selective excitation. We explored the capabilities for these 3D shaped excitations by using a variant of the echo-volume or "spokes" trajectory. This design class of RF excitation pulses can be viewed as multiple slice-selective RF pulses in z that are played out with different amplitude and phase modulations for each (k_x, k_y)-location, providing a conventional slice-selection in z, but with spatial modulations in the image plane, (x, y). Since the conventional axial slice select gradient can be viewed as a line segment in excitation k-space along k_z, multiple such lines look like a collection of spokes orthogonal to (k_x, k_y) when viewed in k-space. The parallel transmit problem then reduces to determining the number and (k_x, k_y) location of such spokes, as well as the calculation of the phase and amplitude of each transmit channel for each spoke to achieve the desired modulation in the x, y plane.
The excitation trajectory design problem is guided by our knowledge of the desired target excitation pattern and B_1 profiles of the transmit array elements, and further augmented by a SAR penalty term in the optimization cost-function. Thus, the k-space trajectory and RF pulse can be jointly optimized to produce a higher fidelity excitation pattern while satisfying constraints on overall SAR. When a mode-mixing strategy is employed in the transmit array, we can additionally choose which modes to connect to the transmit channels based on the excitation trajectory. Since the excitation k-space amplitudes and phases are related to the target pattern by the Fourier transform (for low flip-angle excitations), the k-space trajectory can be limited to regions with the largest magnitude Fourier coefficients. However, this does not take advantage of the "don't care" regions outside the body but within the FOV. A better strategy is to let a sparsity-enforcing algorithm choose the trajectory from among a discrete set of k-space grid points allowing an explicit trade-off between excitation fidelity and pulse length [9]. The simulation in Figure 6 demonstrates the advantage of choosing a subset of circular trajectories

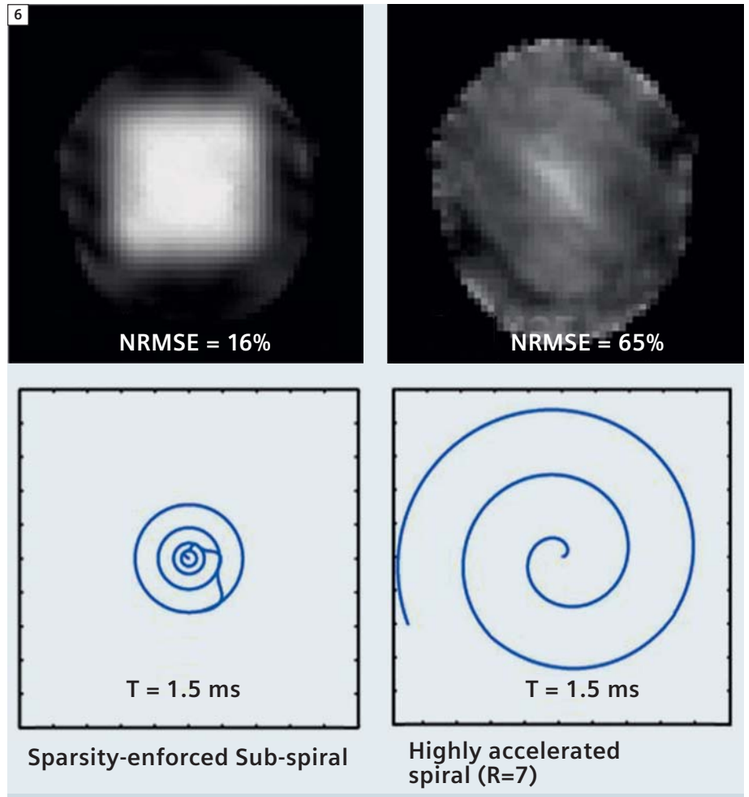

6 Target excitation (box) implemented with a sparsity-enforced choice among a set of concentric circular trajectories and a highly accelerated (R=7) spiral of the same duration. *(Figure courtesy of A. Zelinski, MIT.)*

among a candidate set of circles in the k_x, k_y plane compared to a highly accelerated spiral excitation of the same overall duration. Figure 7 shows a similar optimization from among a grid of possible locations in the k_x, k_y plane of the "spokes" trajectory. The target excitation is slab-selective in z, and selectively excites the two simulated arteries in-plane, such as might be used for a vessel-selective arterial spin labeling experiment. In this case the two crossing vessels are tagged with excitations differing in RF excitation phase by 90°, demonstrating tight RF control in both magnitude and phase for a challenging 3D excitation target.

B_1 mitigation at 7T

Parallel excitations were performed on both head-shape water phantom and in vivo human studies at 7T [10]. Both slice-selective B_1 mitigated excitation and arbitrarily shaped volume excitations were created and validated via a 16-element degenerate strip-line array coil driven with a Butler matrix utilizing the 8 most favorable birdcage modes. RF and gradient excitation waveforms were designed using the MLS optimization, and a spokes' placement optimization algorithm. With this design method, optimized parallel excitation waveforms for human B_1 mitigation were only ~50% longer than conventional single-channel slice-selective excitation while significantly improving flip-angle homogeneity. We compared the B_1 mitigation performance by parallel transmission to "RF shimming," which can be viewed as a simplified form of parallel transmit where the array elements are driven with individual amplitudes and phase shifts but not separate pulse shapes. For the slice-selective excitation, the RF shimming can be viewed as a special case of the "spokes" trajectory where only a single spoke (at the center of (k_x, k_y)-space) is employed. Thus, RF shimming utilizes the spatial patterns of the transmit array, but not the encoding ability of the gradient trajectory. Figure 8 shows the measured B_1 map for the "uniform" birdcage excitation, the RF shimming and pTX with spokes trajectory (all slice selective excitations). The full pTX method clearly demonstrates superior B_1 mitigation performance. The phantom inhomogeniety is similar in shape to that of the head, but exhibits more severe field variations than in the human head; a 3 fold variation in flip angle across the slice. Nevertheless, the

7

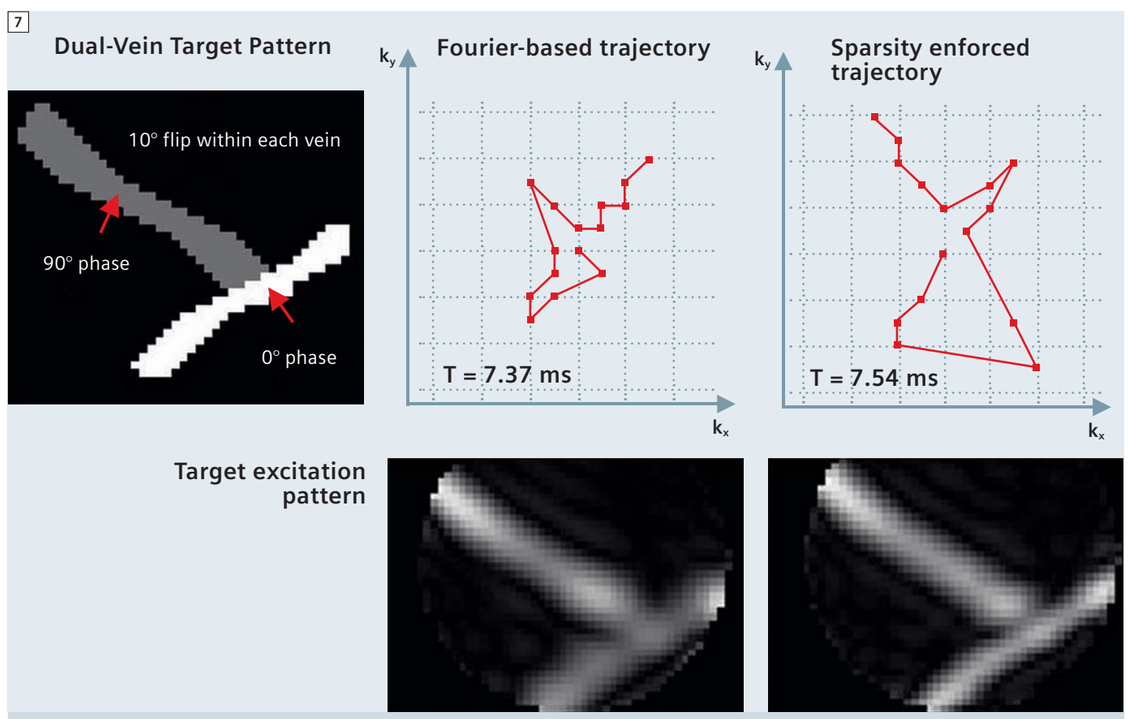

7 Sparsity enforced trajectory generation for a 3D arterial tagging senerio. Slab-selective excitation is performed by 15 "spokes" in the kz direction (each with a weighted excitation amplitude) to create the desired in-plane pattern. The Fourier method utilizes the locations where the transform of the target pattern has highest energy. The sparsity enforced algorithm chooses from a grid of locations and maximizes an L1 norm. *(Figure courtesy of A. Zelinski, MIT.)*

B_1 maps in a head shaped water phantom at 7T.

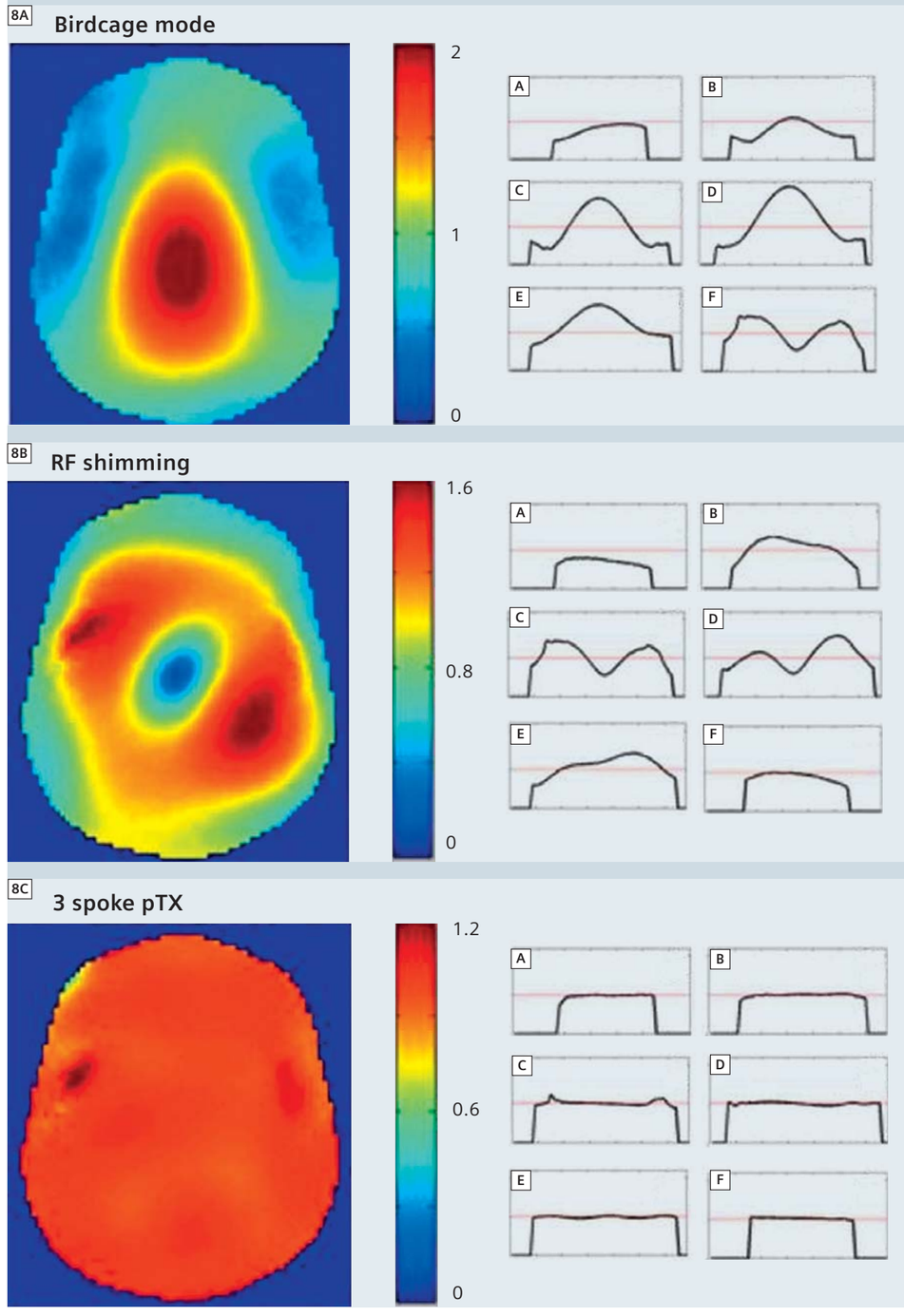

8 Comparison of B_1 inhomogeniety mitigation in slice-selective excitations at 7T (head-shaped phantom) using **A:** conventional birdcage excitation (SD of B_1 across head = 42% of mean), **B:** RF shimming (identification of optimal amplitude and phase excitation settings) with 8-channel transmit array (SD = 29% of mean) and **C:** parallel TX with 3-spoke trajectory (2.4 ms duration) (SD = 5% of mean). *(Figure courtesy of K. Setsompop MGH, MIT.)*

9A

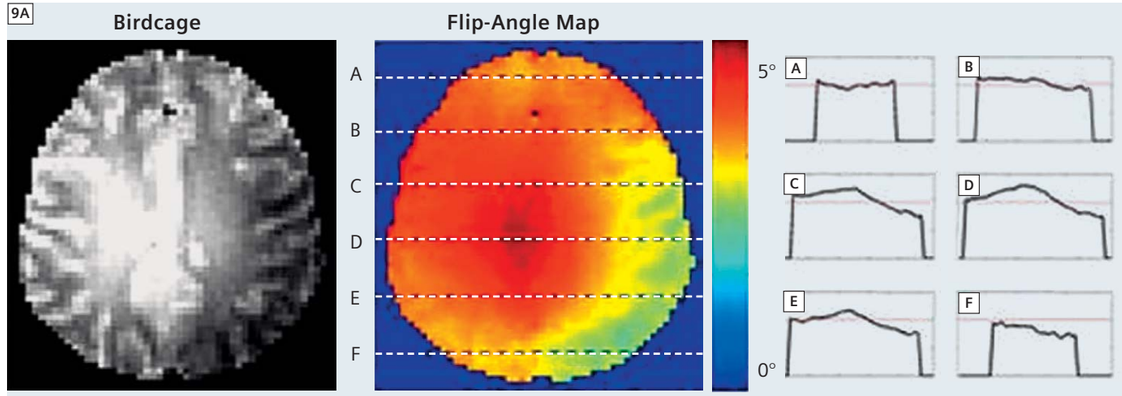

9B

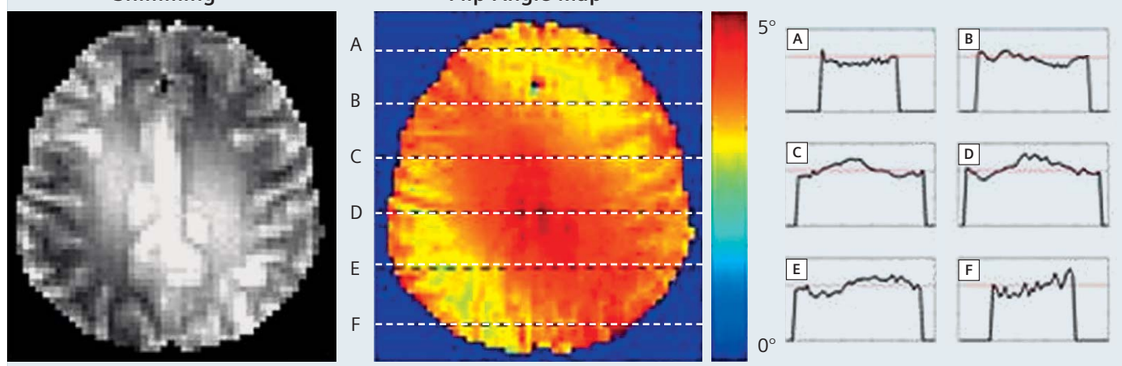

9C

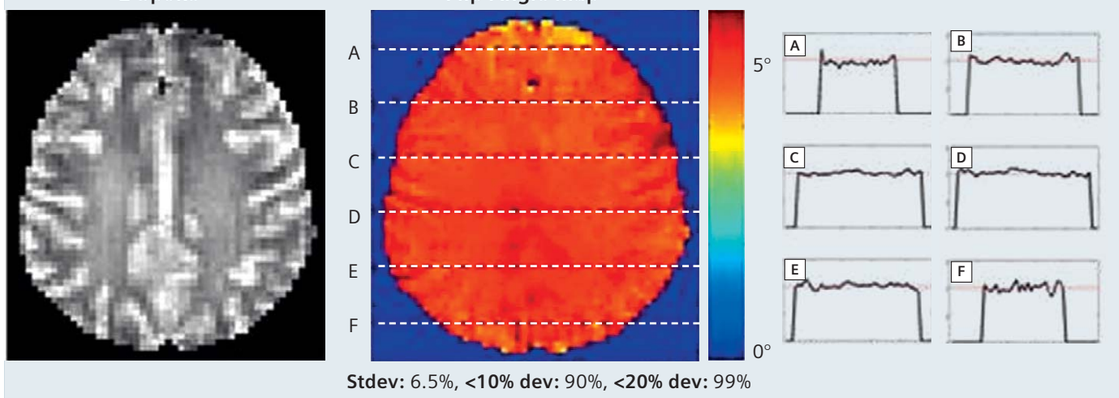

9 Flip-angle inhomogeniety at 7T in the human head using 3 methods (conventional birdcage excitation, RF shimming and pTX with spokes trajectory.) Subject #5 (who displayed the most severe inhomogeniety) is shown. Gray scale images show a proton density-weighted low flip-angle image with the receive profile divided (leaving only variations due to transmit.) Color scale image is a quantitative flip angle map acquired with each of the 3 methods. *(Figure courtesy of K. Setsompop MGH, MIT.)*

10

3T flip angle maps in abdomen

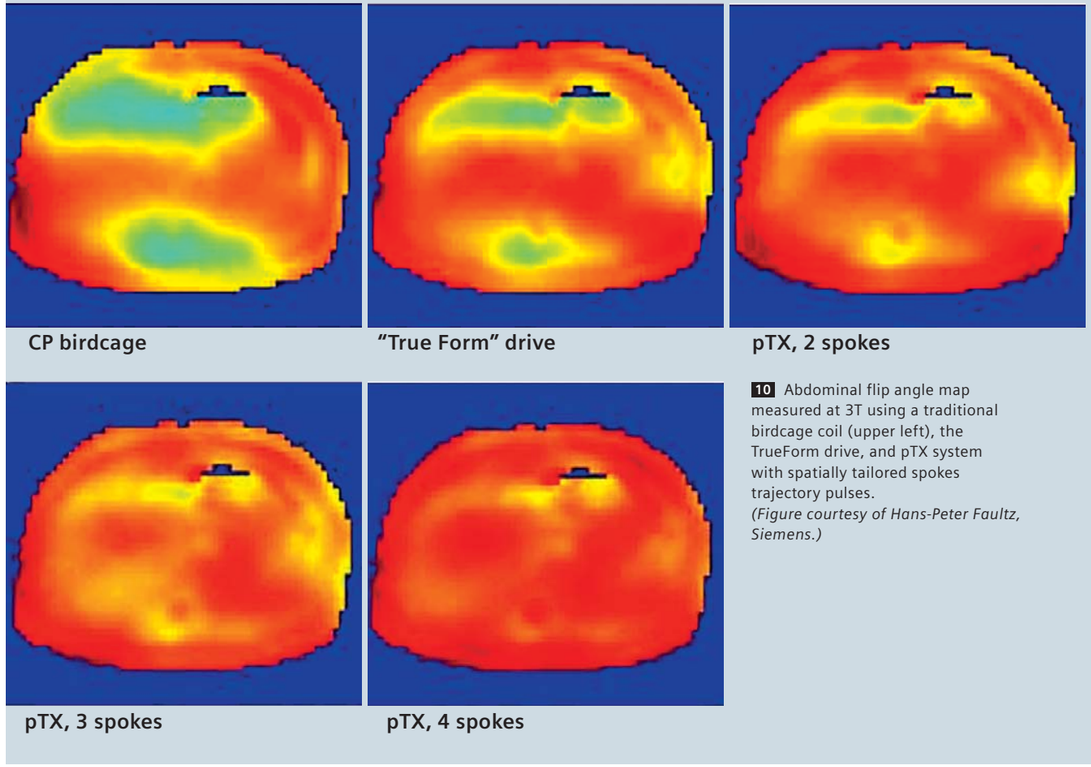

10 Abdominal flip angle map measured at 3T using a traditional birdcage coil (upper left), the TrueForm drive, and pTX system with spatially tailored spokes trajectory pulses. *(Figure courtesy of Hans-Peter Faultz, Siemens.)*

3-spoke trajectory and 8-channel array is sufficient to remove the vast majority of the inhomogeneity.

Figure 9 shows B_1 maps obtained from one of 6 healthy subjects (studied with institutional approval and informed consent). In this case a 2.3 ms duration 2-spoke slice-selective trajectory was used with the 8-channel system and the MLS design method. The birdcage and RF shimming acquisition used a 1.4 ms sinc-like excitation. While some contamination from anatomy is seen in the B_1 transmit maps, the pTX method significantly reduced the B_1 inhomogeneity (standard deviation (Stdev.) across slice was 8% of the mean compared to 21% for the birdcage excitation and 14% for the RF shim).

Figure 10 shows the parallel transmit method applied to a similar flip-angle inhomogeneity problem; the abdomen at 3T. Here a similar wave-cancelation occurs in body imaging where the size of the body becomes comparable to the wavelength of the RF. The conventional circularly polarized birdcage can be significantly improved upon by optimizing the phase relationship between the drive ports of the coil to produce a more uniform and efficient elliptical polarization tailored to the body. Further gains in uniformity were realized with parallel transmit and the 3D spokes spatially tailored excitation pulses calculated based on knowledge of the B_1 field profiles of the transmit array elements.

SAR considerations

While the results in Figure 8 demonstrate the ability of the parallel transmit method to mitigate the inhomogeneous flip-angle distribution at high field, the spokes pulses used more RF energy to achieve the desired flip angle than the simple birdcage transmit (but less than the RF shim). The total pulse energy for the birdcage, RF shim, and pTX-spokes methods were 10.7 mJ, 24.8 mJ, and 21.8 mJ respectively. This suggests that the parallel methods achieve uniformity only with some degree of self-cancellation among the fields or excited magnetization. A similar effect is seen in the 2D spiral trajectories, where pulse energy significantly increases with acceleration,

even with an explicit B_1 amplitude penalty in the pulse design cost-function and local SAR levels are difficult to predict [11]. An example is shown in Figure 11 where the local SAR is calculated for a series of box-shaped excitations placed at 5 different positions in the head (left to right). The spatially tailored 2D pulses used an 8-channel array and spiral trajectories with accelerations ranging from R=1 to R=8. The pulse design maintained a constant fidelity to the target pattern by trading off the pulse amplitude constraint and the fidelity constraint. The local SAR was calculated from the E_1 fields in a multi-tissue head model for the array and pulse. The first observation based on these results is the enormous cost in local SAR incurred by keeping the fidelity constant in the face of increasing parallel transmit acceleration (nearly 3 orders of magnitude variation in local SAR!). The second observation is that local SAR varies significantly with the position of the excitation box. For low accelerations the central box positions have the lowest SAR, while the higher accelerations, the peripheral positions have lower SAR.

For evaluation and monitoring of SAR, the main concern for human imaging is the potential for the E_1 fields from the array elements to constructively superimpose locally, creating a local SAR hot spot. A simple estimate demonstrates how serious the "worst-case" superposition can be. If the E_1 fields from the eight elements superimpose and generate an 8 fold increase compared to a single element, then the local SAR at that location will increase 64 fold. Similarly, electric fields can destructively interfere. This means that if one channel stops transmitting due to equipment failure, the local SAR can actually increase. Therefore, in addition to monitoring the average power from each channel, a pTX system must make an estimate of local E_1 fields and how they superimpose so that the local SAR limits are not exceeded. As the pulse design becomes increasingly tailored to the individual patient, the local SAR check must also move in this direction. This will require fast local SAR calculation methods based on the field patterns calculated for the array and the specific pulse designed for that subject. Preliminary work has exploited the ability to penalize high-amplitude RF pulses in the pulse design optimization, but significant future development is needed to explicitly include local SAR regularization in the design of the RF pulses and enable a flexible trade-off between RF excitation properties (due to B_1) and local SAR distribution (due to E_1).

Remaining challenges

In addition to the SAR estimation and monitoring problem, several other outstanding challenges must be solved before accelerated 2D and 3D spatially tailored excitations can be routinely employed. The method relies on a fast but accurate mapping of the B_1 transmit field in the subject, which is an intense and ongoing area of innovation with several promising methods being proposed in the literature. A second area of innovation is the calculation of high flip-angle spatially tailored RF pulses. Most of the work performed to-date has assumed the small flip angle approximation. While this approximation provides for elegant and computationally tractable RF designs with familiar tradeoffs based on well known Fourier transform properties, large flip-angle pulses are central to many clinical pulse sequences and the low flip-angle constraint needs to be addressed for general applicability of pTX. This computational problem is now just starting to be addressed.

11

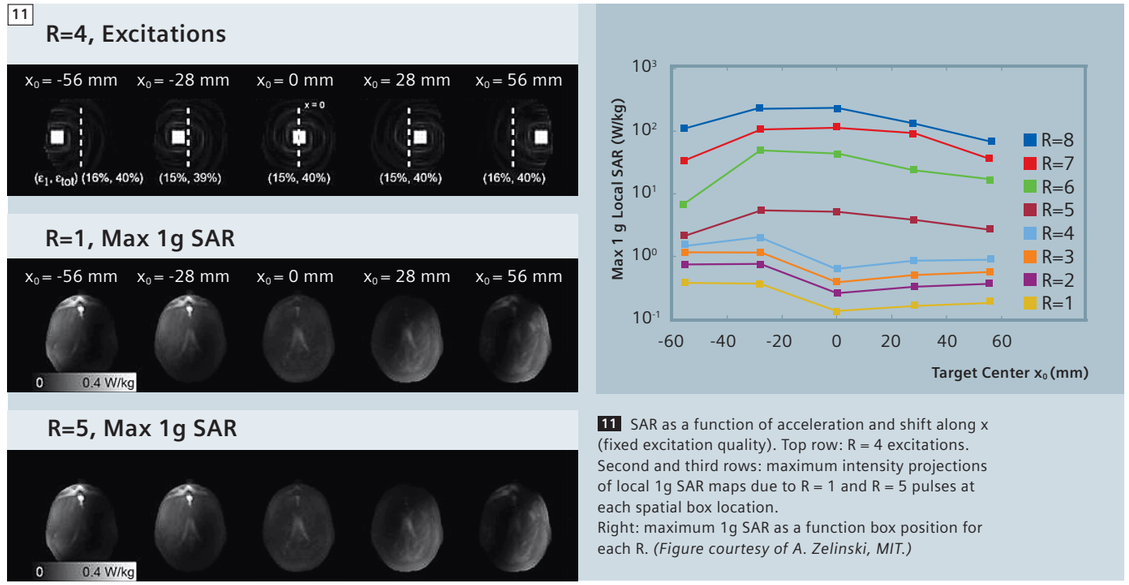

11 SAR as a function of acceleration and shift along x (fixed excitation quality). Top row: R = 4 excitations. Second and third rows: maximum intensity projections of local 1g SAR maps due to R = 1 and R = 5 pulses at each spatial box location.
Right: maximum 1g SAR as a function box position for each R. *(Figure courtesy of A. Zelinski, MIT.)*

Conclusions

Theoretical work on parallel RF transmission and recent experimental validations on 8-channel prototype systems at 3T and 7T indicate that parallel excitation has the potential to overcome critical obstacles to robust and routine human scanning at high field strength. As these developments are extended, high-field human imaging will be possible with essentially constant flip angle, and therefore no compromise in signal strength or clinical contrast, across the human head and body with RF pulse durations comparable to current slice selective pulses. While most work has been concentrated on head-sized transmitters at 7T, the methods are readily translatable to body transmit coils at 3T. Of course, intriguing research questions remain open in several areas, including optimal coil array designs that minimize element couplings and maximize spatial orthogonality of individual channels; the estimation of local SAR from a subject-specific spatially tailored RF pulse; and the development of rapid and robust RF pulse designs that extends the current low-flip angle domain to arbitrary excitation angle, such as spin echoes, saturation, and inversions pulses. However, with continued active research in these areas, progress is likely to accelerate, and logical extensions of the architecture of a current clinical scanner readily accommodates the requirements of a general parallel RF excitation system supported by fast, subject and application tailored RF pulse design software capable of extending MR excitation from the simple slice-select to the more generally tailored anatomy- or application-specific RF excitation pattern.

Acknowledgements

The authors would like to acknowledge the many researchers at Siemens, MGH and MIT whose work is summarized here. We especially acknowledge Kawin Setsompop, Vijay Alagappan, and Adam Zelinski whose thesis work was reviewed here. We also thank Ulrich Fontius and Andreas Potthast for their work setting up the 8-channel 3T and 7T systems and Franz Hebrank and Franz Schmitt for their leadership role in the collaboration and Josef Pfeuffer, Axel vom Endt and Hans-Peter Fautz for their on-going support.
We acknowledge grant support from the NIH (P41RR14075, R01EB007942, and R01EB006847) and a research agreement and research support from Siemens Healthcare. One of us (LLW) acknowledges consulting income from Siemens Healthcare.

WIP – Works in Progress. This information about this product is preliminary. The product is under development and not commercially available in the U.S., and its further availability cannot be ensured.

References

1 Butler, J. and R. Lowe, Beamforming matrix simplifies design of electronically scanned antennas. Electron Design, 1961. 9: p. 170–173.
2 Tropp, J., Mutual Inductance in the Bird-Cage Resonator. J Magn Reson, 1997. 126(1): p. 9–17.
3 Alagappan, V., et al. Mode Compression of Transmit and Receive Arrays for Parallel Imaging at 7T. in International Society for Magnetic Resonance in Medicine. 2008. Toronto, Canada.
4 Pauly, J., D. Nishimura, and A. Macovski, A k-space analysis of small-tip angle excitation. J Magn Reson, 1989. 81: p. 43–56.
5 Katscher, U., et al., Transmit SENSE. Magn Reson Med, 2003. 49(1): p. 144–50.
6 Zhu, Y., Parallel excitation with an array of transmit coils. Magn Reson Med, 2004. 51(4): p. 775–84.
7 Zelinski, A., et al., Comparison of three algorithms for solving linearized systems of parallel excitation RF waveform design equations: Experiments on an eight-channel system at 3 Tesla. Concepts in Magnetic Resonance Part B: Magnetic Resonance Engineering, 2007. 31B: p. 176–190.
8 Setsompop, K., et al., Magnitude least squares optimization for parallel radio frequency excitation design demonstrated at 7 Tesla with eight channels. Magn Reson Med, 2008. 59(4): p. 908–15.
9 Zelinski, A.C., et al., Sparsity-enforced slice-selective MRI RF excitation pulse design. IEEE Trans Med Imaging, 2008. 27(9): p. 1213–29.
10 Setsompop, K., et al., Slice-selective RF pulses for in vivo B1+ inhomogeneity mitigation at 7 tesla using parallel RF excitation with a 16-element coil. Magn Reson Med, 2008. 60(6): p. 1422–32.
11 Zelinski, A.C., et al., Specific absorption rate studies of the parallel transmission of inner-volume excitations at 7T. J Magn Reson Imaging, 2008. 28(4): p. 1005–18.
12 Shinnar, M. and J.S. Leigh, The application of spinors to pulse synthesis and analysis. Magn Reson Med, 1989. 12(1): p. 93–8.
13 Shinnar, M., et al., The synthesis of pulse sequences yielding arbitrary magnetization vectors. Magn Reson Med, 1989. 12(1): p. 74–80.
14 Shinnar, M., L. Bolinger, and J.S. Leigh, The use of finite impulse response filters in pulse design. Magn Reson Med, 1989. 12(1): p. 81–7.
15 Shinnar, M., L. Bolinger, and J.S. Leigh, The synthesis of soft pulses with a specified frequency response. Magn Reson Med, 1989. 12(1): p. 88–92.
16 Pauly, J., et al., Parameter relations for the Shinnar-Le Roux selective excitation pulse design algorithm. IEEE Tr Medical Imaging, 1991. 10(1): p. 53–65.
17 Mao, J.M., TH, K. Scott, and E. Andrew, Selective inversion radiofrequency pulses by optimal control. J Magn Reson, 1986. 70(2): p. 310–318.
18 Conolly, S., D. Nishimura, and A. Macovski, Optimal control solutions to the magnetic resonance selective excitation problem. IEEE T Med Imaging, 1986. MI-5(2): p. 106–115.
19 Geen, H., S. Wimperis, and R. Freeman, Band-selective pulses without phase distortion. A simulated annealing approach. J Magn Reson Med, 1989. 85(3): p. 620–627.

Contact
Lawrence L. Wald
Associate Professor of Radiology
Athinoula A. Martinos Center for Biomedical Imaging
Department of Radiology
Massachusetts General Hospital
Harvard Medical School and
Harvard-MIT Division of Health Sciences and Technology
wald@nmr.mgh.harvard.edu

Elfar Adalsteinsson
Associate Professor
Department of Electrical Engineering and Computer Science
Harvard-MIT Health Sciences and Technology
Massachusetts Institute of Technology
elfar@mit.edu

Global Siemens Headquarters

Siemens AG
Wittelsbacherplatz 2
80333 Muenchen
Germany

Global Siemens Healthcare Headquarters

Siemens AG
Healthcare Sector
Henkestrasse 127
91052 Erlangen
Germany
Phone: +49 9131 84-0
www.siemens.com/healthcare

www.siemens.com/healthcare-magazine

Order No. A91MR-1000-85C-7600 | Printed in Germany | CC MR SD 09110.2 | © 09.11, Siemens AG

Global Business Unit

Siemens AG
Medical Solutions
Magnetic Resonance
Henkestr. 127
DE-91052 Erlangen
Germany
Phone: +49 9131 84-0
www.siemens.com/healthcare

Local Contact Information

Asia
Siemens Pte Ltd
The Siemens Center
60 MacPherson Road
Singapore 348615
Phone: +65 6490-8096

Canada
Siemens Canada Limited
Medical Solutions
2185 Derry Road West
Mississauga ON L5N 7A6
Canada
Phone: +1 905 819-5800

Europe/Africa/Middle East
Siemens AG
Medical Solutions
Henkestr. 127
91052 Erlangen
Germany
Phone: +49 9131 84-0

Latin America
Siemens S.A.
Medical Solutions
Avenida de Pte. Julio A. Roca No 516,
Piso 7
C1067ABN Buenos Aires
Argentina
Phone: +54 11 4340-8400

USA
Siemens Medical Solutions U.S.A., Inc.
51 Valley Stream Parkway
Malvern, PA 19355-1406
USA
Phone: +1-888-826-9702